Master's thesis

NTNU
Norwegian University of Science and Technology
Faculty of Natural Sciences
Department of Biotechnology and Food Science

Ingrid Christine Røgenes

Characterization of alginate-based nanoparticles with atomic force microscopy, scanning electron microscopy, and light scattering

Master's thesis in Nanotechnology
Supervisor: Bjørn E. Christensen
June 2023

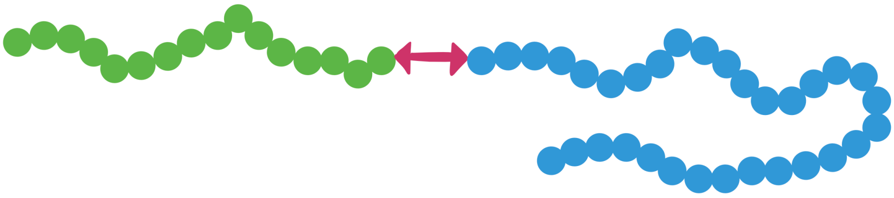

NTNU
Norwegian University of
Science and Technology

Ingrid Christine Røgenes

Characterization of alginate-based nanoparticles with atomic force microscopy, scanning electron microscopy, and light scattering

Master's thesis in Nanotechnology
Supervisor: Bjørn E. Christensen
June 2023

Norwegian University of Science and Technology
Faculty of Natural Sciences
Department of Biotechnology and Food Science

NTNU
Norwegian University of
Science and Technology

Acknowledgements

First and foremost, I would like to thank my supervisor, Professor Bjørn E. Christensen. Thank you for introducing me to this exciting project and for guiding me through the work on it. I very much appreciate that I could swing by your office any time to discuss results and plans.

A big thank you to Staff Engineer Elise Holmås, who has helped me through the processes and analysis in the biopolymer lab. Your broad knowledge and talent of communicating it to others has been irreplacable to me during the work on this thesis.

I wish to thank Senior Engineer Olav A. Aarstad for invaluable assistance with the MALS-experiments. Your expertise on the area has been vital in performing the experiments and analyzing the data.

I'm grateful for my fellow master students Ingrid Ljøsne Tollefsen and Julie Elvsaas. Being in a team and not on your own is very valuable, and working with you has been delightful. The weekly meetings with the BEC group have been very helpful, as we could all discuss our recent results and plans moving forward.

Finally, I would like to thank my dad. Your continuous support for, and interest in, my projects and ventures means a lot to me. For all my life you have prioritized my well being and encouraged me in my education. You always emphasize that one is never done with learning, and I will bring that sentiment with me on my journey now after university. To quote the legendary Marie Curie:

Nothing in life is to be feared, it is only to be understood.

Preface

This Master's Thesis was conducted at the Norwegian University of Science and Technology (NTNU) between January and June 2023.

The work was carried out at NTNU NanoLab and at the Norwegian Biopolymer Laboratory (NOBIPOL), Department of Biotechnology and Food Science, under the supervision of Professor Bjørn E. Christensen.

This work was financed by the Institute of Biotechnology and Food Science (NTNU), NTNU Technology Transfer, and the Norwegian Research Council.

Abstract

This thesis aims to establish a characterization protocol for G_m-b-Dex_n nanoparticles (NPs). There is limited data available for this type of biopolymer-based NP, and a comprehensive characterization protocol had not yet been established. These NPs assembled from oligoguluronate and dextran diblock copolymers are being investigated with the long-term goal of creating a radiopharmaceutical drug that can be used in localized radiation treatment for cancer patients.

G_m-b-Dex_n NPs were self-assembled from diblock copolymers by dialysis or direct titration with solutions containing Ca^{2+} and/or Ba^{2+} cations. Characterization of the NPs was done using dynamic light scattering (DLS), multi-angle light scattering (MALS), atomic force microscopy (AFM), and scanning electron microscopy (SEM).

A characterization protocol consisting of DLS, AFM, and MALS was found to be suitable for the G_m-b-Dex_n NPs. A first impression of the NPs' size distribution is obtained swiftly with DLS. AFM is subsequently used to closely investigate the size and shape of individual NPs. Finally, MALS is used to determine the molar mass of the NPs. The protocol used for characterization with SEM in this work proved not to be ideal, and did not provide much useful information about the NPs. This could be a focus point for future research.

The establishment of an optimal characterization protocol for a specific type of particle is crucial for the overall research development. Having a clearly outlined path for the characterization frees up researches' time to investigate other aspects of the scope. In addition, the commercialization of a pharmaceutical drug is concerned with both the quality control aspect of proper characterization, and the business perspective of cost versus benefits. Determining a characterization protocol for the G_m-b-Dex_n NPs hence serves both the research aspect and the eventual commercialization of the radiopharmaceutical drug.

Key concepts: biopolymer-based nanoparticle, oligoguluronate, dextran,
characterization protocol, radiopharmaceutical

Sammendrag

Denne avhandlingen har som mål å etablere en karakteriseringsprotokoll for G_m-b-Dex_n nanopartikler (NP). Det finnes kun begrensede data for denne typen biopolymer-baserte NPer, og en grundig karakteriseringsprotokoll hadde enda ikke blitt etablert. Disse NPene satt sammen av oligoguluronat og dextran diblokk kopolymerer blir undersøkt med det endelige målet å utvikle et radiofarmasøytisk legemiddel som kan brukes til lokal strålebehandling for kreftpasienter.

G_m-b-Dex_n NPer ble fremstilt via self-assembly av diblokk kopolymerer ved dialyse eller direkte titrering med løsninger som inneholder Ca^{2+} og/eller Ba^{2+} kationer. Karakterisering av NPene ble gjort med dynamisk lysspredning (DLS), fler-vinkel lysspredning (MALS), atomær kraftmikroskopi (AFM) og scannende elektronmikroskopi (SEM).

En karakteriseringsprotokoll bestående av DLS, AFM og MALS ble funnet til å være passende for G_m-b-Dex_n NPer. Et førsteinntrykk av NPenes størrelsesfordeling er fort ervervet med DLS. AFM benyttes så til å undersøke størrelsen og formen på individuelle NPer nøye. Til slutt brukes MALS til å bestemme den molare massen til NPene. Karakteriseringsprotokollen som ble brukt for SEM i dette arbeidet viste seg å ikke være ideell, og ga ikke særlig mye nyttig informasjon om NPene. Dette kan være et fokuspunkt for fremtidig forskning.

Etableringen av en optimal karakteriseringsprotokoll for en spesifikk type partikkel er avgjørende for den helhetlige forskningsutviklingen. Det å ha en klart definert fremgangsmåte for karakteriseringen frigir forskeres tid til å utforske andre aspekter av forskningen. I tillegg er kommersialiseringen av et farmasøytisk legemiddel påvirket av både kvalitetskontrollaspektet av passende karakterisering, og av forretningsperspektivet av kostnad versus nytte. Å bestemme en karakteriseringsprotokoll for G_m-b-Dex_n NPer gagner derfor både forskningsaspektet og den påfølgende kommersialiseringen av det radiofarmasøytiske legemiddelet.

Nøkkelkonsepter: biopolymer-basert nanopartikkel, oligoguluronat, dextran, karakteriseringsprotokoll, radiofarmasøytisk

Acronyms

A_2	Second virial coefficient
AFM	Atomic force microscopy
BSE	Backscattered electrons
DCR	Derived count rate
Dex, D_n	Dextran
DLS	Dynamic light scattering
DP_n	Number average degree of polymerization
EDTA	Ethylenediaminetetraacetic acid
G-block, G_m	Oligoguluronate
MALS	Multi-angle light scattering
MQ	Milli-Q water
M_w	Weight average molecular weight
NMR	Nuclear magnetic resonance spectroscopy
NP	Nanoparticle
PB	2-Methylpyridine borane complex/2-Picoline borane complex
PDHA	O,O′-1,3-Propanediylbishydroxylamine dihydrochloride
SE	Secondary electrons
SEC	Size-exclusion chromatography
SEM	Scanning electron microscopy

Table of Contents

List of Figures

List of Tables

1 Introduction

Biopolymers are produced by or derived from animate organisms from building blocks including saccharides and amino acids [1, 2, 3]. Due to their high degree of biodegradability, biopolymers have gained much traction as a more environmentally sustainable alternative to plastic polymers. In addition, the biocompatibility of biopolymers makes them an interesting research topic in the medical- and pharmaceutical industries. Application areas within medicine and pharmaceuticals include drug delivery, tissue engineering, wound recovery, and medical implants. For drug delivery technology, biopolymer-based nanoparticles (NPs) have been highlighted as especially interesting [4, 5]. The biopolymer-based NPs investigated in this work consists of alginate oligoguluronate (G-block, G_m), a linker (-b-), and dextran (Dex_n), referred to as the G_m-b-Dex_n NPs.

In the past, biomaterials were designed to be inert and not interact with the host body [6]. Due to extensive research done on the biocompatibility of different biomaterials, the materials being chemically inactive is no longer a prerequisite. For example, alginate hydrogels mimic the extracellular matrix of living tissue and can be implemented in drug delivery, wound healing, and cell transplantation. Alginate can chelate with divalent cations, e.g., Ca^{2+}, to form such hydrogels [7]. Since alginate is an anionic polysaccharide, drug delivery of cationic molecules and drugs through electrostatic interactions is particularly relevant.

An essential part of developing a new type of NP is establishing a characterization protocol. To acquire all relevant information about a particle, different characterization techniques must be employed together. The aim of this work is to determine which characterization techniques are best suited to obtain a comprehensive understanding of G_m-b-Dex_n NPs.

The long-term goal with the G_m-b-Dex_n NPs is to create a pharmaceutical drug for localized radiation therapy in cancer treatment, i.e., a radiopharmaceutical drug [8]. The idea behind this is to perform an ion exchange where the divalent cations (Ca^{2+}, Ba^{2+} etc.) bound in the oligoguluronate core of the NPs are exchanged with radioactive, cationic, divalent isotopes, e.g., $^{64}\mathrm{Cu}^{2+}$. Further, attaching suitable ligands to the dextran corona of the NPs would assist them in locating cancerous cells in the body. Through using NPs as carriers of radiation, the radiation treatment would become more localized and spare healthy tissue which would otherwise be affected by general radiation treatment.

Along with other treatment such as surgery and chemotherapy, approximately half of all cancer patients receive a form of radiation therapy [9]. However, the radiation therapy offered to most cancer patients today, i.e., radiation administered outside the body, has remained more or less the same for the past century. A plethora of side effects can affect the patient after receiving externally administered radiation treatment. Official government healthcare resources including the National Cancer Institute [10], the NHS [11], and Cancer Australia [12] report side effects such as skin problems, fatigue, hair loss, and nausea.

This work focuses on four characterization techniques. Atomic force microscopy (AFM) and dynamic light scattering (DLS) have been used in previous work on G_m-b-Dex_n NPs [13, 14], and are explored further in this work. Scanning electron microscopy (SEM) and multi-angle light scattering (MALS) are new approaches to the characterization of G_m-b-Dex_n NPs. AFM is used to examine the topography of a sample, in this case the size and shape of NPs. SEM similarly explores the NPs' topography, but also the chemical composition. DLS surveys the size distribution, while MALS assesses the molar mass of NPs. Together, these characterization techniques can be employed to obtain a comprehensive image of the G_m-b-Dex_n NPs in question.

This work begins with a thorough Theory Section 2 aiming to equip the reader with both general knowledge and topic-specific terms later referred to. The theory focuses on the components and assembly of G_m-b-Dex_n NPs, as well as an in-depth description of various characterization techniques. The Experimental Section 3 describes the full preparation procedure of the NPs, along with the operation and data analysis of the characterization techniques. The Results Section 4 presents the data acquired through the characterization of the NPs. The Discussion Section 5 tackles the presented results with focus on obtained information and the significance of the different characterization techniques. Finally, the Conclusion Section 6 epitomizes the work into its essence.

2 Theory

Parts of the theory section has been taken and/or is adapted from the author's Project Thesis [13], which was conducted in 2022. Since this Master's Thesis is a continuation of the work done in the Project Thesis, much of the theory and some of the experimental procedures overlap. Sections 2.1, 2.2, 2.3, 2.4, 2.5, 2.6, and 2.7 are acquired from the Project Thesis, with the addition of some new information and figures. Sections 2.8, 2.9, 2.10, and 2.11 are completely new for this work.

2.1 Alginate

Alginates occur naturally in brown algae and are produced by some bacteria species [6, 15, 16]. The monomers in alginate are (1 → 4)-linked α-L-guluronic acid (G) and (1 → 4)-linked β-D-mannuronic acid (M). The chemical structure of these monomers can be seen in Figures 1 and 2. These monomers form G-blocks, M-blocks, and MG-blocks in different proportions, depending on the source of the alginate. Figure 3 shows the chemical structure of an alginate containing both an M-block and a G-block. Industrial sodium alginate has a molecular weight between 32.000 and 400.000 Da.

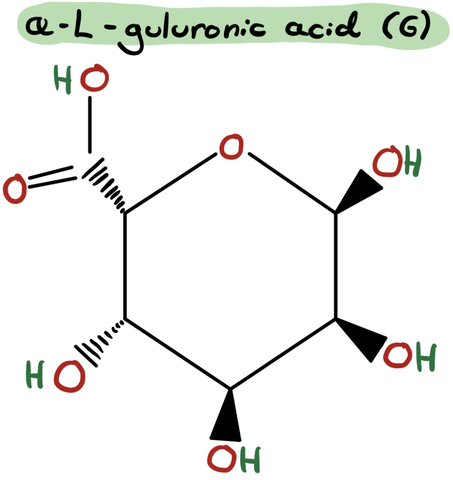

Figure 1: The chemical structure of α-L-guluronic acid (G). Figure based on [17].

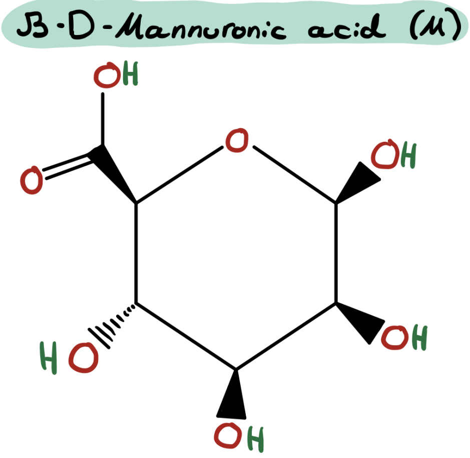

Figure 2: The chemical structure of β-D-mannuronic acid (M). Figure based on [18].

Industrially, alginate is either extracted from brown algae, or synthesized by bacteria [6]. An aqueous alkali solution, e.g., NaOH, is used to extract the alginate from algae, followed by filtration of the alginate. Alginate is precipitated upon addition of NaCl or $CaCl_2$. Alginic acid is then obtained by treating the alginate salt with a dilute HCl solution. Alginate synthesized by bacteria is favorable if specific structures or properties of the alginate is necessary. The bacterial biosynthesis involves a precursor substrate being modified and transferred through different bacterial membranes, and finally export through the outermost membrane of the bacterial cell.

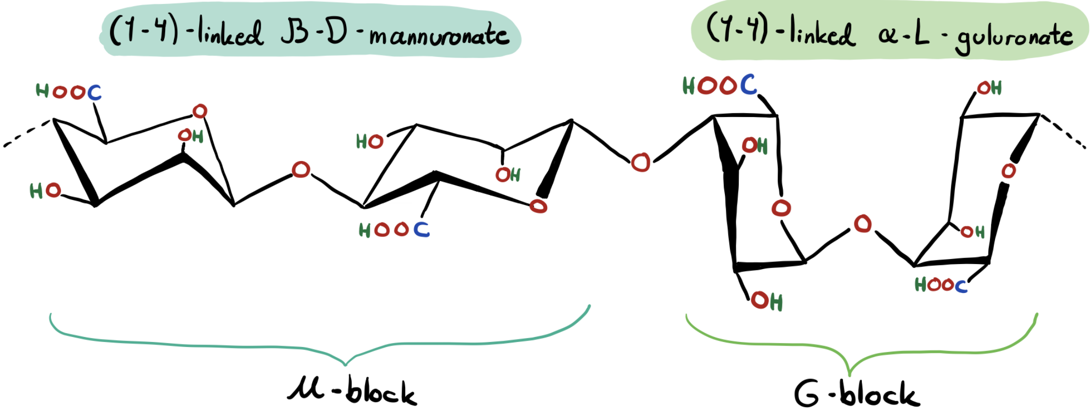

Figure 3: The chemical structure of alginate. Figure based on [19].

Studies have shown that high-purity alginate is particularly biocompatible [6, 20]. The purification of alginate is crucial for its use in biomedical applications [21]. Alginate in nature can contain contaminants such as proteins, DNA and RNA, polyphenolic compounds, and endotoxins, which can induce an unwanted immunological response in the body. Due to mammals lacking the polymer-cleaving enzyme alginase, alginate can in principle not degrade in them. However, an alginate hydrogel with a moderate molecular weight can dissolve into the surrounding media *in vivo*. This happens through ion exchange reactions with monovalent cations, e.g., Na^+. To sum up, alginate in a purified, gelated form is particularly attractive for biomedical purposes.

2.1.1 Alginate G-blocks

Oligoguluronate (G-block) can form hydrogels together with divalent cations, e.g., Ca^{2+}, Sr^{2+}, and Ba^{2+} through intermolecular cross-linking [6, 7, 16]. The cations bind to G-blocks, and junctions are formed between G-blocks in adjoining polymer chains. A hydrogel is formed as a result of this cross-linking. The "egg-box" model describes the hydrogel formation [22], see Figure 4 for a visualization. The model explains how G-blocks are linked together by divalent cations, in particular Ca^{2+}, to form multimers by lateral association. The amount of G-block in an alginate directly impacts its gelating abilities, as the M-blocks do not participate in gelation [6]. The G/M-block ratio of the composition, the molecular weight, and the G-block length are key factors that affect the gelation abilities for native alginate. However, it is central to note that pure G-block can form solid precipitates or especially stiff hydrogels in the presence of divalent cations [16]. Many factors can counteract this effect, for instance the linkage with a different biopolymer.

In this study, the gelating ability of alginate G-block is examined within the context of self-assembly of NPs. For this application, it is important to connect the G-block to a neutral polysaccharide, e.g., dextran [16]. This is done to counteract the profound attractive interactions between G-blocks and divalent cations using a neutral block for repulsive interactions. Read more about such block copolymers in Section 2.3.

Hydrogels are used for numerous applications in biomedicine because of their biocompatibility [6]. They are similar in structure to macromolecules in the body, and do not require an invasive procedure to be administered. Applications include tissue engineering, wound healing, and drug delivery.

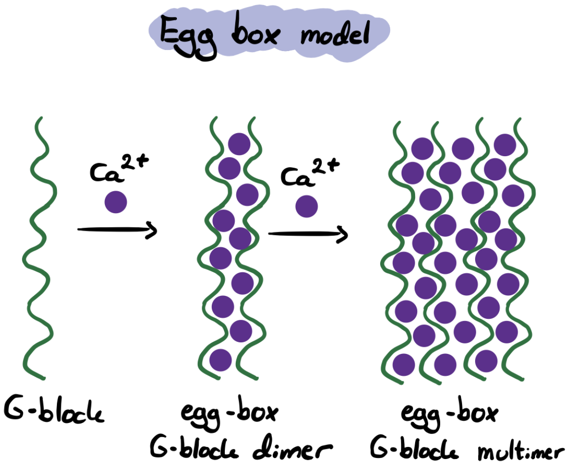

Figure 4: Visualization of the egg-box model for G-block hydrogel formation. Figure based on [23].

2.2 Dextran

Dextran is a neutral, branched biopolymer consisting of anhydroglucose units linked by approximately 95% α-(1→6) glycosidic bonds [24, 25]. The chemical structure of dextran can be seen in Figure 5. Industrially, dextran is produced by fermentation of sucrose by the bacteria species *Leuconostoc mesenteroides* [25, 26]. Depending on the bacterial strand from which the dextran was produced, and the fermentation conditions, there are variations in the amount and types of linkages in its branches. The most widely used variant, produced by *Leuconostoc mesenteroides*, has 5% branching with α-(1→3) branch linkages [26, 27]. Nevertheless, dextran can also have branch linkages of the α-(1→2) and α-(1→4) types [27]. There have been different conclusions as to the average branch length, but the consensus lies between one and three glucose units for the average branch [28, 29]. Native dextran has a rather high molecular weight, typically within the range of 10^6 and 10^8 Da [30, 31, 32].

Another characteristic of polymers is the persistence length. It describes the length where a polymer maintains its rigidity [33], i.e., a flexible polymer is recognized by a short persistence length, and a rigid polymer by a long persistence length. The property is intrinsic to the polymer and is not affected by chain length. Dextran is known as a flexible polymer with a persistence length of around 0.4 nm [33, 34]. The flexibility of dextran accounts for its random coil behavior in aqueous solutions.

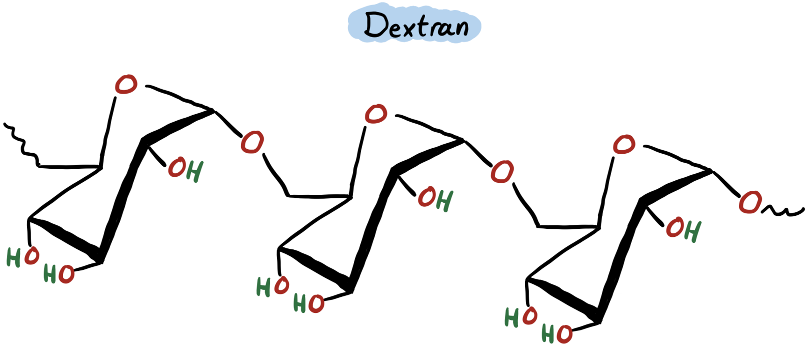

Figure 5: The chemical structure of dextran. Figure based on [35].

Dextran has been exploited for clinical applications throughout the past five decades [35]. It is used as a plasma volume expander, cardiovascular flow enhancer, and antithrombotic agent. Due to its large number of hydroxyl groups, dextran is easy to modify using various chemical modification methods, e.g., by oxidation or enzymes. Dextran is water soluble and stable under physiological conditions. It takes longer for human enzymes to degrade dextran than other similar biopolymers, e.g., glycogen, and therefore it is suitable for use in drug delivery systems. Dextran contributes to a longer circulation time for therapeutic agents, and can be used to reduce immunogenicity of proteins and enzymes.

2.3 Block copolymers

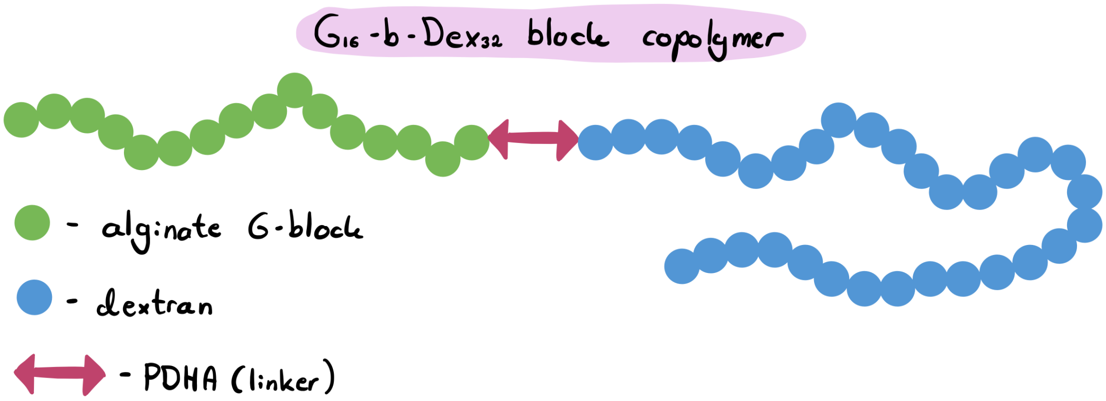

Figure 6: An example of a block copolymer, G_{16}-b-Dex_{32}, which has been extensively researched in this thesis.

When two or more blocks of oligo- or polysaccharides are connected with a linker substance, they are referred to as block copolymers or block polysaccharides [16, 36]. A diblock consists of two blocks and a linker, see Figure 6 for an example. Block copolymers provide opportunities for enhanced material attributes that the polymers do not have on their own.

Reductive amination is an organic synthesis method often used to synthesize block copolymers [36]. It is a two-step process where first, a primary amine and an aldehyde form an imine intermediate/Schiff's base through a condensation reaction. Second, a secondary amine is obtained by reduction of the imine. It is the aldehyde at the reducing end of the polysaccharide that is susceptible to reductive amination [37].

2.3.1 Self-assembly of NPs

Depending on the components chosen for the diblock, they can display self-assembly abilities. As demonstrated in [14], diblocks of G-block and dextran self-assemble to NPs with a micellar structure in the presence of divalent cations. The G-blocks complexed with divalent cations make up the nucleus, and dextran makes up a stabilizing corona. Figure 7 shows a visualization of the G_m-b-Dex_n NP.

NPs self-assemble when a solution of G_m-b-Dex_n diblocks is dialysed against, in this case, the calcium salt $CaCl_2$. However, other salts of divalent cations can also be used. It has been reported that self-assembly with Sr^{2+} and Ba^{2+} gives similar NPs as Ca^{2+}, but with a somewhat smaller size [14]. The less studied method of inducing self-assembly by direct titration of divalent cations will also be explored in this thesis.

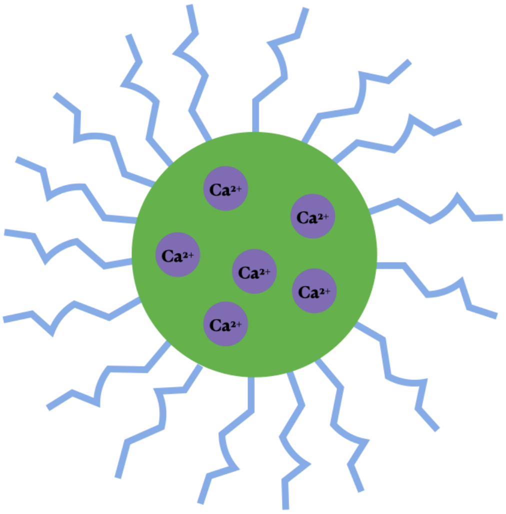

Figure 7: Visualization of the G_m-b-Dex_n self-assembled NP.

2.4 Chemicals used in diblock preparation

2.4.1 PDHA

O,O′-1,3-Propanediylbishydroxylamine dihydrochloride (PDHA) is a dioxyamine with the molecular formula $C_3H_{10}N_2O_2{\cdot}2HCl$, and a molecular weight of 179.05 Da [38]. It has been shown that dioxyamines are suitable for block polysaccharide preparation [16]. Figure 8 shows the chemical structure of PDHA.

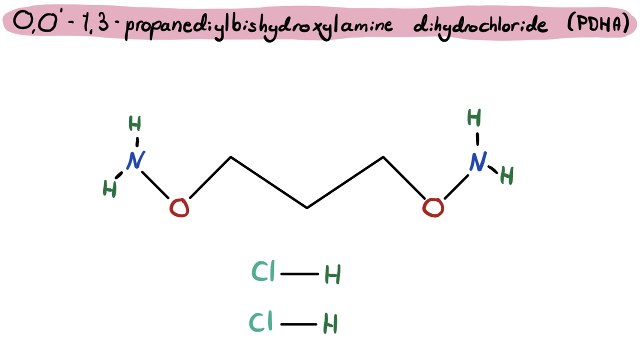

Figure 8: The chemical structure of PDHA. Figure based on [39].

2.4.2 Picoline borane

2-Methylpyridine borane complex/2-Picoline borane complex (PB) is a reducing agent with the molecular formula $C_6H_{10}BN$, and a molecular weight of 106.96 Da [40]. It has been introduced as a less toxic and more environmentally friendly alternative to sodium cyanoborohydride ($NaCNBH_3$) [41]. One of its application areas is reductive amination of oligosaccharides. Figure 9 shows the chemical structure of PB.

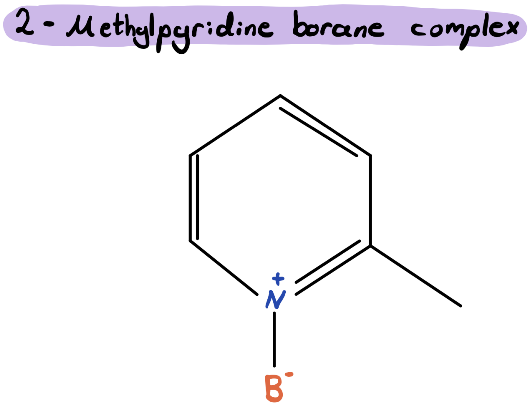

Figure 9: The chemical structure of Picoline borane. Figure based on [42].

2.5 Size-exclusion chromatography

Size-exclusion chromatography (SEC) is based on the principle that different size molecules will be eluted from a porous matrix at different rates [43]. In this context, the particle size refers to the hydrodynamic volume of particles [44]. The porous matrix has a fractionation range that is dependent on the pore size [45]. The largest molecules will be eluted first because they are excluded from the pores. As molecules get smaller, they will remain in the pores for a given time before they are eluted according to decreasing size. This makes it possible to separate and collect fractions with a specific molecular weight. The analytical result is a SEC-chromatogram showing the sample compound as a broad peak [46]. SEC is a relative technique that estimates the molecular weight of an analyte based on the elution volume [47]. SEC can be combined with an absolute detection technique such as multi-angle light scattering (MALS), collectively known as SEC-MALS, to calculate the precise molecular weight of the analyte. MALS is considered an absolute detection technique because it uses fundamental physical equations to calculate the molecular weight.

The experimental setup for SEC consists of a variety of components. The columns, typically several in series, contain the porous matrix where the solution passes through [46]. The solution consists of the sample and a mobile phase, the latter being a buffer solution [48]. A high-performance liquid chromatography (HPLC) pump is used to drive the solution through the columns with a specific flow rate [49]. A refractive index (RI) detector is used to measure the concentration of molecules as they are eluted form the columns [50]. A fraction collector is used to collect the separated fractions [48]. Finally, a data acquisition system is used to collect and analyze the data from the RI-detector and create a SEC-chromatogram [51].

2.6 Nuclear magnetic resonance spectroscopy

Nuclear magnetic resonance (NMR) spectroscopy is based on the unique resonance frequencies emitted by molecules when exposed to a magnetic field [52]. A molecule's chemical environment is made up of the various chemical groups and bonding conditions in it, and produces a resonance frequency known as the chemical shift. The chemical shift is used to find the nuclei types present in a sample. Further, the peak intensity is used to determine the quantity of present nuclei types.

The impact of an external magnetic field makes electrically charged nuclei move to a higher energy state [53]. The energy difference between these states is represented by ΔE:

$$\Delta E = hf = E_2 - E_1 \tag{1}$$

where h is Planck's constant, f is frequency, E_1 is the lower energy state, and E_2 is the higher energy state. The nuclei then releases this energy when the magnetic field is switched off. These energy releases are nuclei-specific and are documented by a computer which subsequently produces the NMR spectra.

NMR spectrometers contain a superconducting magnet coiled up in a cryogenic storage dewar containing liquid helium (4 Kelvin) [54]. Liquid nitrogen (77 Kelvin) is contained within an outer dewar to avoid vaporization of the liquid helium dewar. The magnetic field is homogenized by shim coils, which are central for the resolution of NMR [55]. Shim coils are an addition to the main magnet, which on its own cannot provide the magnitude of homogenity required for an NMR magnetic field. A spinner assembly is utilized to spin the sample tube and move it in and out of the probe carried by a gas cushion.

2.7 Atomic force microscopy

Atomic force microscopy (AFM) is a microscopy technique employing a sharp probe to scan the surface of a sample to obtain a high-resolution image of its topography [56]. The probe is mounted on a flexible cantilever and moved over the sample using a piezoelectric actuator. Piezoelectric materials have the ability to translate an electrical voltage into a mechanical movement [57]. Forces between the sample and probe are picked up by the probe as the deflection of the cantilever. A higher force exerted on the probe corresponds to a larger cantilever deflection [58]. A laser beam is focused onto the cantilever, and conveys the deflection signal on to a position sensitive photo diode [59, 60]. The change in intensity of the reflected light picked up by the photo diode can then be used to determine the position of the cantilever. These mechanisms are used to generate a map of the sample surface, which can be used to visualize the sample's topography, surface roughness, and other physical properties. A wide range of AFM imaging modes have been developed over the past 3 decades [58]. Figure 10 shows the working principle of AFM.

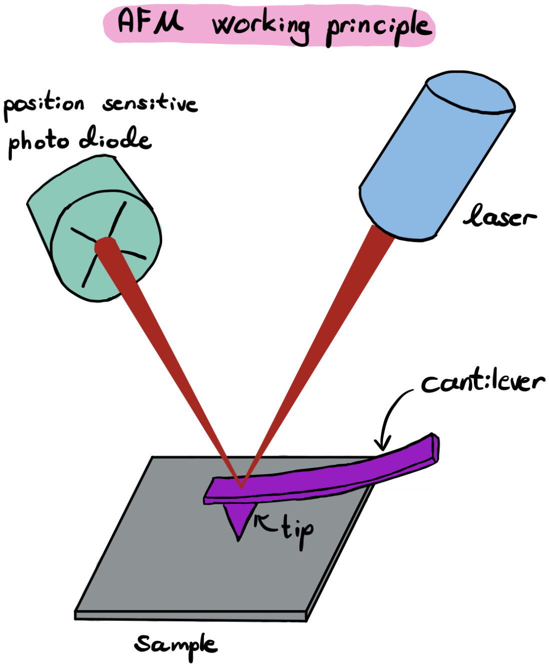

Figure 10: Sketch showing the working principle of AFM. Figure based on [61].

2.7.1 AFM modes

Contact mode involves continual physical contact between the probe tip and the sample surface [59, 62]. Repulsive forces arise between the probe and the sample because of atomic interactions between them, and in turn causes the cantilever to deflect. Samples analyzed by this mode must be able to withstand the lateral forces exerted on the probe tip. Although contact mode is commonly used on solid surfaces, it can be used on soft biological surfaces when the force applied is modified to a non-destructive level for the given sample [58].

Non-contact mode is solely based on measuring the atomic attractive forces between the sample and probe [60]. This mode is typically carried out under ultra-high vacuum or at low temperatures [63]. The reason for this is to take advantage of the high Q-factor (quality factor Q) sensitivity in non-contact AFM. The Q-factor and oscillation frequency are defining properties of oscillating systems [64]. A high Q-factor corresponds to a narrowly defined resonance, and the system stores more energy and loses less energy with each oscillation.

Tapping mode/dynamic mode is a compromise between contact mode and non-contact mode. Tapping mode circumvents the contact mode problem with high lateral forces between the sample and cantilever [65]. Moreover, since the tip touches the sample for a short moment, high lateral resolution is preserved. Tapping mode is based on the principle that the probe will make periodic contact with the sample if it is compelled to oscillate near its resonance frequency [60].

2.7.2 Bruker PeakForce Tapping and ScanAsyst

Scientific instrument manufacturer Bruker has developed new AFM technologies that have been used in this study. The following three paragraphs are adapted from the Application Note [65] for the technologies.

PeakForce Tapping combines the benefits of contact- and tapping mode AFM imaging by utilizing direct force control while avoiding damage to the sample by lateral forces. Similar to tapping mode, the probe only periodically contacts the sample, thus steering clear of lateral forces. Unlike tapping mode, PeakForce Tapping is a non-resonant mode performed at frequencies far below the resonance frequency of the cantilever. The benefits of the latter is avoiding the filtering effect and dynamics found in a resonance system. The z-position in PeakForce Tapping is modulated by a sine wave, as opposed to a triangular wave used in conventional force curves. This ensures unwanted resonances at the turnaround points are avoided, and instead applies a triggering at the peak force.

ScanAsyst uses the PeakForce Tapping technology to automatically adjust all critical analysis parameters. Feedback oscillation is discerned and removed immediately by an image correlation algorithm. The gain is adjusted in real-time by a feedback loop to obtain the predefined data quality and noise level. This technology can give much better resolution and image quality than using one gain setting (manual gain adjustment) for an entire image. According to sample conditions at various locations, the gain applied is optimized by ScanAsyst. Other features of ScanAsyst include optimization of set-point, control of scan rate, and z-limit adjustment.

The consequence of the PeakForce Tapping and ScanAsyst technologies is that AFM users are able to acquire high-quality images without extensive training and long experience in the field. Without this technology, users have to manually input the different imaging parameters, which can lead to low-quality images because of user inexperience or human error. The technologies are advances to conventional tapping mode, which has the major flaw of lacking automation of the feedback loop.

2.8 Scanning electron microscopy

In scanning electron microscopy (SEM), a beam of electrons is used instead of the optical waves utilized in optical microscopy [66]. Beams of particles, e.g., electrons, can be diffracted just as beams of light can. This is useful because the wavelength of light (around 0.5 μm) physically restricts the resolution which is possible to obtain with an optical microscope. Although optical microscopy, in particular optical fluorescense microscopy, is an important characterization technique in modern biology and biomedicine, the challenge remains the optical resolution limitations [67], a consequence of the fundamental laws of diffraction reported by Ernst Abbe in 1873 [68]. The wavelength of light as well as the numerical aperture of the objective pose rudimentary limitations to optical microscopy.

The resolution that can be obtained using an electron beam depends on the de Broglie wavelength of the electrons. The de Broglie wavelength λ for a particle is given by:

$$\lambda = \frac{h}{|p|} \tag{2}$$

where h is Plank's constant. The momentum $|p|$ is the product of the particle's mass m and its velocity v:

$$|p| = mv \tag{3}$$

The velocity v of a charged particle in an electric field being exposed to an acceleration voltage from rest can be calculated as follows:

$$v = \sqrt{\frac{2eV}{m}} \tag{4}$$

where e is the elementary charge, V is the acceleration voltage, and m is the mass of the particle. From these equations, it can be deducted that the higher the acceleration voltage an electron is exposed to, the higher its momentum, and thus the lower its de Broglie wavelength. When electrons are accelerated in the SEM's electron gun, they acquire a low de Broglie wavelength, and that is the basis for the high resolution that can be obtained using SEM. For example, the Thermo Fisher Scientific Apreo 2 SEM used in this work can achieve a resolution of up to 0.9 nm at 1 kV [69].

There are a number of different signals that are emitted when accelerated electrons hit a sample [70]. In the fields of biology and biomedicine, secondary electrons (SE) and backscattered electrons (BSE) are the most relevant. SE are emitted in close proximity to the surface of the sample and provide topographical information, including size and size distribution of particles [71]. BSE are released from the interior of the sample, and produce depth images as well as yielding information about the sample's composition. Because heavier elements emit more BSE, these appear brighter in SEM-images. Conversely, lighter elements appear darker. Biological specimens are commonly stained or fixated with heavy metals such as osmium, uranium, or lead to achieve better contrast in images. Typically, the specimen parts of interest are treated with a heavy metal to appear brighter than the surrounding tissue.

A key concept that influences the attainable resolution is the interaction volume [72]. The interaction volume is essentially the volume of the sample where the accelerated electrons can interact. This is mainly dependent on material and the acceleration voltage. A higher acceleration voltage leads to a larger interaction volume and inferior resolution, while a lower acceleration voltage provides a smaller interaction volume and superior resolution. This is why SE provide better resolution the BSE, because the interaction volume where SE operate is much smaller than for BSE. A visualization of the interaction volume can be seen in Figure 11.

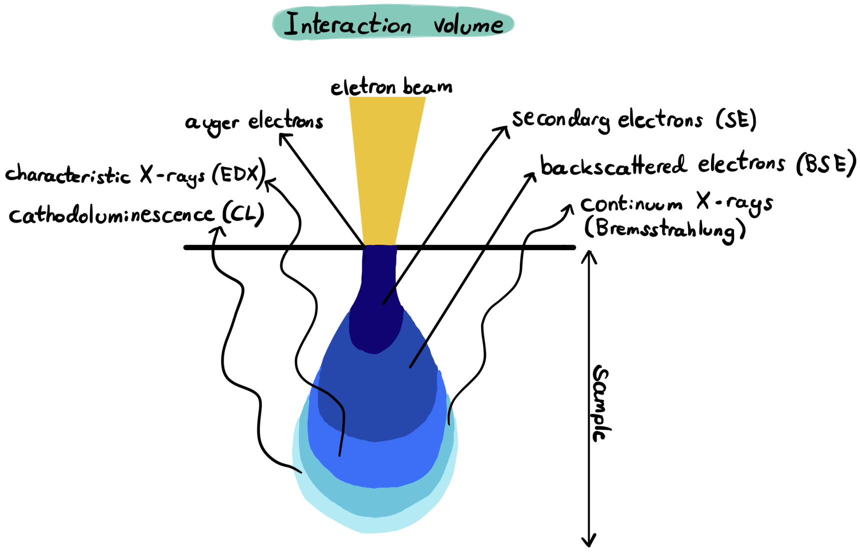

Figure 11: Visualization of the interaction volume. Figure based on [73].

Another central principle of SEM is the need for conductive samples [74]. Due to the applied voltage and high vacuum required to operate the instrument, charging effects can occur on non-conductive samples. Should the accelerated electrons encounter gas molecules due to insufficient vacuum, the image quality is negatively influenced due to the shortened mean free path of the electrons. However, the high vacuum may account for charging effects in non-conductive samples owing to uneven electron concentration at the sample. Accumulation of electrons in certain areas of the sample can be identified in images as having uneven brightness, bright lines, distortion, and loss of stereoscopic perception. There are a number of sample preparation techniques to prepare a non-conductive sample for SEM, the most common being applying a thin metallic- or carbon coating. The coating ensures that the charge remains equal across the sample surface, and prohibits excess electrons from accumulating.

2.9 Dynamic light scattering

Dynamic light scattering (DLS) is a light scattering technique used to obtain the size of nanoparticles in dispersion by analyzing their Brownian motion [75, 76, 77]. DLS is also known as quasi-elastic light scattering (QELS) or photon correlation spectroscopy (PCS) [75, 77]. The technique is non-invasive for the sample, quick, and easy to operate. In addition, only a small amount of sample is required [77]. It is the time dependence of the intensity that is measured with DLS [78]. This is possible because colloidal particles perform random walk governed by Brownian motion.

The hydrodynamic radius of the particles can be determined from their diffusion coefficient $D\tau$, because $D\tau$ depends on the size and shape of the particles [77]. $D\tau$ can be obtained through analysis of the intensity fluctuations of scattered light. These fluctuations occur because of the Brownian motion of the dispersed particles. When the particles are influenced by the cannonade of solvent molecules, they start exerting Brownian motion. The working principle of DLS is thus to relate Brownian motion to $D\tau$, which can then be used to calculate the hydrodynamic radius, i.e., the size, of particles.

In a DLS experiment, the sample is placed in a cuvette and exposed to a polarized laser beam [76]. A detector collects the scattering signals produced. Figure 12 shows the experimental setup.

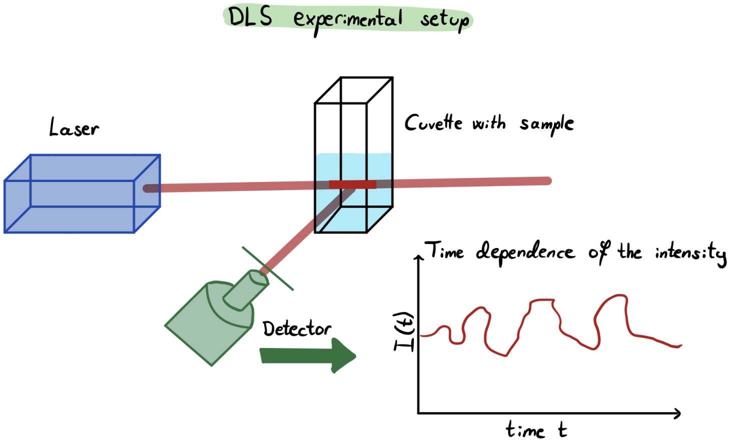

Figure 12: DLS experimental setup. Figure based on [78].

DLS has certain advantages over other techniques for size characterization [75]. A DLS scan analyzes a much larger number of NPs than a scan done by AFM or electron microscopy [75, 78]. This allows for a good statistical average particle size to be calculated. In addition, DLS is an *in situ* colloid characterization technique that allows the colloid sample to be analyzed in its native form. For AFM and electron microscopy, the sample must be dried or prepared by intricate sample preparation methods such as cryofixation. Furthermore, separation techniques such as SEC are far more time-consuming than DLS.

Drawbacks of DLS include high sensitivity to solvent viscosity and temperature, meaning that these must be known and kept constant, respectively, for a DLS experiment to be reliable [77]. Another drawback is low resolution. While DLS is a quick and relatively easy way of roughly determining the size of particles, it cannot differentiate between closely associated molecules such as monomers and dimers. Besides, DLS analysis is limited to transparent samples.

An important aspect of DLS is correlation, which is the analysis of scattered light intensity fluctuations over time [79]. The autocorrelation function is central to correlation analysis. The function is called autocorrelation because the scattering intensity patterns are correlated with themselves. The decay of correlation over time is monitored. A correlation graph that has a short decay time, i.e., has an approximately exponential decay, is indicative of fast and efficient diffusion and consequently of small particles [75, 79]. The Einstein-Langevin equation describes how the diffusivity D of particles is inversely proportional to their hydrodynamic diameter [80, 81]:

$$D = \frac{k_B K_T}{3\pi\eta d} \tag{5}$$

where k_B is Boltzmann's constant, K_T is the absolute temperature, η is the dynamic viscosity of the liquid, and d is the hydrodynamic diameter of the particle. From this equation follows that a smaller hydrodynamic diameter leads to higher diffusivity of a particle.

The correlation has a theoretical limit of 1.0 [78]. The correlator in the DLS instrument compares the similarity of the scattering intensity signal initially (t=0) and at a later point in time (t) [82]. The theoretical limit of 1.0 is impossible to achieve in practice, because this would imply the system had zero noise. In general, the closer the correlation coefficient is to 1.0 at t=0, i.e., at the y-axis intercept, the greater the data quality and the less noise is present.

Using an ultra-low concentration of sample when conducting a DLS analysis can lead to an inaccurate size distribution due to number concentration fluctuations adding a non-Gaussian term to the autocorrelation function [83]. In addition, weak scattering from the particles and noisy measurement results tend to occur when low particle concentrations are used [84]. On the other hand, the result of using very high particle concentrations can be distorted measurements due to particle-particle interactions. Since DLS analysis is limited to transparent samples, a much-used method to determine an appropriate concentration is to choose a clear or low-opacity sample.

Another metric used to compare the signal strength from different samples is the derived count rate (DCR) [81, 85]. DCR is defined as the theoretical count rate that could be obtained at 100% laser power with zero attenuation. Higher concentrations and/or larger particles are typically associated with a high DCR. The unit of DCR is kilo counts per second (kcps).

2.10 Multi-angle light scattering

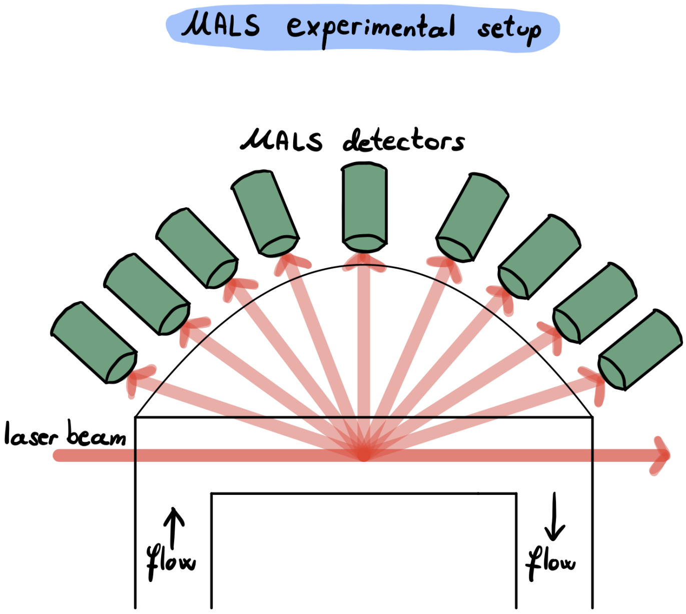

Figure 13: The experimental setup for MALS. Figure based on [86].

Multi-angle light scattering (MALS) is a static light scattering method [87]. The experimental setup for MALS is displayed in Figure 13. With MALS, the intensity of scattered light is computed at different scattering angles. MALS is a characterization technique that allows for the weight average molecular weight (M_w) of particles to be calculated based on the scattering intensity measured and the particle concentration. In 1948, Bruno Zimm [88] developed a theoretical foundation which resulted in a straightforward equation condensing the Rayleigh-Debye-Gans theory of light scattering. In addition, Philip Wyatt [89] composed a review article in which Zimm's developments were discussed [1]. This is known as the Zimm equation:

$$\frac{Kc}{R(\theta, c)} = \frac{1}{M_w P(\theta)} + 2A_2 c \tag{6}$$

- $R(\theta, c)$ is a function of the scattering angle θ and solute concentration c, and describes the solution's excess Rayleigh ratio
- M_w is the weight average molecular weight of the solute
- A_2 is the second virial coefficient
- K is the constant $\frac{4\pi^2 (dn/dc)^2 {n_0}^2}{N_a {\lambda_0}^4}$
- N_a is Avogadro's number

---

[1] A summary article on MALS theory from Wyatt Technology [90] has been used as supporting literature in addition to the works of Zimm [88] and Wyatt [89].

- dn/dc is the refractive index increment
- n_0 is the refractive index of the solvent
- λ_0 is the wavelength in vacuum of the laser
- $P(\theta)$ describes the scattered light's angular dependence, and can be related to the rms-radius

The first order expansion of $P(\theta)$ gives:

$$P(\theta) \approx 1 - \frac{16\pi^2 {n_0}^2}{3{\lambda_0}^2} < {r_g}^2 > sin^2(\frac{\theta}{2}) + O(sin^4(\frac{\theta}{2})) \tag{7}$$

Here, r_g is the rms-radius. Using the slope at $\theta = 0$ of the measured ratios $\frac{1}{R(\theta,c)}$ with respect to $sin^2(\frac{\theta}{2})$, ${r_g}^2$ can be calculated. For $r_g > 50$ nm, higher moments need to be included in the expansion. Further, the mass M of a macromolecule may be derived from ${r_g}^2$ and the elements m_i which the mass M consist of:

$$< {r_g}^2 >= \frac{\sum_i {r_i}^2 m_i}{\sum_i m_i} = \frac{1}{M}\sum_i {r_i}^2 m_i \tag{8}$$

r_i is the element m_i's distance from the mass center of the macromolecule with mass M. This is essentially how the Zimm equation can be used to determine the molar mass of a macromolecule, and the basis for MALS characterization. An important factor in this is that the Zimm equation holds true for all scattering angles, which is utilized by today's modern light scattering instruments that collect data from a range of scattering angles.

A simplified version of the Zimm equation can be applied for particles with dimensions less than $\lambda_0/20$, since the angular dependence factor can be abandoned in this case:

$$\frac{Kc}{\Delta R} = \frac{1}{M_w} + 2A_2c \tag{9}$$

The second virial coefficient[2] A_2 is a thermodynamic quantity [91]. It is used to describe a solution's deviation from ideal conduct, and to forecast and explicate thermodynamic properties [92]. Such properties include solubility, crystallization conditions, and the tendency to aggregate. The more A_2 deviates from zero, the further a solution diverges from being classified as a θ-solvent [93]. $A_2 = 0$ is the value of A_2 in theory providing the most accurate molar mass measurements [94]. $A_2 < 0$ are attractive interactions, and implies a perceptible increase in molar mass. This is due to an increase in scattering intensity faster than linear (i.e., $A_2 = 0$). Conversely, repulsive attractions seen as $A_2 > 0$ implies a detectable decrease in molar mass, owing to a slower than linear increase of the scattering intensity. In practice, the value of A_2 can be determined through bulk experiments, e.g., through MALS-analysis [92]. The unit of A_2 is $[cm^3 \cdot mol/g^2]$.

The refractive index increment dn/dc is a constant used in MALS to calculate the concentration and M_w of polymers [95]. dn/dc concerns how the refractive index varies with solute concentration, and is determined by a variety of parameters. These comprise polymer structure, type of solvent, wavelength of the scattering light, and solution temperature. Given these parameters, to obtain an accurate measurement of dn/dc, the measurements must be carried out at the same conditions as the MALS experiment for which the dn/dc is needed.

2.11 Combining AFM, SEM, DLS, and MALS

Carrying out a comprehensive characterization of a certain type of sample often require several characterization techniques to be employed in conjunction. For the G_m-b-Dex_n NPs that have

---

[2] Many works refer to the second virial coefficient as B or B_2.

investigated in this work, the characterization methods AFM, SEM, DLS, and MALS have been employed. Table 1 summarizes Sections 2.7, 2.8, 2.9, and 2.10 in terms of practical use of the different characterization methods.

Characterization method	**Key information about NPs**
AFM	Topography (size and shape)
SEM	Topography and chemical composition
DLS	Size distribution
MALS	Molar mass
**	**Key advantage**
AFM	Great resolution at nm scale
SEM	Array of signals emitted
DLS	Quick and simple
MALS	Determine molar mass
**	**Key drawback**
AFM	Time-consuming
SEM	Condutive sample required
DLS	Low resolution
MALS	Highly concentration-sensitive

Table 1: Summary and comparison of AFM, SEM, DLS, and MALS for characterization of G_m-b-Dex_n NPs.

3 Experimental

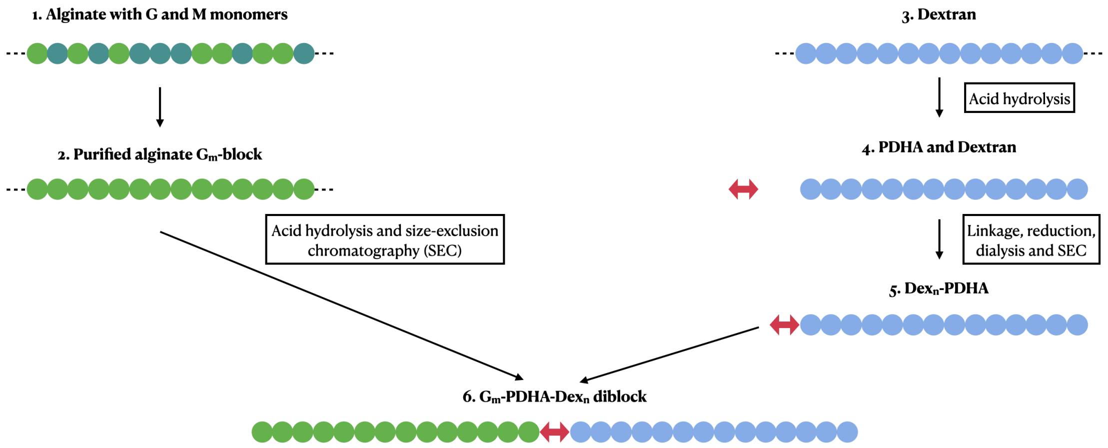

Figure 14: Figure summarizing chapters 3.1.1, 3.1.2, 3.1.3, and 3.1.4.

3.1 Preparation of diblock copolymer

In the work on this Master's Thesis, previously made diblock copolymers were used. G_{16}-b-Dex_{32}, G_{16}-b-Dex_{43}, and G_{37}-b-Dex_{43} diblocks used in subsequent experimental steps were provided by Elise Holmås. G_{19}-b-Dex_{45} diblocks were provided by Victor Zylla Fæster. However, the preparation of the diblock copolymers are part of the basis for this thesis, and is therefore included in the experimental part of this thesis. The Sections 3.1.1, 3.1.2, 3.1.3, and 3.1.4 on the preparation of diblock copolymers are directly aquired from the author's Project Thesis [13], where diblock copolymers were in fact prepared. Figure 14 summarizes these sections.

3.1.1 Preparation of alginate G-blocks

Alginate powder (1 g) provided by Professor Kurt I. Draget was diluted in Milli-Q (MQ) water (25 ml) and mixed overnight using a magnetic stirrer. pH was reduced to 2.8 using HCl (15 ml, 0.5 M), to achieve precipitation of G-blocks. A pH-meter was used to monitor the changes in pH. The solution was mixed (3 hours) using a magnetic stirrer. The sample was filled onto centrifuge tubes (50 ml) and centrifuged 3 times, each time at 1750 RCF for 5 min. The centrifuge instrument used was the Allegra X-15R Centrifuge from Beckman Coulter. Liquid was removed after the first two runs, leaving a pellet of alginate at the bottom of the centrifuge tube. First run, the sample with pH 2.8. Second run, the pellet with HCl (10 ml, 0.1 M). Third run, the pellet and MQ (10 ml). The solution was neutralized using NaOH (0.5 M). NaOH was added carefully to the solution while monitoring pH with a pH-meter. Finally, pH 6.8 was achieved. The solution was filtrated (0.45 μm).

Acid hydrolysis was done next. Using HCl (0.1 M) and a pH-meter, pH was lowered to 3.6. The sample was put in a water bath (95 $°C$, 7 hours). The sample was taken out of the bath and cooled down to room temperature. NaOH (0.1 M) was used to neutralize to pH 6.95. The sample was put into two centrifuge tubes (50 ml) and freeze dried. The dry sample was weighed in at 558.1 mg.

For SEC, 3 columns were used (HiLoad Superdex 30 prep grade 26/600 column, Cytiva, product no. 28989332). A HPLC pump (LC-10ADVP, Shimadzu), an RI-detector (R1-101, Shodex), and a fraction collector (FRAC-100, Pharmacia Fine Chemicals) were also included in the setup. The mobile phase used was ammonium acetate (0.1 M, pH 6.9). The wait was set to 400 min, delay/flow rate to 0.8 ml/min, and the fraction size to 6.32. The sample was dissolved in NaCl buffer solution (15 ml, 0.1 M, pH 6.8). The solution was filtrated (0.45 μm). 186 mg / 5 ml was sent through per run. Through analysis of the chromatograms from the 3 runs of SEC, the chromatogram with the highest peaks was chosen to select fractions from. 7 fractions were chosen to keep, and put into separate glasses. Centricon Plus-70 devices (Millipore/Merck, MWCO 3 kDa, product no. UFC700308) were used for dialysis and concentration of the sample. The same centrifugation process was repeated for all the collected fractions. First, the device was filled with sample (10 ml) and centrifuged (5 min, 3500 RCF). Second, the device was turned around and centrifuged (2 min, 1000 RCF). Third, the device was centrifuged (20 min, 3500 RCF). Fourth, the device was centrifuged (30 min, 3500 RCF). Fifth, the device was washed with MQ and centrifuged 3 times (5 min, 3500 RCF).

The fractions were freeze dried. DP_n was verified by NMR. In the NMR tube, dry sample (5 mg) was mixed with D_2O (500 μl, Sigma-Aldrich, 99.9 atom % D, product no. 151882). The sample was analyzed in the Bruker Ascend 600 MHz NMR instrument.

3.1.2 Preparation of dextran

Dextran T 2000 (Pharmacia Fine Chemicals) was used as starting material. Dextran was diluted to a concentration of 25 mg/ml after acid hydrolysis. Dextran (3 g) was mixed with MQ (30 ml) and put on a magnetic stirrer overnight. For the acid hydrolysis, the water bath was heated up (95 $°C$). The solution of dextran in MQ, and HCl (30 ml, 0.1 M), were heated up separately. When both solutions had reached about 95 $°C$, they were mixed together and put in the water bath (95 $°C$, 150 min). The solution was taken out of the water bath and cooled down to room temperature. To neutralize the solution, NaOH (60 ml, 0.05 M) was added. Two Centricon devices were used to concentrate the dextran-solution further. Samples (60 ml) were filled into each Centricon device, and centrifuged (30 min, 3500 RCF). Next, two runs to wash with MQ (20 min, 3500 RCF). The remaining solution was filled onto centrifuge tubes (50 ml), with around 15 ml solution in each tube. The samples were freeze dried. The freeze dried sample weighed in at 0.8239 g. DP_n was verified by NMR. In the NMR tube, dry sample (5 mg) was mixed with D_2O (500 μl). The sample was analyzed in the Bruker Ascend 600 MHz NMR instrument.

3.1.3 Preparation of dextran-PDHA

All dry dextran (0.8239 g) was used in this step. To achieve a concentration of 7 mM dextran, 24 ml total liquid was used. PDHA was wanted in a tenfold concentration, i.e., 70 mM. To achieve this, PDHA in powder form (178 mg, Sigma-Aldrich, O,O′-1,3-Propanediylbishydroxylamine dihydrochloride 98 %, product no. 689122) was added to the liquid. Due to pH adjustment, 22.4 ml of the liquid consisted of sodium acetate buffer (0.5 M), and 1.6 ml consisted of NaOH-solutions used to bring the pH to 4.0. The resulting solution was put on a magnetic stirrer (24 hours).

Next, Dex-PDHA was reduced using 2-Picoline borane complex (Sigma-Aldrich, 95 % PB, product no. 654213). PB was used in a twenty-fold concentration in relation to dextran, i.e., 140 mM. PB powder (359.4 mg) was added to the Dex-PDHA solution, and put on a magnetic stirrer (5 min). The solution was put in a water bath (40 $°C$, 72 hours).

The solution was taken out of the water bath and prepared for dialysis with a dialysis bag (Spectrum, Spectra/Por 3 Dialysis Membrane, MWCO 3.5 kDa, flat width 45 mm). For the solution volume of 24 ml, a dialysis bag (10 cm) was cut up and soaked in MQ (30 min). After 30 minutes, one end of the dialysis bag was clipped shut with a dialysis clip, and the inside of the bag was rinsed with MQ. The solution was filled into the bag and the other end of the bag was also clipped shut with a dialysis clip. The bag was put in a bucket with MQ (7 l) and NaCl (50 mM, 20.46 g). The bucket was put on a magnetic stirrer at low speed. Dialysis against MQ and salt was done 5 times, followed by two rounds of dialysis against MQ. The conductivity of the bucket contents was 1.03 μS/cm when the dialysis ended. The sample was collected from the dialysis bag and put into two centrifuge tubes (50 ml), with roughly 17 ml of the sample in each tube, and freeze dried.

The dry sample weighed 611 mg. Sample (188 mg) was mixed with NaCl buffer (4 ml, 0.1

M, pH 6.8). The solution was filtrated (0.45 μm). Two runs of SEC was done, each with 200 mg dry sample and 4 ml NaCl buffer solution (0.1 M). 8 fractions were chosen from the resulting SEC chromatogram, and collected onto flasks.

Four Centricon devices were used to concentrate the Dex-PDHA fractions. First, solutions (40 ml) were filled into each device, and centrifuged (20 min, 3500 RCF). Second, the rest of the solution was used to refill, and centrifuged (20 min, 3500 RCF). Third, the devices were washed with MQ (20 ml)(10 min, 3500 RCF). The washing was repeated once more. This was repeated for the remaining 4 fractions, due to space limitations in the centrifuge instrument. The fractions were freeze dried.

DP_n was verified by NMR. In the NMR tube, dry sample from fraction D (4.4 mg) was mixed with D_2O (500 μl). The sample was analyzed in the Bruker Ascend 600 MHz NMR instrument.

3.1.4 Preparation of G_m-b-Dex_n

This process is identical to Section 3.1.3, except for a few differences. Dex-PDHA is added in 3x excess to G-block, and linked for 24 hours. The solution is then reduced with 10x excess of PB for 24 hours [3].

3.2 Self-assembly of NPs

3.2.1 Dialysis

This section is in part adapted from the author's Project Thesis [13]. Subsequent dialysis of the NPs against MQ was new for the Master's Thesis work.

G_m-b-Dex_n diblocks were dissolved in NaCl buffer (10 mM) to a concentration of 4 mg/ml, and put on a tube rotator overnight. The G_m-b-Dex_n solution was filtrated (0.45 μm), and dialysed (Spectrum, Spectra/Por Float-A-Lyzer G2 1 ml, MWCO 3.5-5 kD) against $CaCl_2$ (20 mM) and NaCl (10 mM) on a magnetic stirrer overnight. Before use, the device was soaked in ethanol (10 %, 10 min), and in MQ (20 min).

One experiment included subsequent dialysis of the NPs against MQ after dialysis against $CaCl_2$ and NaCl. The same dialysis device (Spectrum, Spectra/Por Float-A-Lyzer G2 1 ml, MWCO 3.5-5 kD) was used, it was just transferred from the buffer solution to a beaker containing MQ. The beaker was put on a magnetic stirrer for 48 hours.

3.2.2 Direct titration

For direct titration, G_m-b-Dex_n diblocks were dissolved in NaCl (10 mM) overnight to a concentration of 8 mg/ml. This was done to achieve a concentration of 4 mg/ml upon addition of the same volume of ion stock solution and/or MQ. Before direct titration, the diblock solutions were filtrated (0.45 μm).

The stock solution used for the direct titration was Ca^{2+}/Ba^{2+} in a 1:1 ratio (3.75 mM of each ion). The stock solution was first mixed with MQ. The stock solution and/or MQ was then added to the diblock copolymer solution and immediately mixed on a vortex mixer. An Excel spreadsheet was used to calculate the different amounts that were required to achieve the different saturation percentages, see the Appendix Section A. Saturation percentage refers to how saturated the dissolved diblocks are with divalent cations, i.e., to which degree NPs have assembled. 0 % saturation indicates pure diblock form, 80 % saturation expresses that 80 % of diblocks should have assembled to NPs, and 120 % saturation denotes an over-saturation of cations, and all diblocks should have assembled to NPs.

---

[3] This step was not done by the author in their Project Thesis due to very low yield of fractionated Dex-PDHA.

The solutions were kept at room temperature for a specific amount of time before samples were examined, see Section 4 for how the individual samples were treated.

3.3 Characterization of NPs

3.3.1 DLS

NP solution (100 μl) was placed in a cuvette (Sarstedt, UV-Transparent Disposable Cuvettes for use from 220 nm, dimensions: 12.5 x 12.5 x 45 mm) and placed in the DLS instrument (Malvern Panalytical, Zetasizer Nano ZS). In the instrument's software, "measure → manual" was chosen, and different variables chosen depending on the goal of the measurement. After measurement, the data was exported to Excel for further data analysis, see the Appendix Section B.

3.3.2 MALS with flow injection

G_m-b-Dex_n diblocks were dissolved overnight in NaCl (10 mM) to a concentration of 8 mg/ml (for direct titration) or 4 mg/ml (for dialysis). The solution was then filtrated (0.22 μm). NP solutions were prepared either by dialysis, see Section 3.2.1, or by direct titration, see Section 3.2.2. A concentration series was prepared. The solutions were filled onto syringes (5 ml) and subsequently injected into the light scattering detector (Wyatt Technology, Dawn Heleos II) using a syringe pump. The dialysate was used as the buffer solution for the dialysed NP solutions. For the NP solutions made by direct titration, NaCl (10 mM) was used as the buffer solution. For the standard samples (pullulan and dextran), the buffer consisted of $NaNO_3$ (0.15 M) and Ethylenediaminetetraacetic acid (EDTA) (10 mM) with pH 6. To achieve as accurate concentrations of the standard samples as possible, the dry substances were placed in a dessicator overnight to remove moisture, before being weighed, mixed with MQ, and put on a tube rotator overnight. Before preparing the concentration series, the solutions were filtrated (0.22 μm).

The software Astra (Wyatt Technology) was used to collect the data from the light scattering detector. The collection procedure chosen was "Basic collection". After the collection was finished, the method "batch (Debye plot)" was added to the experiment file. Baselines and peaks were defined, see the Appendix Section C for an example. From "Report (summary)" the molar mass moments of the peaks were noted. This data was exported to Excel for further data analysis, see the Appendix Section C. In Excel, a Debye-plot was constructed using Equation 9. A linear trend line was added to the data points. From the y-intercept, M_w of the NPs was obtained, while the slope provided A_2.

3.3.3 AFM

This section is in part adapted from the author's Project Thesis [13]. The addition of vacuum drying as a process step was new for this work.

The following procedure was done in an ISO-7 cleanroom environment to avoid contamination of the sample. From G_m-b-Dex_n NP stock solutions (4 mg/ml), diluted solutions (e.g., 1.0 mg/ml, 0.2 mg/ml) were prepared using deionized water, and mixed using a vortex mixer. The solutions (5 μl) were deposited on mica discs (Ted Pella, highest quality grade V1, diameter 15 mm, product no. 50-15) and gently dried with N_2 gas. The samples were stored in wafer holders at room temperature. The NP solutions were stored at $4°C$.

Selected samples were subject to an additional drying step using a vacuum oven (Binder VD23). The pressure was set to 300 mbar, and the hysteresis to 10 mbar. The temperature was set to either $50°C$ or $120°C$. The former if samples for SEM were prepared at the same time, and the latter if only AFM samples were prepared [4]. The sample was immediately placed in the oven

---

[4] Grade V1 muscovite mica has a maximum operating temperature of 600-700$°C$ [96], while carbon tape can withstand up to $60°C$ [97].

(i.e., before the oven reached the set temperature) and stayed there for 3 hours.

The AFM analysis was done using the Dimension Icon instrument from Bruker. The mode ”ScanAsyst Air” was chosen and the probe tip used was the SCANASYST-AIR [98]. The probe is a silicon tip on nitride lever, its spring constant is 0.4 N/m, resonance frequency is 70 KHz, and the tip radius is 2 nm. All probe values are nominal. The scan size was set to 500 nm.

The AFM data was analyzed using the software Gwyddion. The tools ”Align rows using various methods” and ”Stretch color range to part of data” were used to increase the quality and contrast of the images. To measure the diameter of particles, the tool ”Measure distances and directions between points” was used. See the Appendix Section D for a figure that highlights the tools in the software layout.

3.3.4 SEM

Diluted NP solutions were prepared as described in Section 3.3.3. The solutions (5 μl) were deposited on carbon tape (Ted Pella, PELCO Tabs, Carbon Conductive Tabs, 9mm OD, product no. 16084-3) fastened onto SEM-stubs (vacuum grade aluminum) and gently dried with N_2 gas.

Selected samples were subject to an additional drying step using a vacuum oven (Binder VD23). The settings were the same as described in Section 3.3.3, though the temperature used was $50°C$ because of the thermal range of carbon tape [97].

The SEM-samples were coated with platinum/palladium (5 nm) using a sputter coater (Cressington 208HR). For the characterization, the Thermo Fisher Scientific Apreo 2 SEM was used. The specific magnifications, acceleration voltages, beam currents, and detectors used are provided in the SEM images found in Section 4.4. The SEM images were saved as .tif-files and opened directly in Preview on Mac.

3.4 Regeneration of diblocks

The NPs can be regenerated to diblock form by acid dialysis. First, a dialysis bag (Spectrum, Spectra/Por 3 Dialysis Membrane, MWCO 3.5 kDa, flat width 45 mm) was cut out according to the volume of the NP solution. The dialysis bag was soaked in MQ (30 min). After 30 minutes, one end of the dialysis bag was clipped shut with a dialysis clip, and the inside of the bag was rinsed with MQ. The NP solution was filled into the bag and the other end of the bag was also clipped shut with a dialysis clip. The dialysis bag was put in a beaker containing HNO_3 (0.2 M), on a magnetic stirrer overnight in a ventilated fume hood. Subsequently, dialysis against MQ was done 3 times before pH was balanced to 6/7. The diblock solutions were freeze dried.

4 Results

Unless noted otherwise, dialysis refers to the dialysis against 20 mM $CaCl_2$ and 10 mM NaCl, as per the procedure described in Section 3.2.1. Direct titration refers to the addition of Ca^{2+} and Ba^{2+} ions, as per the procedure described in Section 3.2.2.

4.1 DLS results

Unless otherwise specified, 5 measurements with 8 runs each were done for each sample. In the case that one of the 5 measurements diverged greatly from the others, this measurement was left out of the final data analysis. The data was collected using the Malvern Zetasizer Nano software, and processed in Excel. The Excel setup used can be found in the Appendix Section B.

4.1.1 G_{16}-b-Dex_{32} NPs by dialysis

G_{16}-b-Dex_{32} NPs (4 mg/ml) were prepared by dialysis. The particles had an average size of 25 nm, and average derived count rate of 1813 kcps.

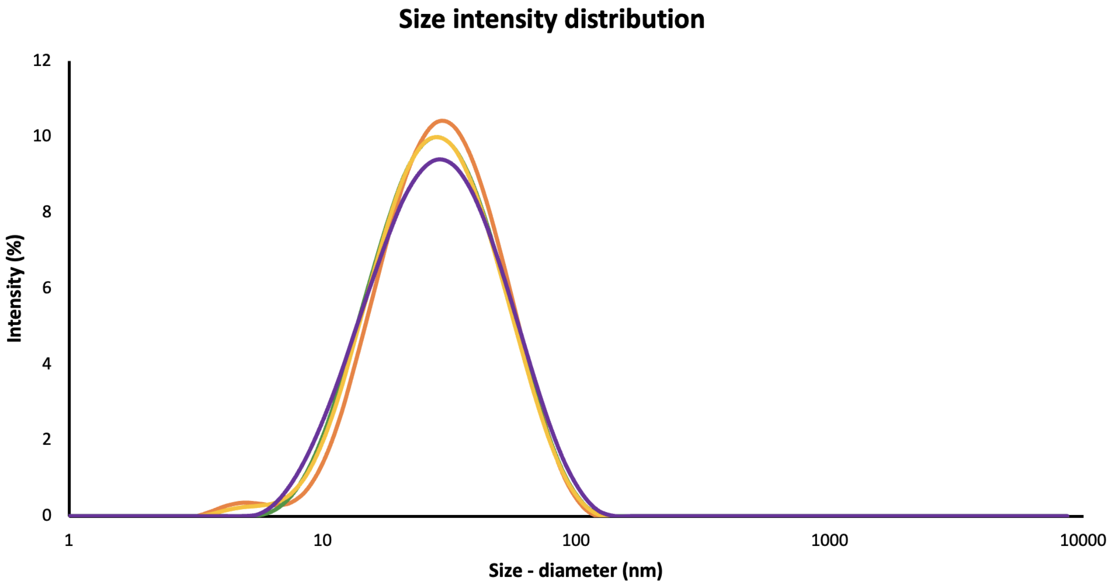

Figure 15: Size distribution of the 4 mg/ml G_{16}-b-Dex_{32} NPs prepared by dialysis.

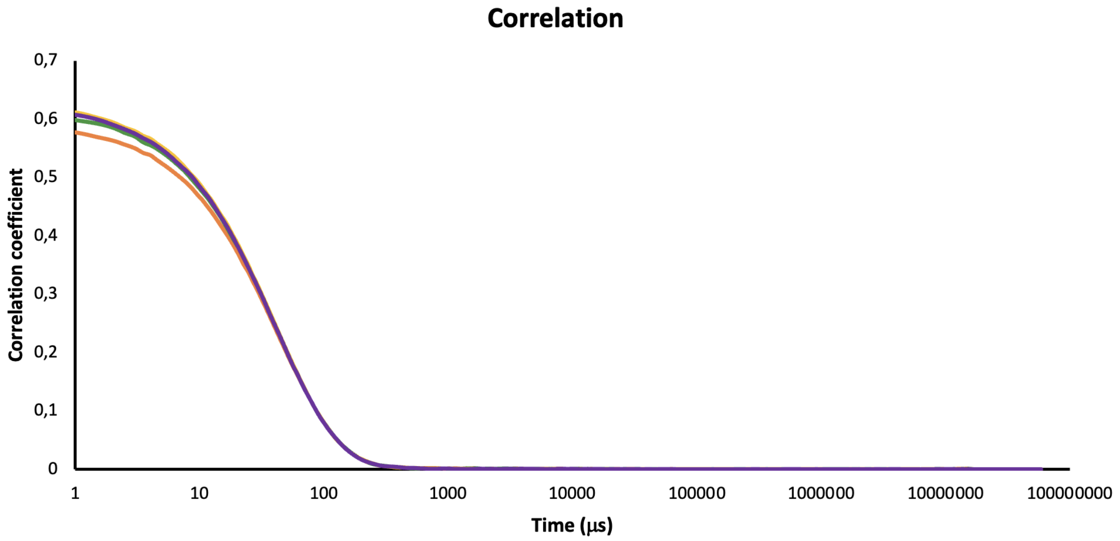

Figure 16: Correlation of the 4 mg/ml G_{16}-b-Dex_{32} NPs prepared by dialysis.

4.1.2 G_{16}-b-Dex_{32} NPs by direct titration

This experiment was carried out together with Elise Holmås. G_{16}-b-Dex_{32} NPs were prepared to a concentration of 4 mg/ml by 1h direct titration using 0% [5], 80%, and 120% saturation of Ca/Ba stock solution.

% saturation Ca/Ba	Average size (nm)	Average derived count rate (kcps)
0	46	1419
80	18	3123
120	24	2791

Table 2: The average size and average derived count rate of the 4 mg/ml G_{16}-b-Dex_{32} NPs prepared by 1h direct titration.

---

[5] 0% saturation refers to the diblock form, where no cations have been added, i.e., no NPs have formed.

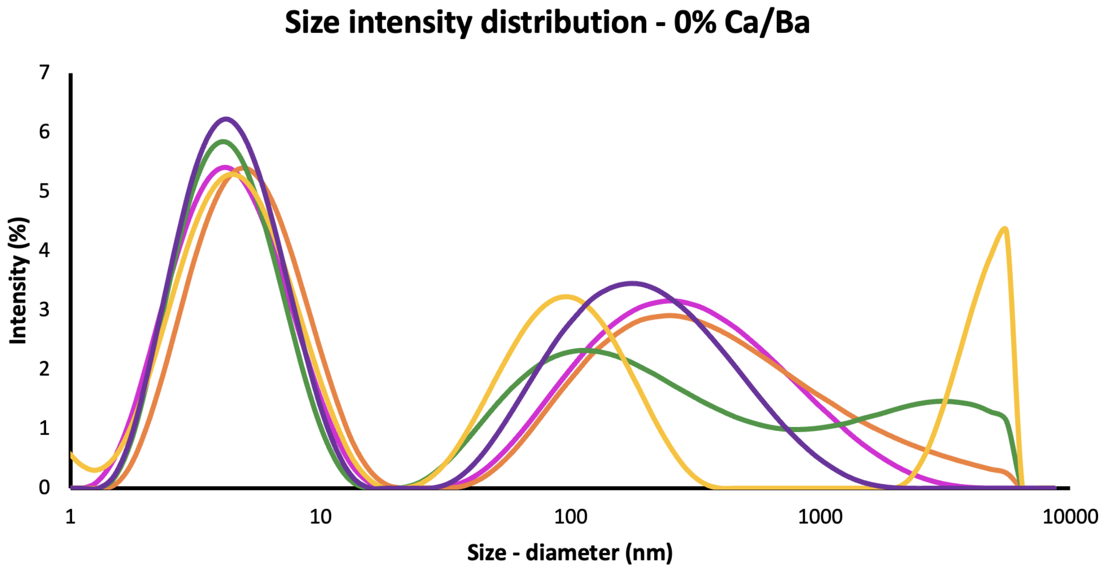

Figure 17: Size distribution of the 4 mg/ml G_{16}-b-Dex_{32} diblock with 0% saturation of Ca/Ba stock by 1h direct titration.

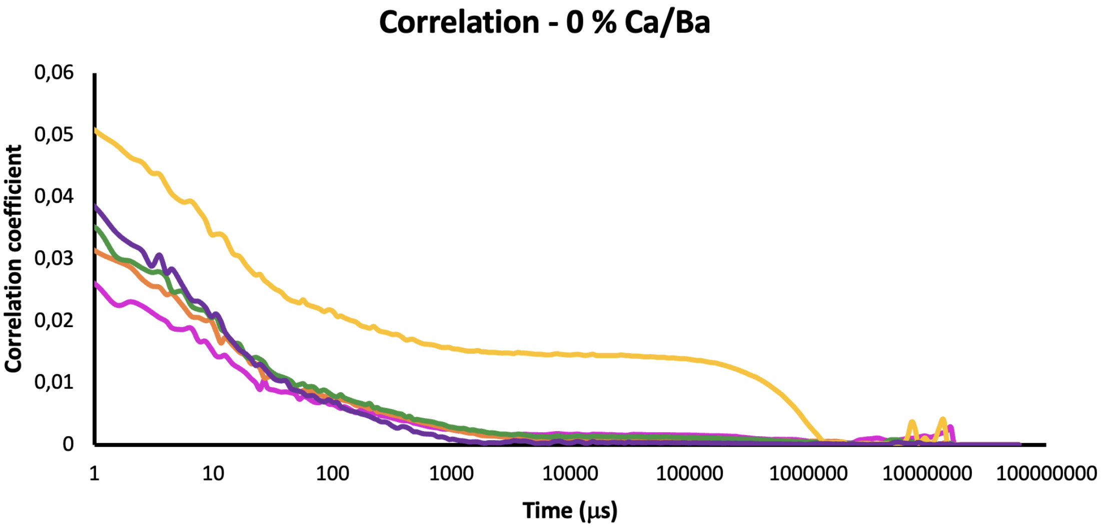

Figure 18: Correlation of the 4 mg/ml G_{16}-b-Dex_{32} diblock with 0% saturation of Ca/Ba stock by 1h direct titration.

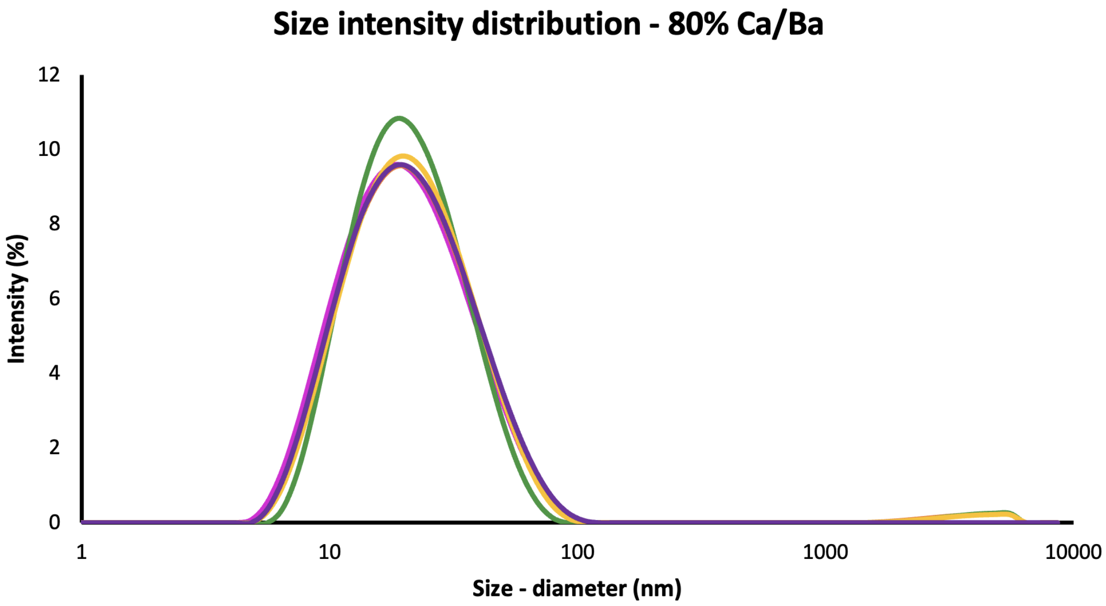

Figure 19: Size distribution of the 4 mg/ml G_{16}-b-Dex_{32} NPs with 80% saturation of Ca/Ba stock by 1h direct titration.

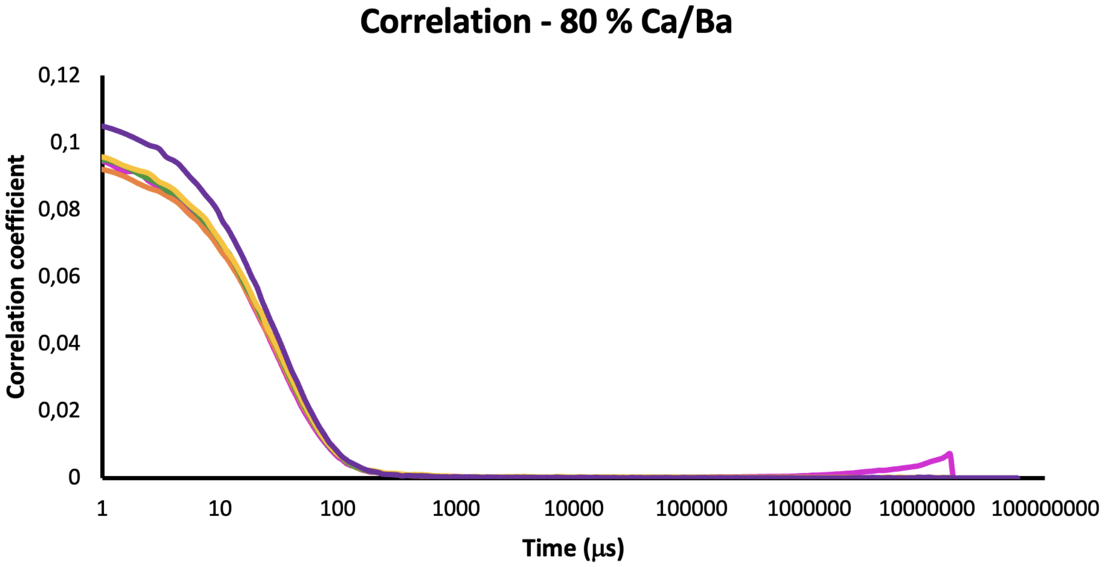

Figure 20: Correlation of the 4 mg/ml G_{16}-b-Dex_{32} NPs with 80% saturation of Ca/Ba stock by 1h direct titration.

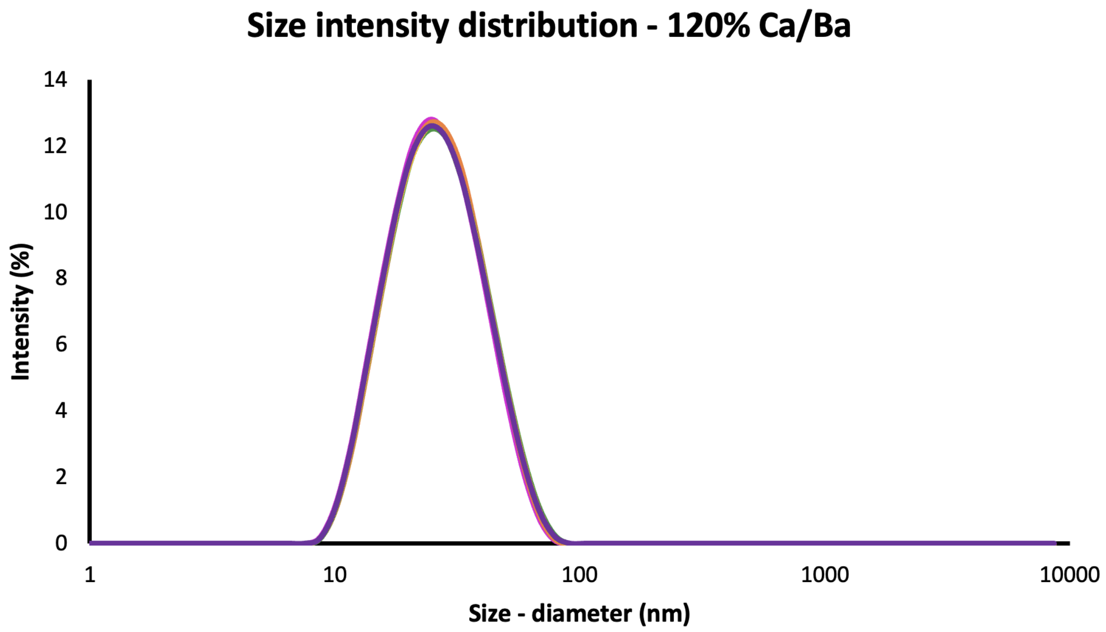

Figure 21: Size distribution of the 4 mg/ml G_{16}-b-Dex_{32} NPs with 120% saturation of Ca/Ba stock by 1h direct titration.

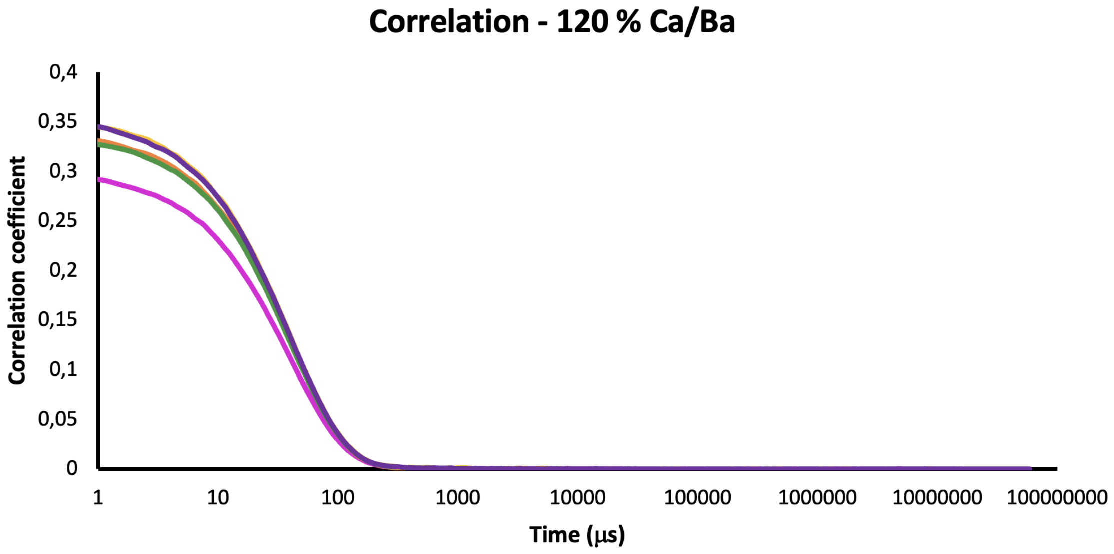

Figure 22: Correlation of the 4 mg/ml G_{16}-b-Dex_{32} NPs with 120% saturation of Ca/Ba stock by 1h direct titration.

4.1.3 G_{16}-b-Dex_{43} NPs by direct titration

This experiment was carried out by Elise Holmås. The experiment is included in this thesis since it directly relates to the previous experiment presented in Section 4.1.2. G_{16}-b-Dex_{43} NPs were prepared to a concentration of 4 mg/ml by 1h direct titration using 80% and 120% saturation of Ca/Ba stock solution. 3 measurements with 8 runs each were done in this case.

% saturation Ca/Ba	Average size (nm)	Average derived count rate (kcps)
80	17	530
120	17	1000

Table 3: The average size and average derived count rate of the 4 mg/ml G_{16}-b-Dex_{43} NPs prepared by 1h direct titration.

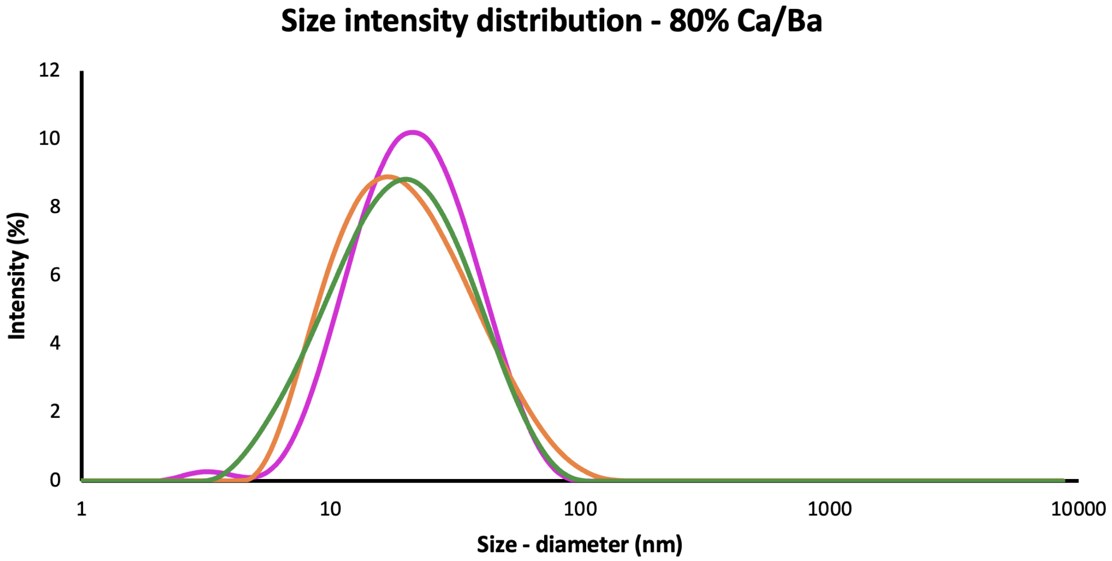

Figure 23: Size distribution of the 4 mg/ml G_{16}-b-Dex_{43} NPs with 80% saturation of Ca/Ba stock by 1h direct titration.

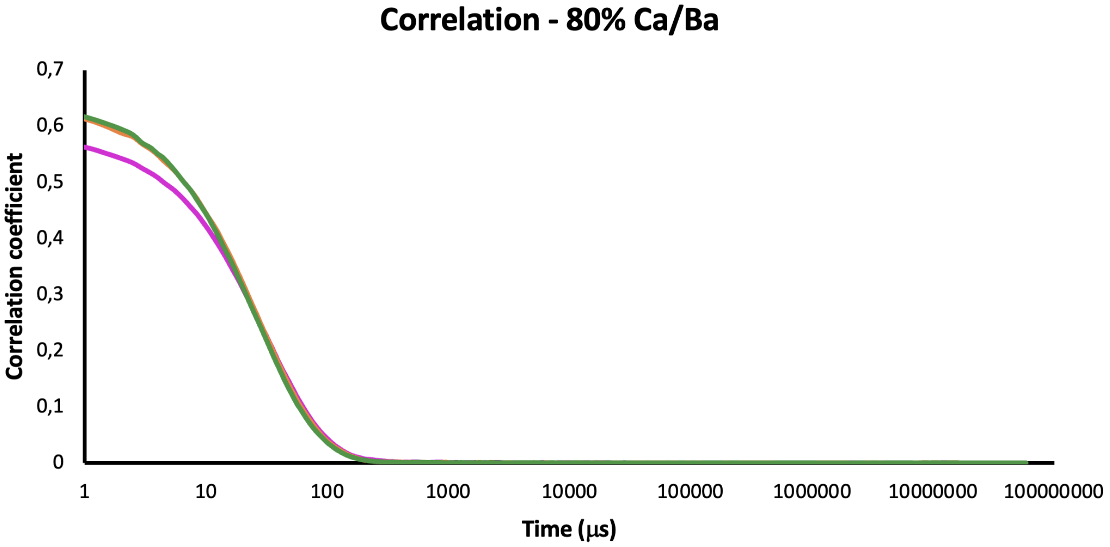

Figure 24: Correlation of the 4 mg/ml G_{16}-b-Dex_{43} NPs with 80% saturation of Ca/Ba stock by 1h direct titration.

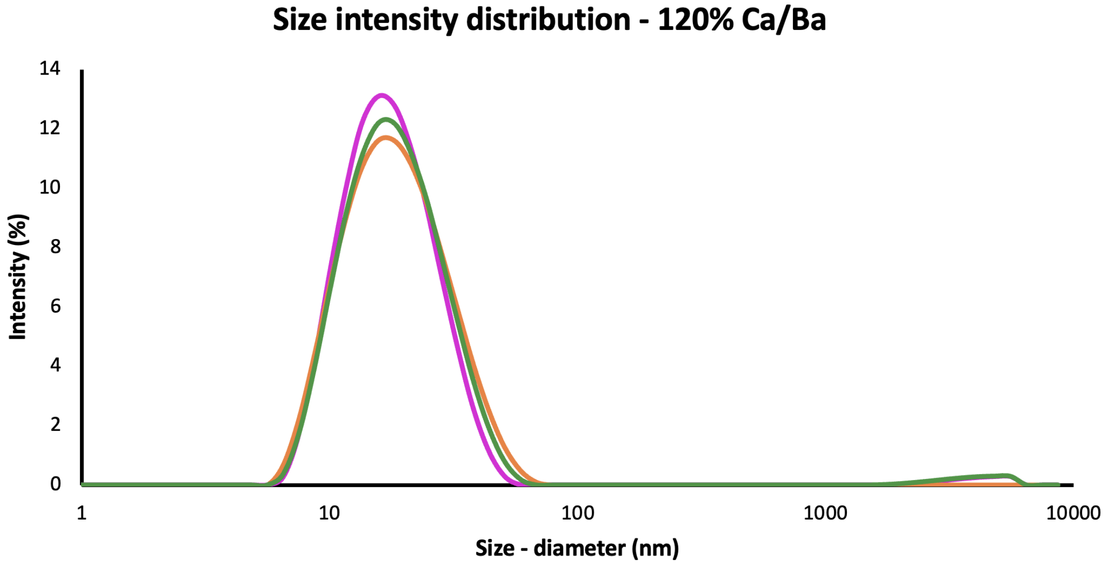

Figure 25: Size distribution of the 4 mg/ml G_{16}-b-Dex_{43} NPs with 120% saturation of Ca/Ba stock by 1h direct titration.

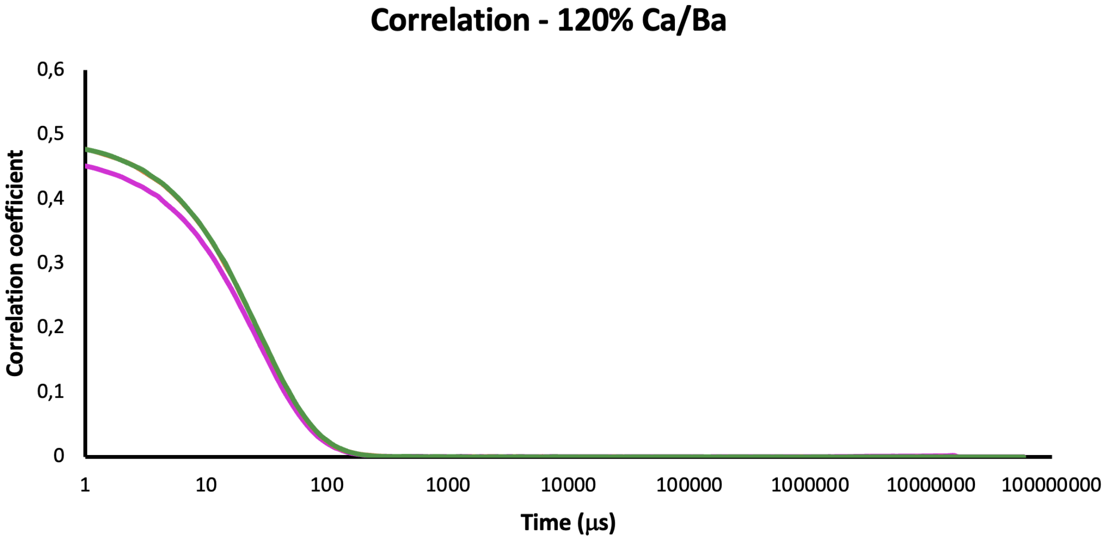

Figure 26: Correlation of the 4 mg/ml G_{16}-b-Dex_{43} NPs with 120% saturation of Ca/Ba stock by 1h direct titration.

4.1.4 G_{16}-b-Dex_{32} NPs by dialysis with buffer and MQ

G_{16}-b-Dex_{32} (4 mg/ml) was dialysed first against 20 mM $CaCl_2$ + 10 mM NaCl for 24h, and second against MQ for 48h.

Treatment	Average size (nm)	Average derived count rate (kcps)
Before MQ	28	2809
After MQ	72	3560

Table 4: The average size and average derived count rate of the G_{16}-b-Dex_{32} NPs before and after dialysis against MQ.

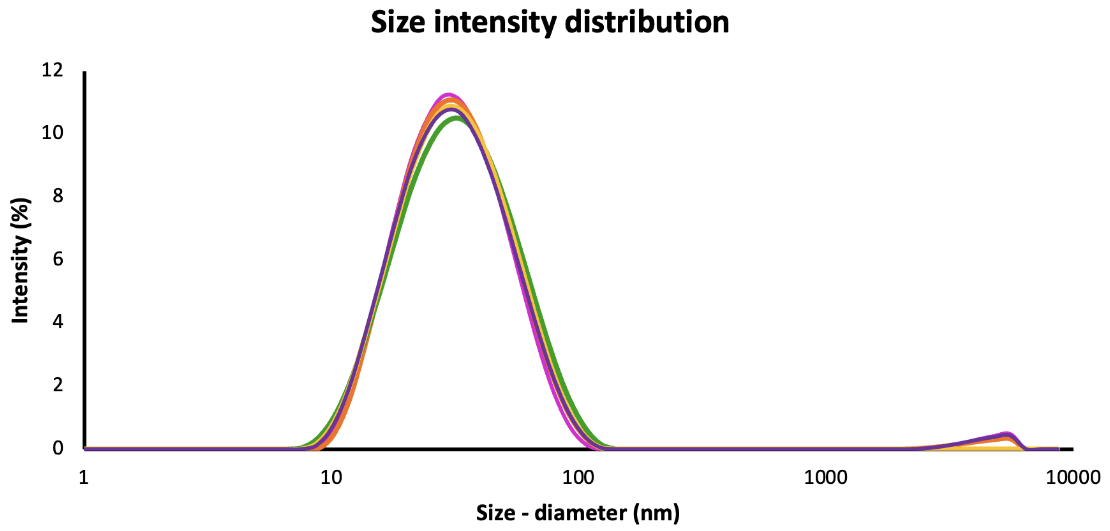

Figure 27: Size distribution of the NPs after dialysis against 20 mM $CaCl_2$ + 10 mM NaCl for 24h.

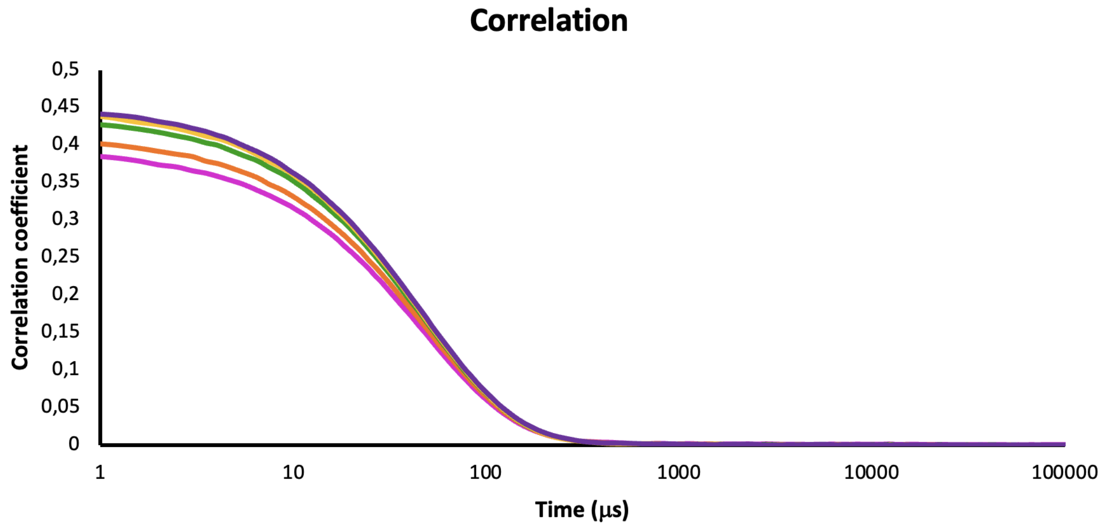

Figure 28: Correlation of the NPs after dialysis against 20 mM $CaCl_2$ + 10 mM NaCl for 24h.

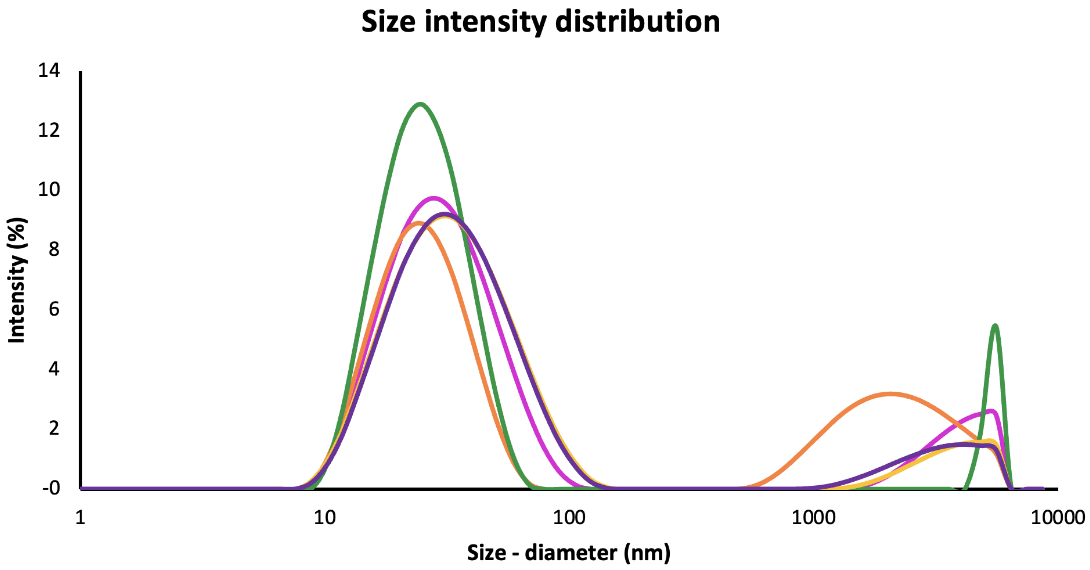

Figure 29: Size distribution of the NPs after dialysis against 20 mM $CaCl_2$ + 10 mM NaCl for 24h, and against MQ for 48h.

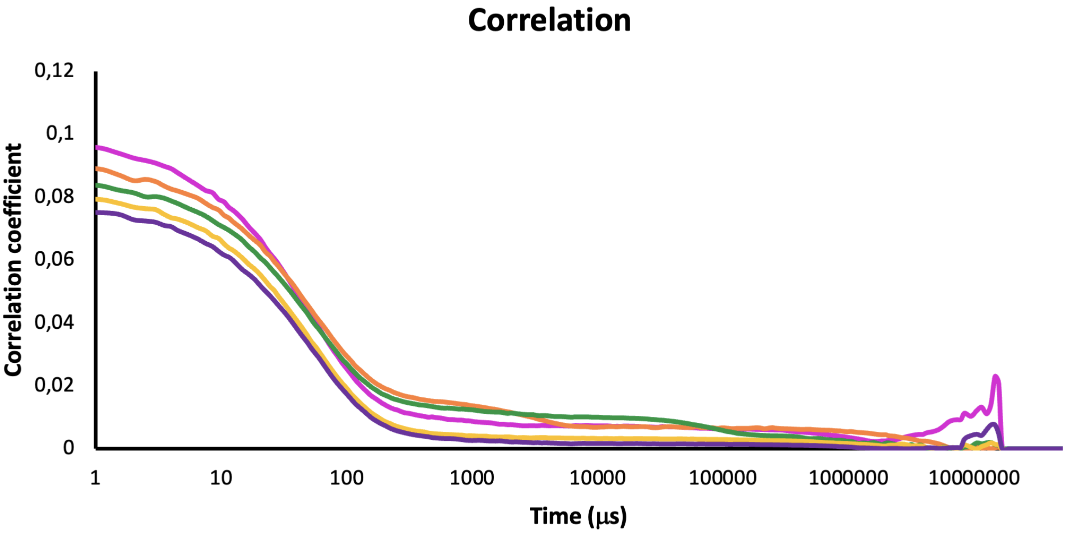

Figure 30: Correlation of the NPs after dialysis against 20 mM $CaCl_2$ + 10 mM NaCl for 24h, and against MQ for 48h.

4.1.5 G_{16}-b-Dex_{43}, G_{37}-b-Dex_{43}, and G_{16}-b-Dex_{32} NPs by dialysis

G_{16}-b-Dex_{43}, G_{37}-b-Dex_{43}, and G_{16}-b-Dex_{32} NPs were prepared to a concentration of 4 mg/ml by dialysis.

Sample	Average size (nm)	Average derived count rate (kcps)
G_{16}-b-Dex_{43}	29	3050
G_{37}-b-Dex_{43}	38	10985
G_{16}-b-Dex_{32}	25	2448

Table 5: The average size and average derived count rate of the different 4 mg/ml NPs prepared by dialysis.

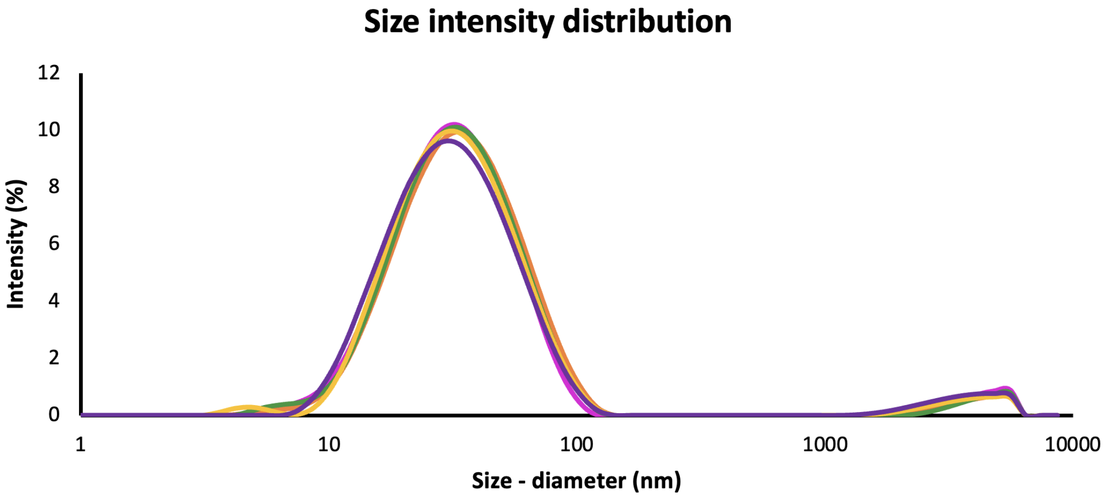

Figure 31: Size distribution of the 4 mg/ml G_{16}-b-Dex_{43} NPs prepared by dialysis.

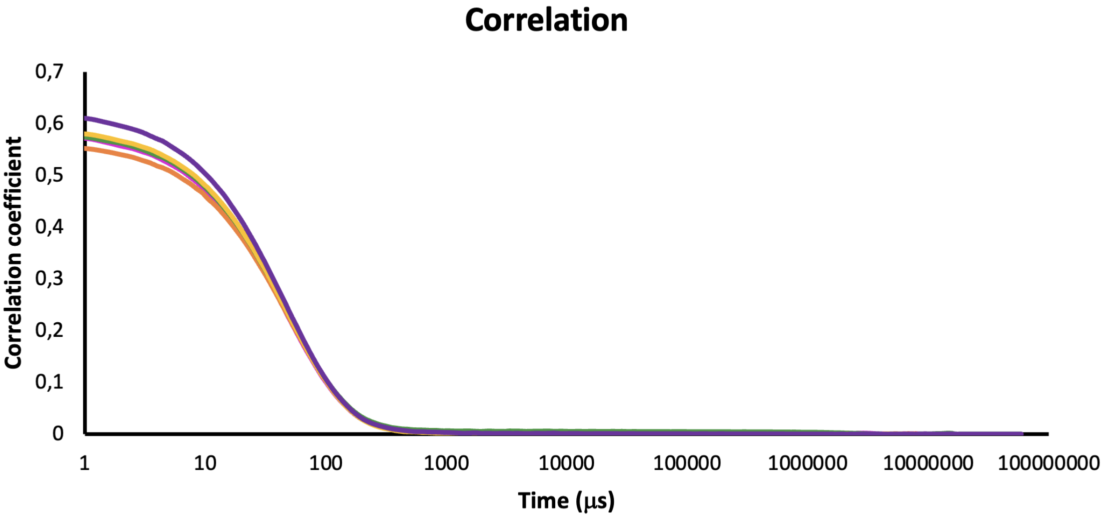

Figure 32: Correlation of the 4 mg/ml G_{16}-b-Dex_{43} NPs prepared by dialysis.

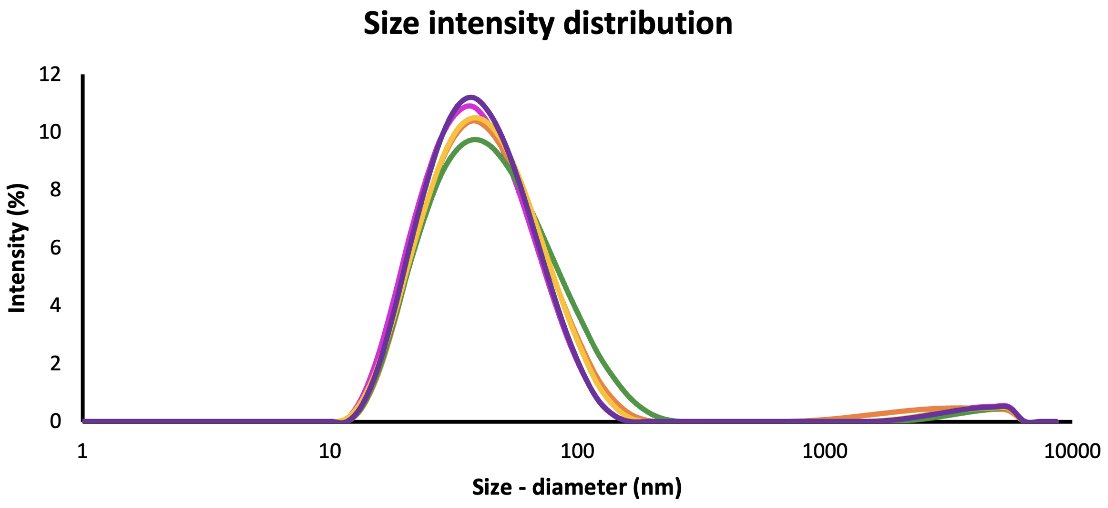

Figure 33: Size distribution of the 4 mg/ml G_{37}-b-Dex_{43} NPs prepared by dialysis.

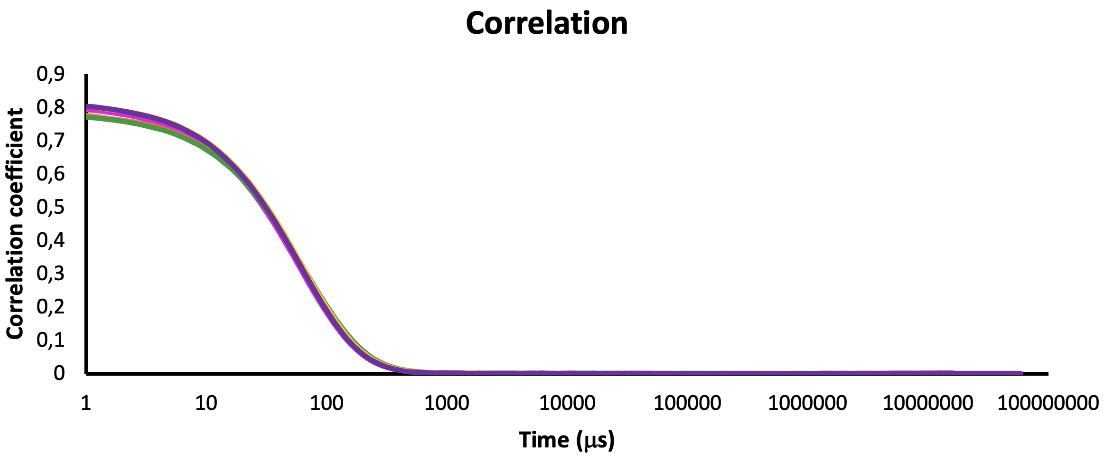

Figure 34: Correlation of the 4 mg/ml G_{37}-b-Dex_{43} NPs prepared by dialysis.

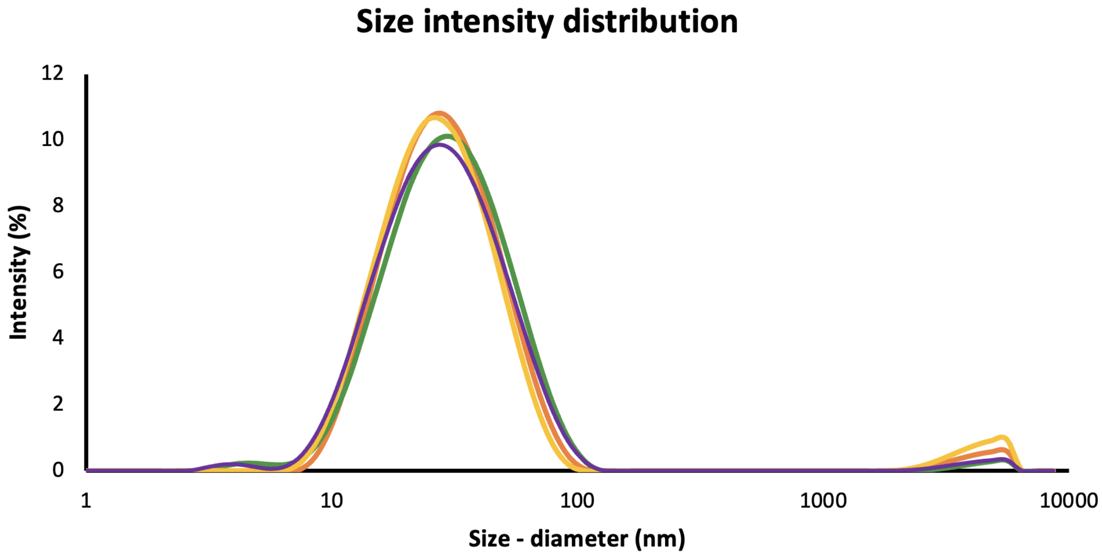

Figure 35: Size distribution of the 4 mg/ml G_{16}-b-Dex_{32} NPs prepared by dialysis.

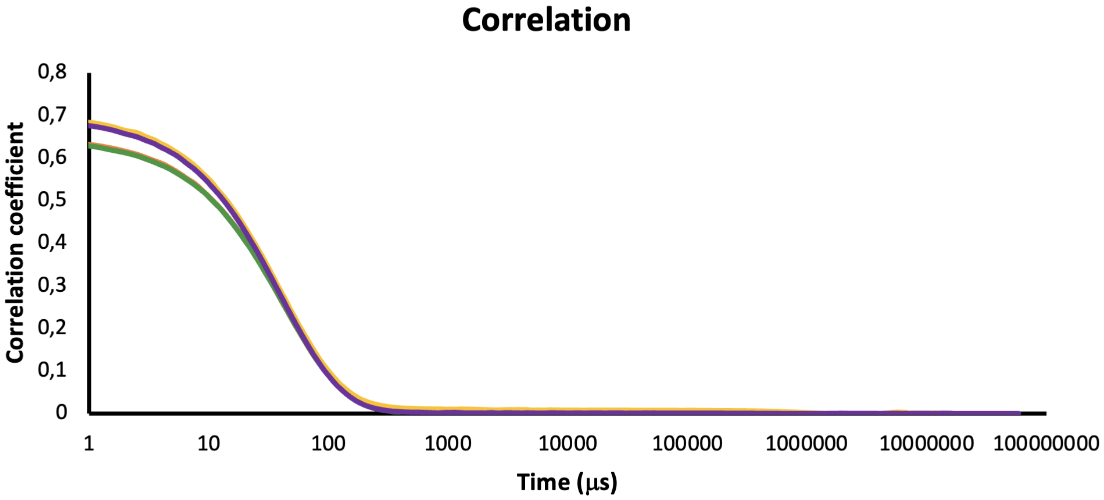

Figure 36: Correlation of the 4 mg/ml G_{16}-b-Dex_{32} NPs prepared by dialysis.

4.2 MALS results

Throughout this section, the data has been collected using the software Astra, and processed in Excel, see the Appendix Section C for the steps done in Astra and the Excel setup used in the calculations.

4.2.1 Standard samples

The standard sample Dextran-2000 with a weight average molecular weight (M_w) of 1927 kDa was used [99]. In addition, a standard sample of pullulan with an M_w of 8.2 kDa was used. The dn/dc for both dextran and pullulan was set to 0.148.

Sample	**M_w calculated (g/mol)**	**A_2 [$\mathbf{cm^3 \cdot mol/g^2}$]**
Dextran-2000	$1.61 \cdot 10^6$	$5.50 \cdot 10^{-5}$
Pullulan 8.2 kDa	$3.13 \cdot 10^4$	$1.47 \cdot 10^{-2}$

Table 6: The calculated weight average molecular weight and second virial coefficient of two standard samples obtained by MALS-analysis.

4.2.2 G_{16}-b-Dex_{32} NPs by dialysis

A concentration series containing 0.2 mg/ml, 0.5 mg/ml and 1.0 mg/ml was prepared. The dn/dc was set to 0.150.

Sample	**M_w calculated (g/mol)**	**A_2 [$\mathbf{cm^3 \cdot mol/g^2}$]**
G_{16}-b-Dex_{32}	$1.26 \cdot 10^5$	$-9.70 \cdot 10^{-4}$

Table 7: The calculated weight average molecular weight and second virial coefficient of G_{16}-b-Dex_{32} NPs obtained by MALS-analysis.

4.2.3 G_{16}-b-Dex_{32} and G_{16}-b-Dex_{43} NPs by direct titration

This section describes the subsequent MALS-analysis of the NPs from Sections 4.1.2 and 4.1.3. Samples with 0 %, 80 %, and 120 % saturation were prepared. Concentration series of 0.2 mg/ml, 0.5 mg/ml, 1.0 mg/ml and 2.0 mg/ml were subsequently prepared for each sample and % saturation. The dn/dc was set to 0.150. Due to insufficient signals for the 0 % samples, and 0.2 mg/ml samples in all cases, these were not included in the data analysis.

Sample	**M_w calculated (g/mol)**	**A_2 [$\mathbf{cm^3 \cdot mol/g^2}$]**
G_{16}-b-Dex_{32} 80 %	$2.40 \cdot 10^4$	$-3.13 \cdot 10^{-3}$
G_{16}-b-Dex_{32} 120 %	$7.00 \cdot 10^4$	$-1.14 \cdot 10^{-3}$
G_{16}-b-Dex_{43} 80 %	$4.38 \cdot 10^4$	$-8.05 \cdot 10^{-4}$
G_{16}-b-Dex_{43} 120 %	$8.78 \cdot 10^4$	$-6.80 \cdot 10^{-4}$

Table 8: The calculated weight average molecular weight and second virial coefficient of different NPs prepared by direct titration, obtained by MALS-analysis.

4.2.4 G_{16}-b-Dex_{43}, G_{37}-b-Dex_{43}, and G_{16}-b-Dex_{32} NPs by dialysis

This section describes the subsequent MALS-analysis of the NPs from Section 4.1.5. Table 9 displays the calculated weight average molecular weight M_w and second virial coefficient A_2 of different NPs obtained by MALS analysis [6]. The dn/dc was set to 0.150.

---

[6] Due to somewhat inaccurate concentrations, these results are only approximate.

Sample	M_w calculated (g/mol)	A_2 [$cm^3 \cdot mol/g^2$]
G_{16}-b-Dex_{43}	$5.35 \cdot 10^4$	$-2.02 \cdot 10^{-3}$
G_{37}-b-Dex_{43}	$8.62 \cdot 10^5$	$-7.5 \cdot 10^{-5}$
G_{16}-b-Dex_{32}	$7.35 \cdot 10^4$	$-1.24 \cdot 10^{-3}$

Table 9: The calculated weight average molecular weight and second virial coefficient of different NPs obtained by MALS-analysis.

4.3 AFM results

All images are shown in the height sensor (Z-sensor) mode. Brighter color means that the area is elevated, whereas darker color indicate lower areas.

4.3.1 G_{16}-b-Dex_{32} NPs by dialysis

The images in Figure 37 were obtained during the work on this Master's Thesis. Table 10 summarizes the findings from the images included in Figure 37.

Image	Sample	Treatment	Particle size (nm)
A	G_{16}-b-Dex_{32} 0.2 mg/ml	not vacuum dried	18-60
B	G_{16}-b-Dex_{32} 1 mg/ml	vacuum dried	20-40
C	G_{16}-b-Dex_{32} 0.2 mg/ml	vacuum dried	15-25

Table 10: The measured particle size for G_{16}-b-Dex_{32} NPs prepared by dialysis with different treatments and concentrations.

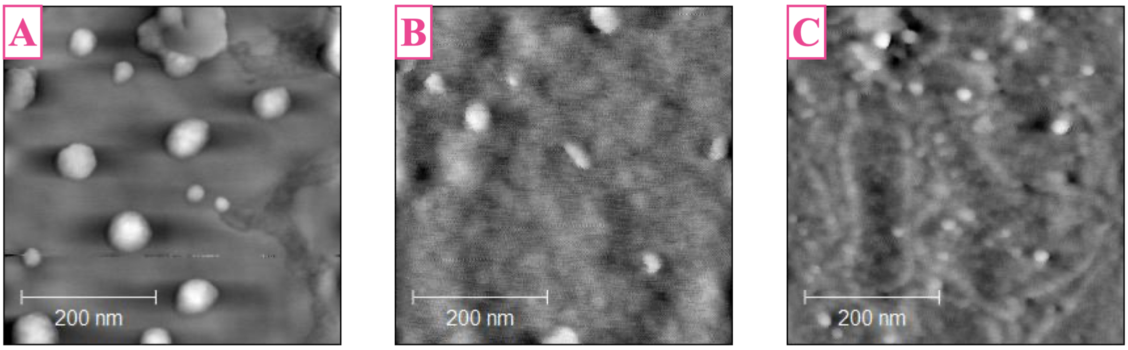

Figure 37: G_{16}-b-Dex_{32} NPs prepared by dialysis. Image A is 0.2 mg/ml, not vacuum dried. Image B is 1 mg/ml, vacuum dried. Image C is 0.2 mg/ml, vacuum dried.

Figures 38 and 39 are adapted from the author's Project Thesis [13]. Figure 38 shows a particle size of 30-75 nm. Figure 39 shows agglomerated particles.

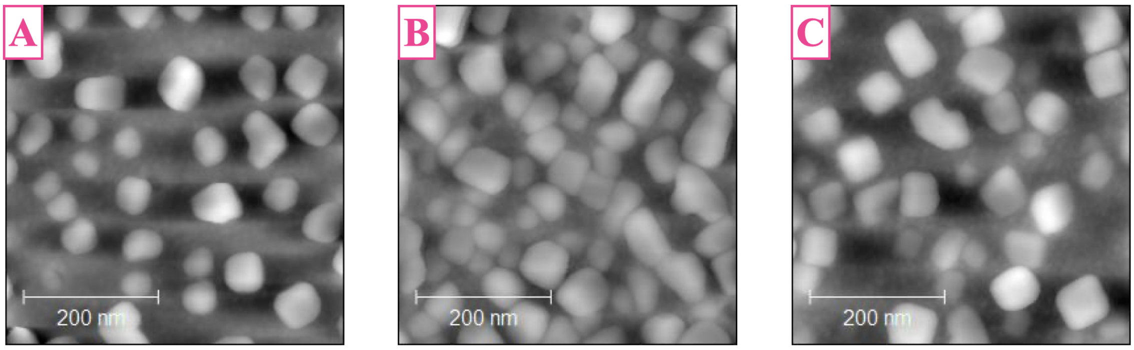

Figure 38: The images show G_{16}-b-Dex_{32} NPs 1 mg/ml prepared by dialysis.

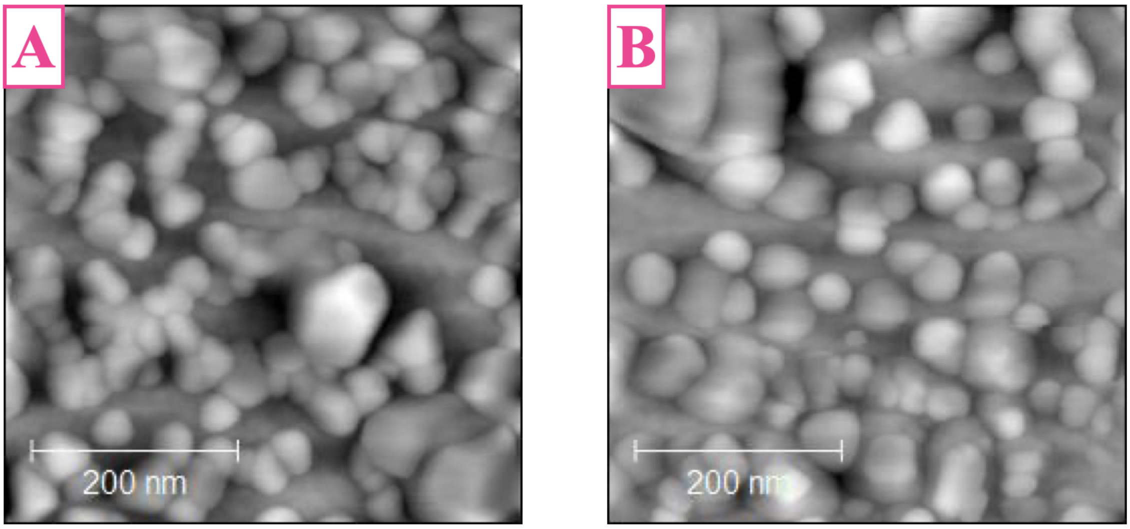

Figure 39: The images show G_{16}-b-Dex_{32} NPs 0.2 mg/ml prepared by dialysis.

4.3.2 G_{19}-b-Dex_{45} NPs by dialysis

Figure 40 is adapted from the author's Project Thesis [13]. Table 11 displays the particle size measured for the particles in the figure.

Image	Sample	Particle size (nm)
A	G_{19}-b-Dex_{45} 1 mg/ml	55-125
B	G_{19}-b-Dex_{45} 0.2 mg/ml	70-125

Table 11: The measured particle size for G_{19}-b-Dex_{45} NPs prepared by dialysis.

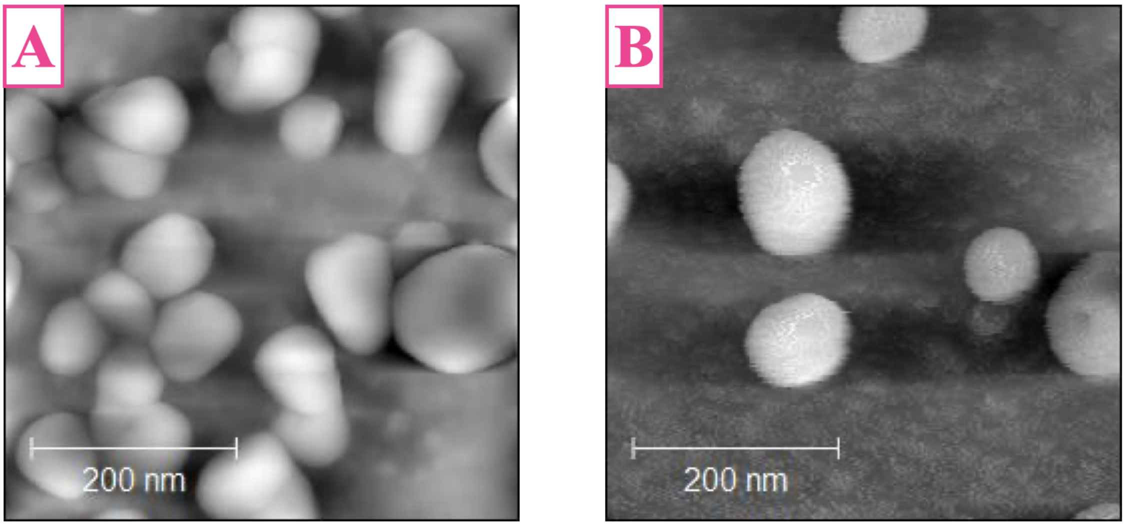

Figure 40: G_{19}-b-Dex_{45} NPs prepared by dialysis. Image A is 1 mg/ml, while Image B is 0.2 mg/ml.

4.3.3 Negative control

Figure 41 shows a negative control with pure mica.

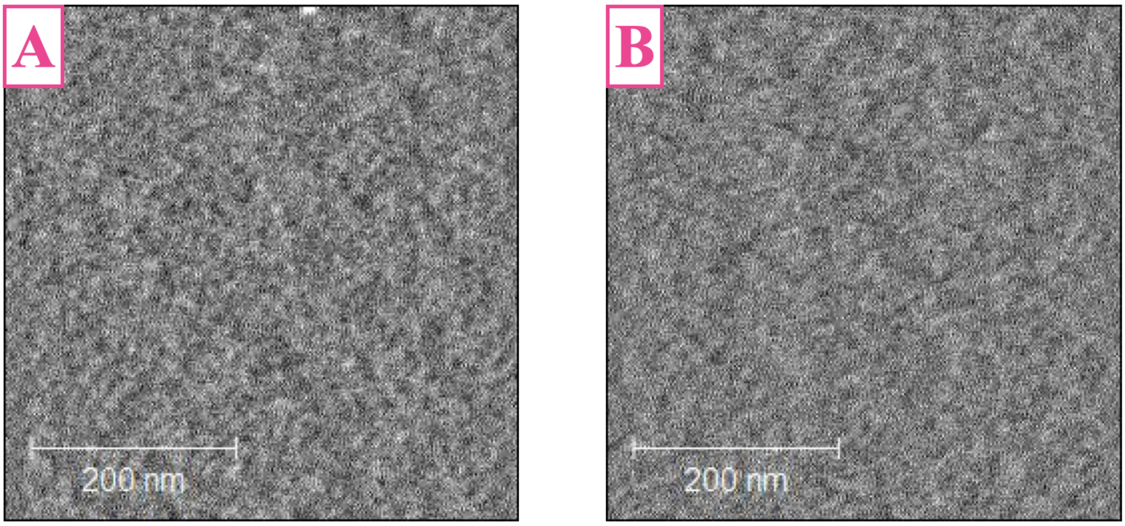

Figure 41: Pure mica for the negative control.

4.4 SEM results

Each SEM image displays relevant imaging parameters in the footer. Full size images are provided in the Appendix Section E. All images were taken using the T2 detector in immersion mode. Table 12 clarifies the abbreviations used in the image footers.

Abbreviation	**Meaning**
HFW	Horizontal field width
curr	Beam current
HV	Acceleration voltage (high voltage)
tilt	Degree of tilting of sample stage
det	Detector
mode	Operational mode of detector
mag	Magnification
WD	Working distance

Table 12: Clarification of abbreviations used in SEM images.

4.4.1 G_{16}-b-Dex_{32} NPs by dialysis

G_{16}-b-Dex_{32} NPs prepared by dialysis were investigated using SEM. One sample had undergone the extra process step of vacuum drying, see Figures 42, 43, and 44, while the other sample was not vacuum dried, see Figures 45 and 46.

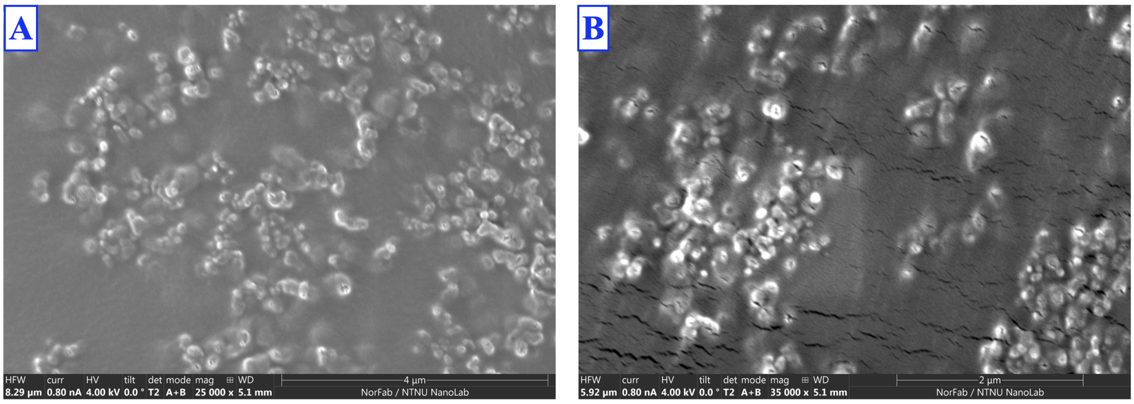

Figure 42: G_{16}-b-Dex_{32} NPs prepared by dialysis. This sample was vacuum dried.

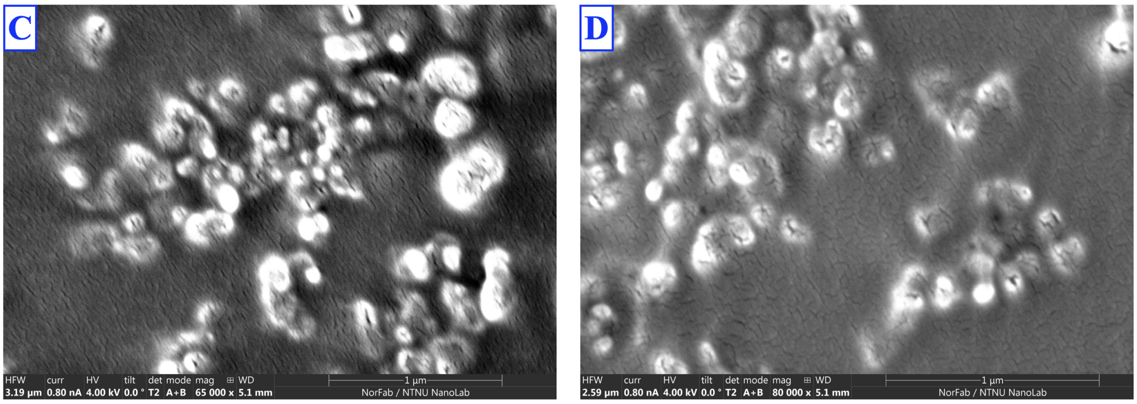

Figure 43: G_{16}-b-Dex_{32} NPs prepared by dialysis. This sample was vacuum dried.

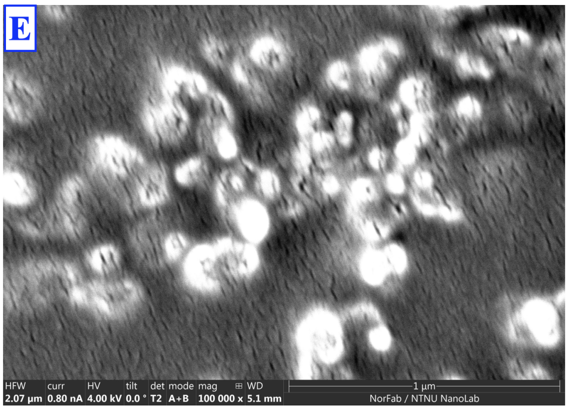

Figure 44: G_{16}-b-Dex_{32} NPs prepared by dialysis. This sample was vacuum dried.

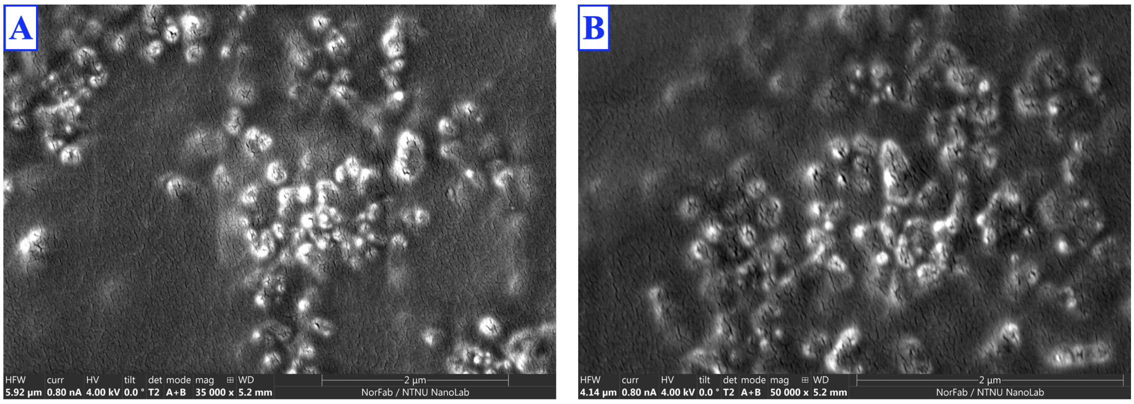

Figure 45: G_{16}-b-Dex_{32} NPs prepared by dialysis. This sample was not vacuum dried.

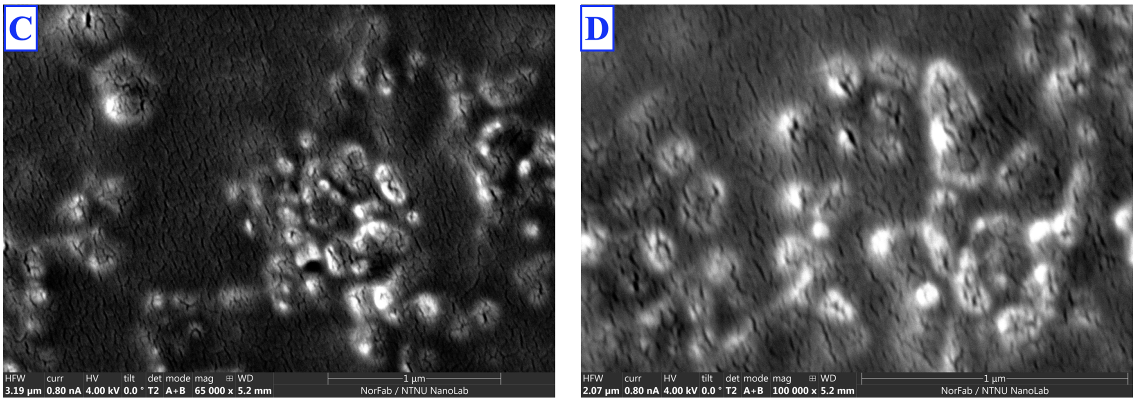

Figure 46: G_{16}-b-Dex_{32} NPs prepared by dialysis. This sample was not vacuum dried.

4.4.2 Negative control

Figures 47 and 48 show pure carbon tape used for the negative control. The carbon tape was not coated.

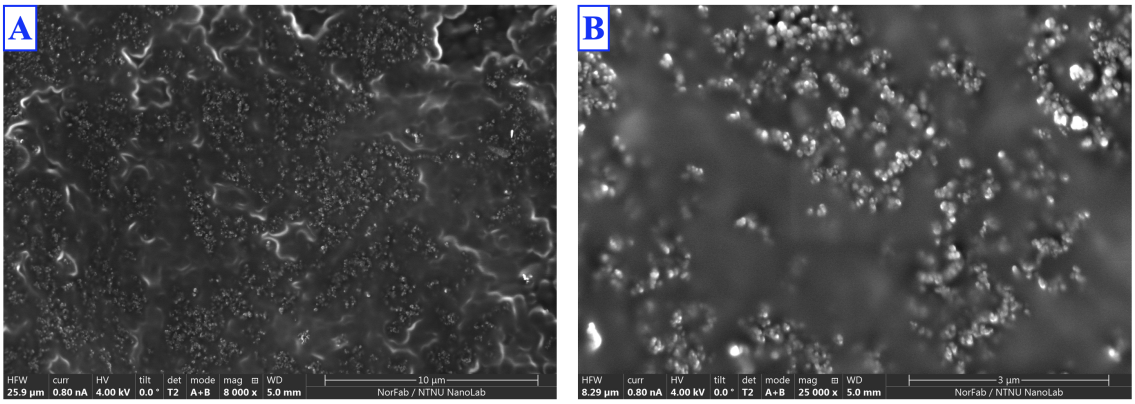

Figure 47: Pure carbon tape for the negative control.

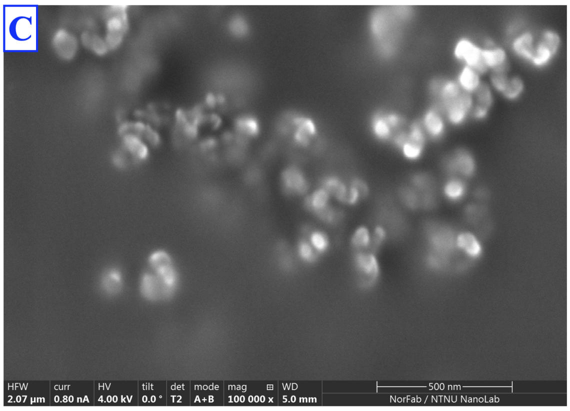

Figure 48: Pure carbon tape for the negative control.

Figures 49 and 50 show a sample of 20 mM $CaCl_2$ and 10 mM NaCl, the buffer solution used to dialyse the NPs. The sample was coated.

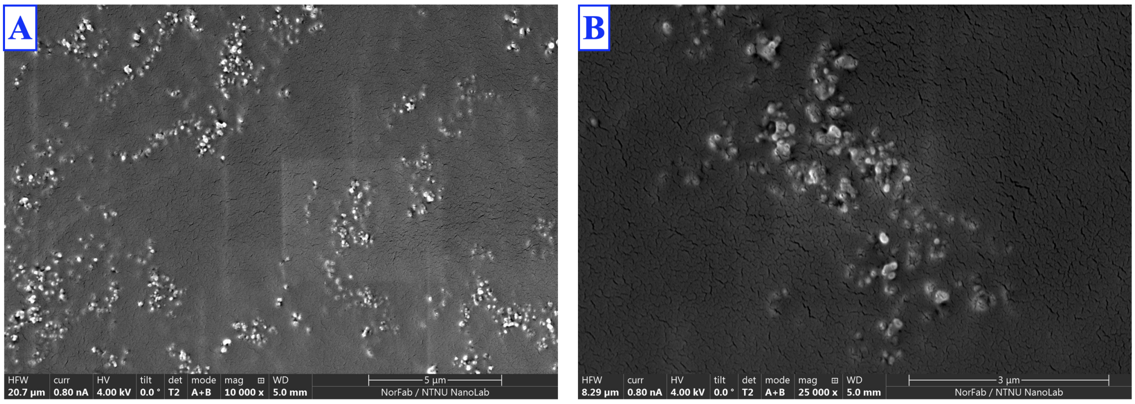

Figure 49: 20 mM $CaCl_2$ and 10 mM NaCl for the negative control.

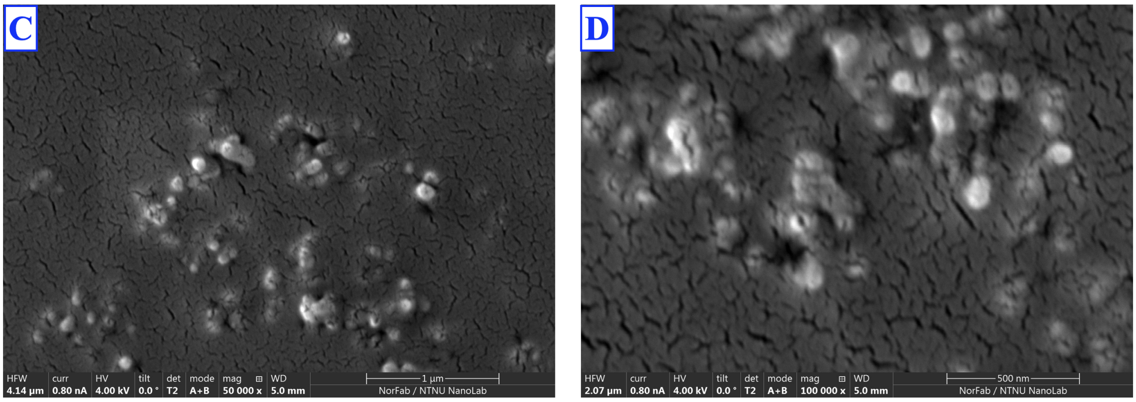

Figure 50: 20 mM $CaCl_2$ and 10 mM NaCl for the negative control.

5 Discussion

5.1 Size of NPs

The NPs are prepared as a solution, and thus the most accurate way of measuring their size should be with a characterization technique which allows for the sample to be analyzed in its native form. In this study, that technique is DLS. As highlighted in Table 1, DLS is a quick and simple technique to obtain the size distribution of NPs, however, its main drawback is low resolution. It is not single NPs that are being measured with DLS, but rather the time dependence of the intensity. AFM on the other hand has extremely high resolution down to single NPs, though it requires the NPs to be dried in sample preparation and is much more time-consuming. While the size of NPs imaged by AFM can be directly measured using appropriate software, this may not reflect the true size of the NPs in solution. Moreover, the size of a few NPs imaged by AFM cannot serve as a statistical average for the whole sample of NPs, just as the average size of the whole sample recorded by DLS does not provide any information about individual NPs. This is the reason why combining DLS and AFM to investigate the size of NPs is beneficial. Neither characterization method can provide the full scope on its own, but together quite a comprehensive image can be built. In addition, performing DLS on an NP sample before characterizing with more intricate methods is a good assessment to check if the NPs have formed as desired. Table 13 compares size recorded by DLS and AFM through this work.

Characterization	**NP sample**	**Preparation**	**Size (nm)**
DLS	G_{16}-b-Dex_{32}	Dialysis	25
DLS	G_{16}-b-Dex_{32}	Direct titration 0 %	46
DLS	G_{16}-b-Dex_{32}	Direct titration 80 %	18
DLS	G_{16}-b-Dex_{32}	Direct titration 120 %	24
DLS	G_{16}-b-Dex_{43}	Direct titration 80 %	17
DLS	G_{16}-b-Dex_{43}	Direct titration 120 %	17
DLS	G_{16}-b-Dex_{32}	Dialysis (before MQ)	28
DLS	G_{16}-b-Dex_{32}	Dialysis (after MQ)	72
DLS	G_{16}-b-Dex_{43}	Dialysis	29
DLS	G_{37}-b-Dex_{43}	Dialysis	38
DLS	G_{16}-b-Dex_{32}	Dialysis	25
AFM	G_{16}-b-Dex_{32}	Dialysis	18-60
AFM	G_{16}-b-Dex_{32}	Dialysis + vacuum dried	15-40
AFM	G_{16}-b-Dex_{32}	Dialysis	30-75
AFM	G_{19}-b-Dex_{45}	Dialysis	55-125

Table 13: The average size of the NP samples presented in Sections 4.1 and 4.3.

In general, AFM appears to record a larger particle size than DLS for the same type of NP. This observation was somewhat reduced by introducing vacuum drying as a sample preparation step for AFM. The size chart shows that the length of the G-block chain has a more substantial effect of the overall particle size than the length of the dextran chain. This can be traced back to the fact that G-block binds the divalent cations and assembles the core of the particle, while dextran forms a stabilizing corona around it.

The size of NPs is crucial for medical and pharmaceutical purposes [100]. For cancer therapeutics specifically, the NPs need to be able to move through small capillaries and into tumors. However, the NPs should not be too small. Studies on spherically shaped NPs have shown that particles under 5 nm are promptly cleared from circulation [101]. The mechanisms responsible for this are extravasation and renal clearance. Extravasation is the leakage of fluid from a blood vessel to the surrounding tissue [102], while renal clearance refers to the kidneys' removal of substances from plasma [103]. On the other hand, NPs that are too large may end up accumulated in the liver, spleen, and bone marrow [101]. The exact size that is considered too large depends heavily on the intended outcome, e.g., which cell type is targeted, but generally speaking the lower micrometer range is not ideal for medical purposes. There is also a difference between NPs intended for long-term circulation and cellular uptake. NPs measuring 100-200 nm have been reported as the ideal candidates for long-term circulation, as they are able to evade both filtration in the spleen and uptake into the liver [101]. In terms of cellular uptake, a size of 50 nm has been reported to be ideal for efficient uptake [104].

While more research is needed to determine which cellular uptake mechanisms are ideal for the NPs in this study, the size analysis place them in an intriguing territory for medical and pharmaceutical research. As the long-term goal is to have the NPs deliver radioactive isotopes to cancerous cells, their size needs to be ideal for cellular uptake and not for long-term circulation.

5.1.1 DLS size intensity distribution, correlation and derived count rate

From the DLS analysis of G_{16}-b-Dex_{32} and G_{16}-b-Dex_{43} NPs prepared by direct titration, as shown in Sections 4.1.2 and 4.1.3, the size distribution is narrower for 120 % than for 80 % saturation of Ca/Ba stock. This can be explained by the fact that at 80 % saturation, not all diblocks have assembled to NPs. The presence of aggregates was negligible both for 120 % and for 80 % saturation. Figure 17 shows how the size distribution for G_{16}-b-Dex_{32} on diblock form looks like, i.e., 0 % saturation of Ca/Ba stock. As this figure does not provide any useful information regarding the size of NPs, a 0 % saturation sample was not made for G_{16}-b-Dex_{43}. The figure can be considered a negative control for the DLS characterization, as it clarifies the difference between the size intensity distribution of diblocks and NPs.

Section 4.1.4 describes an experiment where G_{16}-b-Dex_{32} NPs were subject to subsequent dialysis with MQ. This appears to have had a profound effect on the size and size intensity distribution of the NPs. Before MQ dialysis, the NPs had an average size of 28 nm, which corresponds well with other findings for G_{16}-b-Dex_{32}. Further, the size intensity distribution recorded for the 5 measurements of the NPs before the MQ dialysis coincide well. However, after 48 hours of MQ dialysis, the average size had nearly tripled, to 72 nm. The NPs being subject to a certain degree of swelling was expected, nonetheless, Figures 27 and 29 show that the size intensity distribution had shifted significantly. A notable amount of aggregates appear to be present in the sample after MQ dialysis, and the size distribution overall had little overlap between the different measurements. The drop in correlation from around 0.4 before and 0.08 after MQ dialysis, see Figures 28 and 30, indicate that the data quality was reduced after the MQ dialysis, and more noise was present in the correlation data. This ultimately leads to the verdict that the average size of 72 nm after MQ dialysis is approximate at best, and that MQ dialysis was not a useful sample preparation step for DLS characterization. The intention behind this experiment was to investigate if MQ dialysis was useful in terms of removing excess salt from the NPs, which, as will be further discussed in Section 5.5, has been an obstacle when investigating the NP samples with AFM and SEM.

As reviewed in Section 2.9, the correlation coefficient is a measure for data quality and noise levels. A high correlation coefficient is associated with greater data quality and low noise levels. Table 14 provides an overview of the average correlation coefficient for different NPs presented in Section 4.1. The lowest correlation coefficients of less than 0.10 are noted for G_{16}-b-Dex_{32} on diblock form (0 % saturation) and G_{16}-b-Dex_{32} NPs after dialysis against MQ. For the NPs prepared by direct titration, there is no clear link between saturation % and correlation coefficient, but it is over 0.10 for all samples. For NPs prepared by dialysis, the correlation coefficient is 0.62 on average.

NP sample	Preparation	Correlation coefficient
G_{16}-b-Dex_{32}	Dialysis	0.60
G_{16}-b-Dex_{32}	Direct titration 0 %	0.04
G_{16}-b-Dex_{32}	Direct titration 80 %	0.10
G_{16}-b-Dex_{32}	Direct titration 120 %	0.35
G_{16}-b-Dex_{43}	Direct titration 80 %	0.60
G_{16}-b-Dex_{43}	Direct titration 120 %	0.45
G_{16}-b-Dex_{32}	Dialysis (before MQ)	0.45
G_{16}-b-Dex_{32}	Dialysis (after MQ)	0.09
G_{16}-b-Dex_{43}	Dialysis	0.60
G_{37}-b-Dex_{43}	Dialysis	0.80
G_{16}-b-Dex_{32}	Dialysis	0.65

Table 14: The average correlation coefficients of the NP samples presented in Section 4.1.

A near-exponential decay of the autocorrelation function corresponds to small particles. The general trend for all NP samples, except for G_{16}-b-Dex_{32} on diblock form and G_{16}-b-Dex_{32} after dialysis against MQ, is that the autocorrelation function shows approximately exponential decay, and reaches zero between 100 and 1000 μs. This trend further strengthens the claim that the NPs are small in size.

The derived count rate (DCR) is a measure of signal strength, and high DCR values are typically correlated to larger particles. Table 15 gives an overview of the recorded DCR values in this study. The most deviating value is found for G_{37}-b-Dex_{43}, and this will be discussed further in Section 5.9. In any case, there appears to be a general trend of larger particle size leading to higher DCR. The outliers to this trend are G_{16}-b-Dex_{32} on diblock form (0 % saturation) and G_{16}-b-Dex_{32} with 80 % saturation. The former is not expected to show the same results as the actual NPs, and the latter was recorded with a relatively high DCR despite its small size of 18 nm, without any clear cause.

NP sample	Preparation	Size (nm)	Derived count rate (kcps)
G_{16}-b-Dex_{43}	Direct titration 80 %	17	530
G_{16}-b-Dex_{43}	Direct titration 120 %	17	1000
G_{16}-b-Dex_{32}	Direct titration 0 %	46	1419
G_{16}-b-Dex_{32}	Dialysis	25	1813
G_{16}-b-Dex_{32}	Dialysis	25	2448
G_{16}-b-Dex_{32}	Direct titration 120 %	24	2791
G_{16}-b-Dex_{32}	Dialysis (before MQ)	28	2809
G_{16}-b-Dex_{43}	Dialysis	29	3050
G_{16}-b-Dex_{32}	Direct titration 80 %	18	3123
G_{16}-b-Dex_{32}	Dialysis (after MQ)	72	3560
G_{37}-b-Dex_{43}	Dialysis	38	10985

Table 15: The average size and DCR of the NP samples presented in Section 4.1. DCR is presented in order of increasing magnitude.

5.2 Shape of NPs

The assumption that the G_m-b-Dex_n NPs should have a spherical shape is based on the observations by A. Solberg in [14], where a spherical shape was confirmed with AFM. The spherical shape is also reasonable to assume due to the micellar structure of the NPs. Of the characterization methods used in this work, AFM was the only one that could be used to determine the shape of individual NPs. In theory, SEM should be able to achieve a similar resolution, but for reasons that will be discussed in Sections 5.8.2 and 5.8.3, this was not the case in this work. The AFM images presented in Section 4.3 show that the NPs are spherical or rounded cubic. For example, Image A in Figure 37 and Image B in Figure 40 show close to perfectly spherical NPs, while Figure 38 presents NPs with both spherical and rounded cubic shapes. One reason for why the NPs are not all perfectly spherical could be related to the sample preparation for AFM, in particular the drying step(s). However, the reason behind the occurrence of rounded cubic NPs has not been investigated in detail, and so conclusive statements cannot be given about the cause at this time.

5.3 Molar mass of NPs

The molar mass of NPs was registered to be in the range of 10^4 and 10^5 Da. Table 8 indicates that the molar mass for the same NPs increase with saturation %. This makes sense because a higher saturation % means that there are more bound divalent cations in the NPs. In addition, the fact that more diblocks have assembled to NPs with higher saturation % could also lead to a higher recorded molar mass, as there are less free diblocks present. Table 13 shows that the particle size recorded by DLS does increase with saturation % in the case of G_{16}-b-Dex_{32}, but not for G_{16}-b-Dex_{43} where the particle size is the same both for 80 % and 120 % saturation. These findings from MALS and DLS combined suggest that there is a link between saturation %, particle molar mass, and size. However, future research could clarify this link further.

The experiment presented in Table 9 was flawed because of inaccurate concentrations used, see Section 5.8.5 for an explanation as to why, therefore, the recorded molar masses are questionable. For instance, G_{16}-b-Dex_{43} is recorded with a lower molar mass than G_{16}-b-Dex_{32}, which is likely due to these concentration inaccuracies and not to the reality. The one thing that can however be deducted from these results is that G_{37}-b-Dex_{43} displays a significantly higher molar mass than G_{16}-b-Dex_{43} and G_{16}-b-Dex_{32}. This is justifiable with the fact that since G-blocks bind the divalent cations, an increase in G-block length will have a more profound effect on the NPs molar mass than an increase in dextran length. Not only will there be more G-block monomers present, which would also be the case for dextran monomers, there will in addition be more bound divalent cations which contribute to the molar mass.

A_2 for the NPs was in all cases negative, with values in the range of 10^{-3} and 10^{-5}. As introduced in Section 2.10, $A_2 < 0$ are attractive interactions materializing as a perceptible increase in molar mass. The consequence of this is that the observed molar masses are probably somewhat higher than in reality. Nonetheless, given the rather small A_2 values recorded, the increase in observed molar mass is negligible.

5.4 Aggregation and agglomeration of particles

Both DLS and AFM provide information about the particles' tendency to aggregate and agglomerate. Aggregation occurs due to strong covalent or metallic bonds forming between NPs [105]. Agglomeration is governed by weak forces and involves NPs adhering to each other, creating units in the sub-micron size range. The driving force behind aggregation and agglomeration is reducing surface free energy, and is achieved by agglomerating to a bigger size which reduces the particle's surface area.

With AFM, agglomerates can be recognized by NPs forming loosely associated structures. Examples of agglomerated NPs are seen in Figure 39. While the agglomerated particles appear to be loosely attached to each other, it is still possible to identify the individual particles and conclude that this is most likely caused by weak interactions between particles. While it is possible that some of the larger particles imaged could be aggregates, there is no clear way to prove this. Aggregation could have occurred during sample preparation, but again this would be quite intricate to demonstrate.

DLS provides some information about the presence of aggregates and agglomerates in an NP sample. Peaks to the far right of the size intensity distribution graph indicate the presence of aggregates and/or agglomerates in a sample, however, which one of the two is present cannot be read from these data. Peaks to the far right simply indicate that large particles are present, but as individual particles cannot be viewed with DLS, such large particles could just as well be aggregates as agglomerates. Reviewing the size intensity distributions presented in Section 4.1, the samples that appear to have a presence of larger particles have so in the size range between 1000-10000 nm (1-10 μm). The most extreme case can be seen in Figure 29 showing G_{16}-b-Dex_{32} NPs after dialysis against MQ. More moderate cases can be seen in Figures 19, 25, 27, 31, 33, and 35.

5.5 Effects of salt

An issue throughout this work has been the presence of Ca/Ba salts in NP samples, in particular in dried samples for AFM and SEM. Since the diblock copolymers require divalent cations to form NPs, the addition of ions is inevitable. However, it can be difficult to distinguish between salt crystals and NPs in the dried samples. The shape of the particles can in most cases specify if a NP or a salt crystal can be seen. The NPs generally display a spherical and uniform shape, whereas the shape of salt crystals appear more irregular and heterogenous.

5.5.1 Subsequent dialysis against MQ

The experiment which results are presented in Section 4.1.4 showed that the presence of salt due to dialysis against $CaCl_2$ and NaCl is not problematic for DLS measurements, rather, the removal of salt through subsequent dialysis against MQ is unfavorable, as discussed in Section 5.1.1. The stable size intensity and correlation measurements before the MQ dialysis deteriorated significantly after the MQ dialysis.

5.5.2 Distinguishing salt from NPs

Throughout this work, distinguishing salt crystals from NPs when working with AFM and SEM has been a challenge. The main approach to solving this question has been investigating the shape and size of particles. Particles that were spherical to rounded cubic were assumed to be NPs, whereas particles with an irregular shape were assumed to be salt crystals. A size in the area of 20-100 nm combined with a spherical shape further strengthened the assumption that what was seen was indeed a NP.

5.6 Effects of vacuum drying

Vacuum drying was introduced as an additional sample preparation step for AFM and SEM in this work. The background for this decision was that the NPs imaged by AFM tended to be larger than the same NPs analyzed with DLS. This is in principle a curious observation since one could assume that NPs in solution would have a certain degree of swelling and thus be larger than dried NPs, regardless of the degree of dryness. An open question thus remains whether or not the NPs swell or aggregate during the drying process. It is not necessarily possible to identify an aggregated particle with AFM, as the strong bonds created between NPs can make them appear as one entity. However, due to the sizes seen with AFM at times being twice as large as the sizes seen with DLS, particles aggregating in the AFM sample preparation is a possible cause.

G_{16}-b-Dex_{32} NPs have been extensively researched both with DLS and AFM in this study. These NPs had an average size of 24 nm across DLS measurements. AFM analysis showed that the NPs that were not vacuum dried had a size between 18-75 nm, while the vacuum dried NPs measured 15-40 nm. These results suggest that vacuum drying had an effect on the size of NPs prepared for AFM, by producing an NP size closer to the one seen by DLS in its native form in solution. These observations could be interesting to explore in future research, e.g., by investigating the optimal parameters for the vacuum drying process. Relevant variable parameters in this case include temperature, pressure, hysteresis, and drying time.

Vacuum drying was also tested on SEM-samples, however, given the inconclusive images, discussed in Sections 5.8.2 and 5.8.3, it is not possible to draw a conclusion as to how useful vacuum drying was for the SEM analysis.

5.7 Direct titration for NP self-assembly

An alternative approach to dialysis for NP self-assembly has been investigated in this work. This approach is the direct titration of buffer solution to a solution of diblocks. The main advantage presented by this approach is that it is less time-consuming than dialysis. While dialysis in this case is done overnight, titration can be done in an hour. An aspect of the titration approach that could be explored further in future research is the significance of the time span for a titration, e.g., the difference between a 1-hour titration and an overnight one.

In Section 4.1.2, the DLS results of an experiment concerning G_{16}-b-Dex_{32} NPs by direct titration are shown. At 0% saturation of Ca/Ba stock, the solution is a diblock and NPs have not formed because no Ca^{2+} or Ba^{2+} ions are present. This is seen in the turbulent size intensity distribution in Figure 17, and the poor correlation in Figure 18. Figures 19 and 21 show how the size distribution narrows to the area of 10-100 nm when Ca^{2+} and Ba^{2+} ions are present. These figures show that the measurements overlap quite well for 80% saturation, and with 120% saturation the overlap is nearly perfect. A minuscule amount of aggregates are present in the sample with 80% saturation, whereas the graph for 120% saturation is perfectly flat after 100 nm, i.e., no aggregates appear to be present. The distinction between 80% and 120% saturation can also be seen in Figures 20 and 22 showing the correlation. For 80% saturation, the correlation coefficient is around 0.10, falls quickly enough, but does not fully approach zero for all measurements. For 120% saturation, the coefficient is over 0.30, it falls quickly and all measurements fall to zero after about 1000 μs. These findings indicate that a 120 % saturation leads to a more uniform size distribution and better data quality than an 80 % saturation. Similar results is seen for G_{16}-b-Dex_{43} in Section 4.1.3. 120 % saturation shows a more uniform size distribution than 80 %, and only a minuscule amount of aggregates are present for the 120 % saturation. Both percentages have a high correlation coefficient and an approximately exponentially falling autocorrelation function, indicating sterling data quality.

Several attempts were made at obtaining AFM images of the samples containing NPs prepared by direct titration. However, no good images were procured. Because the DLS and MALS results of NPs by direct titration strongly suggests that NPs have indeed formed, the lack of AFM results on these NPs are likely due to not succeeding in locating an interesting area of the sample. Obtaining AFM images of NPs prepared by direct titration is an area future research could look into.

5.8 Characterization methods

5.8.1 Characterization with AFM

The main application areas for AFM as a characterization technique for G_m-b-Dex_n NPs are size and shape determination. In addition, the technique can provide information on particle behaviour such as agglomeration. It is distinctive in its ability to image individual NPs with great resolution.

Two main elements that separates AFM from SEM is that samples do not need to be conductive, and the instrument does not operate in vacuum. This means that samples such as biological specimens and insulators can be analyzed without first coating them in a metallic or carbon coating. In addition, many biological specimens cannot be subject to vacuum without compromising their native state.

Two main drawbacks of AFM are that it is time-consuming and typically requires dry samples.

However, there are ways to circumvent the latter. An example is by using a technique known as fluidic force microscopy (FluidFM) [106], developed by a research team at ETH Zürich [107]. The technique combines ordinary AFM with microchanneled cantilevers designed for local fluid distribution by means of a fluidic circuit. The technique has found many applications particularly in biology, where single cells, bacteria etc. can be studied under physiological conditions. Whether FluidFM is relevant for inanimate NPs can be discussed, as DLS already poses as a quick and easy method of obtaining an average size of NPs in their native state.

5.8.2 Characterization with SEM

According to the SEM Apreo user manual, the T2 detector in "mode A+B" (composite mode) does display atomic number contrast to some degree despite the detector being primarily designed to collect secondary electrons. Therefore, discussing the figures in Section 4.4 with focus on atomic number contrast is a relevant discussion.

Carbon is a light non-metal element with atomic number 6 (Z=6). Therefore, carbon tape will appear darker when seen in combination with heavier elements. It is difficult to determine which SEM-images in this study actually show NPs, as even the negative control with pure carbon tape displayed particle-like structures that appear bright. As can be seen in Figures 3 and 5, alginate and dextran are polysaccharides containing carbon, oxygen, and hydrogen. These elements have atomic number 6, 8, and 1, respectively. These atoms alone would not account for any significant contrast in BSE signals to the carbon tape. This could explain why the NPs do not show up, or show up very insignificantly, in the SEM-images. Calcium (Z=20) and barium (Z=56) have better chances of showing up as contrast because they are heavier elements than carbon, oxygen, and hydrogen. In this study, direct titration experiments for SEM were not done, but this could be an interesting point in future research. Since the Ca/Ba stock solution contains barium, this heavier alkali metal may provide the NPs with better contrast in SEM imaging.

However, it should be noted that atomic number contrast does not provide much useful information about the NPs. The NPs have a known molecular structure, and are checked for various atomic signals using NMR in the preparation process. Thus, if anything about the molecular structure was out of the ordinary, this would have been uncovered during the diblock preparation process. The main piece of information that can be deducted from the atomic number contrast is that carbon tape is not a suitable substrate for the NPs.

Even though SE signals can show the NPs topographically, given that there is good enough resolution, if there is contamination or roughness of the carbon tape as well, it can be quite intricate to distinguish the NPs from the rest. The mica substrate used for AFM was exceptionally flat and polished, see Figure 41. The same cannot be said for the carbon tape, see Figures 47 and 48, which questions its suitability for SEM imaging of the NPs. Both optical inspection and SEM-images of the carbon tape show a rough surface, and this is likely a cause for the inconclusive images.

5.8.3 Characterization with SEM versus AFM

Characterizing the particles using SEM was a new experimental approach used in this work. In previous work [13, 14], only AFM had been used for this purpose.

The main advantage SEM has over AFM in this case, is that it easier to gain an overview of the sample and choose areas to study more closely from there. With AFM, a camera can show where on the sample the cantilever scans, but the magnification provided by such a camera is not enough to see where the NPs on the sample are. An improvised solution used was marking the mica discs with a sharpie around where the solution has been dried onto the disc. As can be seen in the SEM-images provided in Section 4.4, there are gaps of void between the clusters of particles [7]. With SEM, this is easy to navigate using a lower magnification to locate an interesting area, and steer clear of the void. With AFM, a scan must be started and run for a few minutes

---

[7] It could not be determined whether these particles were in fact the NPs of interest or native to the carbon tape and/or buffer solution. Nevertheless, clusters of some sort can be seen in the SEM images.

before one can tell if the scan area is of interest. This means that AFM is a more time-consuming characterization method than SEM.

Nevertheless, it proved difficult to get good resolution at the nanometer scale with SEM for this particular sample. The best resolution achieved was obtained using the T2 detector in immersion mode, an acceleration voltage of 4.00 kV, a beam current of 0.80 nA, and a working distance of around 5.1 mm. For future research, the optimal parameter settings for SEM can be explored further. Another aspect that can be researched further is the substrate used to deposit the sample on. The choice to use carbon tape was based on the method described in [108]. This article describes a process in which cells were grown on carbon tape and coated with gold. However, after conducting the negative control using only carbon tape, it became clear that this substrate was not optimal for the NPs in this work. As mentioned, a similar magnification as the one used in AFM (500 x 500 nm) was unattainable with SEM. The SEM-images with 100.000 x magnification are still not close to the resolution that is easily obtained with AFM. With special emphasis on ease of operation as well as image quality on the nanometer scale, AFM performed the best in both categories.

With AFM, achieving good resolution at the nanometer scale was quite convenient. Using a scan area of 500 x 500 nm, individual NPs can be seen clearly. The use of an AFM instrument that chooses and monitors different scan parameters for the user, see Section 2.7.2, further simplifies the characterization. Apart from locating an interesting area of the sample, there is not anything further that must be done before the scan can start. This is in contrast to SEM, where focus, stigma, contrast, brightness etc. have to be adjusted frequently when the magnification is changed.

Ultimately, AFM appears to be the most valuable in the characterization of the NPs. The main advantage AFM has over SEM is that good resolution on the nanometer scale is easier to achieve. The main benefit of using SEM over AFM is that it is easier to locate an interesting area of the sample.

5.8.4 Characterization with DLS

DLS has been demonstrated to be a convenient and important characterization step in the work with G_m-b-Dex_n NPs. The key information that can be collected from DLS is the size of NPs. In addition, the size intensity distribution and correlation graphs provide information about how narrow the size distribution is, the presence of aggregates, and how reliable the average size is. The experimental process for DLS described in Section 3.3.1 is quick and relatively simple to carry out. Another key advantage of DLS is that there is no loss of sample. The sample placed in the cuvette for DLS analysis can be pipetted back to the rest of the sample afterwards. Besides, only 100 μl sample is required to a do DLS analysis, and liquid samples can be analyzed in their native form.

5.8.5 Characterization with MALS

This work has shown that MALS is a promising characterization method for the NPs. The principle of this characterization method was shown by dextran and pullulan standard samples, see Section 4.2.1. The purpose of using such standards was to investigate how well the characterization method worked to determine the experimentally calculated M_w of a sample with a known M_w. Further, the use of a standard sample with a somewhat similar M_w to what could be expected of the NPs, in this case pullulan with an M_w of 8.2 kDa, helps to establish which concentrations give an adequate signal for a particle of that size. Since the diblock material at hand was very limited (under 100 mg for all), it was rational to first test out the experiment using a standard biopolymer sample which can be bought commercially.

The measured M_w for Dextran-2000 was around 20 % lower than the expected M_w, i.e., the M_w that the product claimed to have. For pullulan, the measured M_w was alomst 3 times higher than the product claim. Although M_w for such products is only stated as a nominal value, these divergences are too large to be justified with this argument. The small positive A_2-value of

$5.50 \cdot 10^{-5}$ for dextran does in theory indicate a lower recorded molar mass than in reality, however the deviation from the product claim is far too large to be explained by this. Furthermore, pullulan had a positive A_2-value of $1.47 \cdot 10^{-2}$, but was recorded with a significantly higher molar mass than the product claim. According to theory, A_2 should in this case have been negative, which it is not. Hence, A_2 can not have been the culprit for the deviating molar mass measurements. There are other causes such as software user error and slightly incorrect concentrations, that are more likely culprits in this case. As the characterization method was very new to the project, human error is the most feasible explanation. Nonetheless, the MALS analysis done on the standard samples demonstrated the use of MALS to determine M_w of biopolymers.

Preparing a concentration series from a solution is more demanding than the preparation from a solid state. Although the starting material in this case is also solid, i.e., the dried diblocks, the dialysis step needed to assemble the NPs leads to some loss of volume and thus a different concentration after dialysis than the intended start concentration. This was not taken into account while performing the MALS-experiments done in this work, and thus the data cannot be used to accurately calculate the molecular weight of the NPs. This is not a concern with characterization by AFM, SEM, and DLS, but it is a concern with MALS because the concentrations used have to be accurate for the collected data to be useful. For AFM and SEM, the concentration of the solution that is dried onto the mica disc or SEM-stub has no other function than to serve as guidance of how many NPs are present in the resulting images. For DLS, while it is important that the concentration is not exceedingly high or low, as explained in Section 2.9, the exact concentration used is not crucial. Preparing the NPs for MALS-characterization with direct titration is one measure to make the concentration series preparation easier and the data more accurate. Through direct titration, the final volume and concentration of the resulting NP solution is known because no volume is lost in dialysis.

The MALS-experiments showed that concentrations from 0.5 mg/ml and up give satisfactory signals for the NPs. With a lower flow rate on the syringe pump, e.g., 0.2 ml/min, a sample size of 1 ml was enough to get a stable signal that could be used for further data analysis. A full concentration series can be prepared before the experiment, or the first injected sample can be recycled and diluted to the next concentration. The drawback of the former is that a significant amount (several mg) of diblock is needed. Because the preparation of the diblocks is time-consuming and work-intensive, it is preferable to use as little diblock as possible when conducting the characterization. A disadvantage of the latter is that it can be challenging to constantly prepare new concentrations as the experiment is running. This is especially due to the experience made in this work that there is some loss of solution occurring during the experiment. This results in the inability to calculate the amount of buffer to add to the new concentrations in advance. This effect was not expected as the experiment described in Section 4.2.4 was conducted, and a visual estimate of the volume of the recycled solution was done before diluting to the next concentration. The inaccuracy this caused can be solved by weighing the recycled solution before diluting, to accurately determine the volume. However, preparing a full concentration series in advance appears to be the most accurate and convenient approach, given that enough diblock is available. As mentioned, the NP solution can be recycled from the MALS-instrument and regenerated back to diblock form by the procedure described in Section 3.4.

An essential difference between the Debye plots, which can be seen in the Appendix Section C, for the standard samples and those of the NPs, is that the former have an upward slope, while the latter have a downward slope. This is due to the slope of the linear regression being $2 \cdot A_2$. For the standard samples, A_2 was positive, indicating a lower apparent molar mass. For the NPs, A_2 was negative, indicating a higher apparent molar mass. However, since the y-axis of the Debye plot displays $\frac{1}{M_w}$ and not M_w, this might seem inconsistent at first glance. Nevertheless, when plotting the concentration against M_w instead of $\frac{1}{M_w}$, the slope change signs and it can be observed that a positive A_2 lead to a lower apparent molar mass, and a negative A_2 to a higher apparent molar mass.

5.9 Peculiar findings

The sample of G_{37}-b-Dex_{43} NPs showed curious DLS results, see Table 5. Although the particle size was as expected, the DCR was unusually high. While the DCR for the other samples was no higher than about 3500, for the G_{37}-b-Dex_{43} NPs it was almost 11000. The particle size being around 10 nm larger than those of G_{16}-b-Dex_{43} and G_{16}-b-Dex_{32} is sensible because the number of G-block units are what largely impacts the particle size. Figures 33 and 34 that show the size intensity distribution and the correlation of the G_{37}-b-Dex_{43} NPs are not much different to the other figures in the DLS section, and do not provide a clear explanation for why the DCR would be so high. The size intensity distribution is shifted slightly to the right, indicating somewhat larger particles, but again, this is an expected finding. The correlation is the highest recorded for any samples included in this work, and also do not justify the abnormally high DCR. Regarding the MALS results for the G_{37}-b-Dex_{43} NPs, see Table 9, the M_w is higher than for G_{16}-b-Dex_{43} and G_{16}-b-Dex_{32}, but not overly so. A_2 is very low and also not something that raises concern. One explanation for the unusually high DCR for the G_{37}-b-Dex_{43} NPs could be that the sample contained pure G-block.

5.10 Business relevance

As discussed in the Introduction Section 1, the long-term goal with the G_m-b-Dex_n NPs is to create a radiopharmaceutical drug. From a business point of view, it is important that the characterization protocol for the NPs is as efficient and accurate as possible, while ensuring costs are kept at a manageable level. For instance, some characterization techniques may only be required in research and not in commercial production. Once an optimal preparation protocol for the NPs has been established, the finished product batch may only need a quick size verification with e.g., DLS before the batch can go on market. Given that at this point in the manufacture process the NPs would have gone through extensive characterization in the research phase, a quality control of the final product could focus on verifying that the size of the NPs has remained as intended. AFM and MALS (and SEM if improved) would then only be relevant in the research phase and not necessary for the final quality control.

An aspect that is outside the scope of this work but should be mentioned briefly is the practical implication of creating a drug containing radioactive isotopes. There is an essential time aspect that is due to the short half-life of radioactive isotopes, e.g., 12.7 hours for $^{64}Cu^{2+}$ [109]. This implies that the drug cannot necessarily be finished on the production site, and that the ion exchange must take place in clinic where the drug is administered. While the details around this are not covered in this work, it does pose the question of whether characterization of the radioactive NPs in clinic will be necessary. This characterization would focus on verifying that the ion exchange has been successful, rather than verifying size, shape, and molar mass of the NPs. Choosing the best suited characterization technique for ion exchange verification is a topic that can be explored in further research.

As touched on in the Introduction are the many side effects associated with traditional radiation treatment administered outside the body. A drug focusing its radiation on the tumor site could not only limit discomfort and ensure more efficient treatment for the patient, but also reduce time in hospital. If the side effects themselves are mild and do not require additional medical treatment and surveillance, this would save costs and capacity for hospitals. However, there is generally a high cost associated with radiopharmaceuticals in themselves [110]. Therefore, having an efficient and accurate characterization protocol in place is crucial to be able to practice efficient use of the radiopharmaceutical.

6 Conclusion

This work has focused on establishing a characterization protocol for G_m-b-Dex_n NPs. The characterization techniques AFM, SEM, DLS, and MALS and their suitability for this type of NPs have been covered in detail. It was found that a characterization protocol consisting of DLS, AFM, and MALS is suitable for characterization of G_m-b-Dex_n NPs. DLS is a convenient first step to quickly investigate the size distribution of NPs, while AFM can be used to look at the size and shape of individual NPs in detail. MALS can be utilized to determine the molar mass of the NPs. While SEM in theory can be used to investigate the size and shape of NPs, as well as their chemical composition, this work showed that this characterization technique is not ideal for the characterization of G_m-b-Dex_n NPs with the protocol presented here.

Having established a characterization protocol for G_m-b-Dex_n NPs can assist further research on the NPs in the process of creating a radiopharmaceutical drug for localized radiation treatment for cancer patients. With a solid preparation- and characterization protocol, the research focus can proceed to the biomedical aspects of the drug. The biomedical aspects include surveying which ligands are suitable to include in the NPs to encourage them to migrate to cancerous cells, how to execute the ion exchange with the radioactive isotope, and in time clinical trials to test the drug's efficiency on cancerous cells and tumors. However, there are improvements that can be made in the characterization protocol. Firstly, establishing a more efficient way to work with AFM, as the technique is time-consuming and the NPs can be difficult to locate on the substrate. Secondly, improving the preparation of concentration series for MALS will help make the molar mass measurements more accurate and the characterization work more orderly. Thirdly, working on developing the characterization protocol for SEM, with particular focus on finding a suitable substrate, optimizing imaging parameters, and enhancing the metallization process.

AFM provides information about the topography of a sample, which within the scope of this work translates to the size and shape of NPs. The key advantage of AFM is great resolution at the nm scale, which is accompanied with its key drawback of being a time-consuming technique. SEM offers topographical information as well as chemical composition of a sample. Its upper hand lies in the array of different signals emitted, however, it is disadvantageous in that it requires conductive samples. DLS is a quick and easy technique to obtain the size distribution of particles. Its main downside is the low resolution. MALS yields the molar mass of particles. It is the only one of these four characterization techniques that can supply information about a particle's molar mass, which becomes its main advantage. Its key shortcoming is that it is highly concentration-sensitive and thus can be complicated to operate.

This work has highlighted both the advantages and drawbacks of these characterization methods. AFM has provided invaluable size- and shape information about individual NPs, with a resolution that remains unmatched. However, a great deal of time was spent on AFM images with few satisfactory images resulting. A main challenge remains locating the NPs on the mica substrate. If the SEM protocol for the NPs can be improved, this technique can become useful because it is (given sufficient resolution) significantly easier to locate specific features of a sample with SEM than it is with AFM. While DLS has the drawback of low resolution, this is only a minor concern in its application on the NPs. As DLS has proved to be a convenient and valuable first step of the characterization, it can be accepted that the resolution is not optimal when combined with a high-resolution technique such as AFM. MALS stands out as the only one of the four characterization techniques that can determine the molar mass of the NPs. However, the operational protocol for MALS requires improvement. In particular, ensuring accurate concentrations is crucial for valid MALS-results.

This work builds upon the works of Solberg [14] and Røgenes [13]. While these works touch on G_m-b-Dex_n NPs and characterization with AFM and DLS, a comprehensive characterization protocol had not yet been established. Therefore, this work has been heavily focused on the characterization of G_m-b-Dex_n NPs, and has presented a thorough review of the different characterization techniques. The significance of this is that it brings the research on G_m-b-Dex_n NPs one step closer to the end goal of developing a radiopharmaceutical drug. Without a clear and comprehensive characterization protocol, the preparation of the NPs cannot be monitored, and the quality of the end product cannot be ensured. This would have been a major roadblock on the path of the pharmaceutical product development. Moving forward, a characterization technique that can be used to monitor the ion exchange with radioactive isotopes can be investigated.

The optimal characterization protocol for G$_m$-b-Dex$_n$ NPs is starting with gaining a quick overview of the size distribution using DLS, examining the size and shape in more detail with AFM, and finally assess the molar mass using MALS. The path to a finished pharmaceutical product is a long one, and it requires an array of different research aspects, including an optimized characterization protocol.

Bibliography

[1] M. Fata Moradali and Bernd H. A. Rehm. 'Bacterial biopolymers: from pathogenesis to advanced materials'. In: *Nature Reviews Microbiology* 18.4 (Apr. 2020), pp. 195–210. ISSN: 1740-1526. DOI: 10.1038/s41579-019-0313-3.

[2] Jaya Baranwal et al. 'Biopolymer: A Sustainable Material for Food and Medical Applications'. In: *Polymers* 14.5 (Feb. 2022), p. 983. ISSN: 2073-4360. DOI: 10.3390/polym14050983.

[3] Preeti Yadav. 'Biomedical Biopolymers, their Origin and Evolution in Biomedical Sciences: A Systematic Review'. In: *JOURNAL OF CLINICAL AND DIAGNOSTIC RESEARCH* (2015). ISSN: 2249782X. DOI: 10.7860/JCDR/2015/13907.6565.

[4] Welela Meka Kedir et al. 'Pharmaceutical and drug delivery applications of chitosan biopolymer and its modified nanocomposite: A review'. In: *Heliyon* 8.8 (Aug. 2022), e10196. ISSN: 24058440. DOI: 10.1016/j.heliyon.2022.e10196.

[5] Neelam Pathak et al. 'Biopolymeric nanoparticles based effective delivery of bioactive compounds toward the sustainable development of anticancerous therapeutics'. In: *Frontiers in Nutrition* 9 (July 2022). ISSN: 2296-861X. DOI: 10.3389/fnut.2022.963413.

[6] Kuen Yong Lee and David J. Mooney. 'Alginate: Properties and biomedical applications'. In: *Progress in Polymer Science (Oxford)* 37.1 (2012), pp. 106–126. ISSN: 00796700. DOI: 10.1016/j.progpolymsci.2011.06.003.

[7] Jinchen Sun and Huaping Tan. 'Alginate-based biomaterials for regenerative medicine applications'. In: *Materials* 6.4 (2013), pp. 1285–1309. ISSN: 19961944. DOI: 10.3390/ma6041285.

[8] International Atomic Energy Agency. *Diagnostic radiopharmaceuticals.* URL: https://www.iaea.org/topics/diagnostic-radiopharmaceuticals#:~:text=Radiopharmaceuticals%20are%20radioisotopes%20bound%20to,for%20the%20therapy%20of%20diseases..

[9] National Cancer Institute. *Radiopharmaceuticals: Radiation Therapy Enters the Molecular Age.* 2020. URL: https://www.cancer.gov/news-events/cancer-currents-blog/2020/radiopharmaceuticals-cancer-radiation-therapy.

[10] National Cancer Institute. *Radiation Therapy Side Effects.* URL: https://www.cancer.gov/about-cancer/treatment/types/radiation-therapy/side-effects.

[11] NHS. *Side effects Radiotherapy.* URL: https://www.nhs.uk/conditions/radiotherapy/side-effects/.

[12] Cancer Australia. *Radiation therapy.* URL: https://www.canceraustralia.gov.au/content/radiation-therapy.

[13] Ingrid Christine Røgenes. *Alginate-based self-assembling nanoparticles.* Tech. rep. Trondheim: Norwegian University of Science and Technology, Dec. 2022.

[14] Amalie Solberg. 'Self-assembling alginate-based diblock polymers'. PhD thesis. Trondheim: Norwegian University of Science and Technology, Feb. 2022. ISBN: 978-82-326-6414-6.

[15] Hadas Hecht and Simcha Srebnik. 'Structural Characterization of Sodium Alginate and Calcium Alginate'. In: *Biomacromolecules* 17.6 (June 2016), pp. 2160–2167. ISSN: 15264602. DOI: 10.1021/acs.biomac.6b00378.

[16] Amalie Solberg et al. 'Alginate-based diblock polymers: Preparation, characterization and Ca-induced self-assembly'. In: *Polymer Chemistry* 12.38 (Oct. 2021), pp. 5412–5425. ISSN: 17599962. DOI: 10.1039/d1py00727k.

[17] National Center for Biotechnology Information. *PubChem Compound Summary for CID 446401, alpha-L-Gulopyranuronic acid.* 2023. URL: https://pubchem.ncbi.nlm.nih.gov/compound/alpha-L-Gulopyranuronic-acid.

[18] National Center for Biotechnology Information. *PubChem Compound Summary for CID 446145, beta-D-Mannopyranuronic acid.* 2023. URL: https://pubchem.ncbi.nlm.nih.gov/compound/beta-D-Mannopyranuronic-acid.

[19] Olivia Eskens, Gianna Villani and Samiul Amin. 'Rheological investigation of thermoresponsive alginate-methylcellulose gels for epidermal growth factor formulation'. In: *Cosmetics* 8.1 (Jan. 2021), pp. 1–11. ISSN: 20799284. DOI: 10.3390/COSMETICS8010003.

[20] G Orive et al. ‘Biocompatibility of microcapsules for cell immobilization elaborated with different type of alginates’. In: *Biomaterials* 23.18 (Sept. 2002), pp. 3825–3831. ISSN: 01429612. DOI: 10.1016/S0142-9612(02)00118-7.

[21] Mariana Isabel Neves, Lorenzo Moroni and Cristina Carvalho Barrias. ‘Modulating Alginate Hydrogels for Improved Biological Performance as Cellular 3D Microenvironments’. In: *Frontiers in Bioengineering and Biotechnology* 8 (June 2020). ISSN: 22964185. DOI: 10.3389/fbioe.2020.00665.

[22] Hua Liao et al. ‘Mechanisms of oligoguluronate modulating the calcium-induced gelation of alginate’. In: *Polymer* 74 (Aug. 2015), pp. 166–175. ISSN: 00323861. DOI: 10.1016/j.polymer.2015.08.007.

[23] Akila Merakchi et al. ‘Cross-linking and modification of sodium alginate biopolymer for dye removal in aqueous solution’. In: *Polymer Bulletin* 76.7 (July 2019), pp. 3535–3554. ISSN: 14362449. DOI: 10.1007/s00289-018-2557-x.

[24] R. J. Dimler et al. ‘Interpretation of Periodate Oxidation Data on Degraded Dextran’. In: *J. Am. Chem. Soc.* 77.24 (1955), pp. 6568–6573. DOI: 10.1021/ja01629a044.

[25] J. W. Van Cleve, W. C. Schaefer and C. E. Rist. ‘The Structure of NRRL B-512 Dextran. Methylation Studies ’. In: *Journal of the American Chemical Society* 78.17 (Sept. 1956), pp. 4435–4438. ISSN: 0002-7863. DOI: 10.1021/ja01598a064.

[26] Farwa Sarwat et al. ‘Production & Characterization of a Unique Dextran from an Indigenous Leuconostoc mesenteroides CMG713’. In: *Int. J. Biol. Sci* 4.6 (2008), pp. 379–386. ISSN: 1449-2288. DOI: 10.7150/ijbs.4.379.

[27] Elsa Díaz-Montes. ‘Dextran: Sources, Structures, and Properties’. In: *Polysaccharides* 2.3 (July 2021), pp. 554–565. DOI: 10.3390/polysaccharides2030033.

[28] Olle Larm, Bengt Lindberg and Sigfrid Svensson. ‘Studies on the length of the side chains of the dextran elaborated by Leuconostoc mesenteroides NRRL B-512*’. In: *Carbohyd. Res.* 20 (1971), pp. 39–48. DOI: 10.1016/S0008-6215(00)84947-2.

[29] F. A. Bovey. ‘Enzymatic polymerization. I. Molecular weight and branching during the formation of dextran’. In: *Journal of Polymer Science* 35.128 (Feb. 1959), pp. 167–182. ISSN: 00223832. DOI: 10.1002/pol.1959.1203512813.

[30] Lester H. Arond and H. Peter Frank. ‘Molecular Weight Distribution and Molecular Size of a Native Dextran’. In: *The Journal of Physical Chemistry* 58.11 (Nov. 1954), pp. 953–957. ISSN: 0022-3654. DOI: 10.1021/j150521a006.

[31] Hans-Georg Elias. ‘Ultrazentrifugen- und Diffusionsmessungen an nicht-Newtonschen Lösungen nativer Dextrane. Über extrem große Makromoleküle. IV’. In: *Die Makromolekulare Chemie* 33.1 (1959), pp. 166–180. ISSN: 0025116X. DOI: 10.1002/macp.1959.020330112.

[32] E. Antonini et al. ‘Studies on dextran and dextran derivatives. I. Properties of native dextran in different solvents’. In: *Biopolymers* 2.1 (1964), pp. 27–34. ISSN: 10970282. DOI: 10.1002/bip.1964.360020105.

[33] Andrea N. Trementozzi et al. ‘Gap Junction-Mediated Delivery of Polymeric Macromolecules’. In: *ACS Biomaterials Science & Engineering* 8.4 (Apr. 2022), pp. 1566–1572. ISSN: 2373-9878. DOI: 10.1021/acsbiomaterials.1c01459.

[34] Jian-Min Yuan et al. ‘The effects of macromolecular crowding on the mechanical stability of protein molecules’. In: *Protein Science* 17.12 (Dec. 2008), pp. 2156–2166. ISSN: 0961-8368. DOI: 10.1110/ps.037325.108.

[35] João Maia et al. *Carbohydrates applications in medicine.* 2014, pp. 31–53. ISBN: 9788130805238.

[36] Anastasia S. Volokhova, Kevin J. Edgar and John B. Matson. ‘Polysaccharide-containing block copolymers: Synthesis and applications’. In: *Materials Chemistry Frontiers* 4.1 (Jan. 2020), pp. 99–112. ISSN: 20521537. DOI: 10.1039/c9qm00481e.

[37] Dilusha S. Dalpathado et al. ‘Reductive amination of carbohydrates using NaBH(OAc)3’. In: *Analytical and Bioanalytical Chemistry* 381.6 (Mar. 2005), pp. 1130–1137. ISSN: 16182642. DOI: 10.1007/s00216-004-3028-9.

[38] Merck KGaA. *O,O-1,3-Propanediylbishydroxylamine dihydrochloride.* URL: https://www.sigmaaldrich.com/NO/en/product/aldrich/689122.

[39] National Center for Biotechnology Information. *PubChem Compound Summary for CID 87535645*. 2023. URL: https://pubchem.ncbi.nlm.nih.gov/compound/87535645.

[40] Merck KGaA. *2-Methylpyridine borane complex*. URL: https://www.sigmaaldrich.com/NO/en/product/aldrich/654213.

[41] Ingrid Vikøren Mo et al. 'Activation of enzymatically produced chitooligosaccharides by dioxyamines and dihydrazides'. In: *Carbohydrate Polymers* 232 (Mar. 2020). ISSN: 01448617. DOI: 10.1016/j.carbpol.2019.115748.

[42] National Center for Biotechnology Information. *PubChem Substance Record for SID 24884021, 2-Methylpyridine borane complex solution, 95%, Source: Sigma-Aldrich*. 2023. URL: https://pubchem.ncbi.nlm.nih.gov/substance/24884021.

[43] Paula Hong, Stephan Koza and Edouard S.P. Bouvier. 'A review size-exclusion chromatography for the analysis of protein biotherapeutics and their aggregates'. In: *Journal of Liquid Chromatography and Related Technologies* 35.20 (Jan. 2012), pp. 2923–2950. ISSN: 10826076. DOI: 10.1080/10826076.2012.743724.

[44] Tung Yung Huang, Lang Ming Chi and Kun Yi Chien. 'Size-exclusion chromatography using reverse-phase columns for protein separation'. In: *Journal of Chromatography A* 1571 (Oct. 2018), pp. 201–212. ISSN: 18733778. DOI: 10.1016/j.chroma.2018.08.020.

[45] Valentina La Verde, Paola Dominici and Alessandra Astegno. 'Determination of Hydrodynamic Radius of Proteins by Size Exclusion Chromatography'. In: *BIO-PROTOCOL* 7.8 (2017). ISSN: 2331-8325. DOI: 10.21769/BioProtoc.2230.

[46] Elena Uliyanchenko. 'Size-exclusion chromatography - From high-performance to ultra-performance'. In: *Analytical and Bioanalytical Chemistry* 406.25 (Oct. 2014), pp. 6087–6094. ISSN: 16182650. DOI: 10.1007/s00216-014-8041-z.

[47] Daniel Some et al. 'Characterization of Proteins by Size-Exclusion Chromatography Coupled to Multi-Angle Light Scattering (SEC-MALS)'. In: *Journal of Visualized Experiments* 148 (June 2019). ISSN: 1940-087X. DOI: 10.3791/59615.

[48] Daniela Held and Peter Kilz. 'Size-exclusion chromatography as a useful tool for the assessment of polymer quality and determination of macromolecular properties'. In: *Chemistry Teacher International* 3.2 (June 2021), pp. 77–103. ISSN: 25693263. DOI: 10.1515/cti-2020-0024.

[49] Ken Broeckhoven, Konstantin Shoykhet and Michael W. Dong. 'Modern HPLC Pumps: Perspectives, Principles, and Practices'. In: *LCGC North America* 37.6 (June 2019), pp. 374–384.

[50] James H. Wade and Ryan C. Bailey. 'Refractive index-based detection of gradient elution liquid chromatography using chip-integrated microring resonator arrays'. In: *Analytical Chemistry* 86.1 (Jan. 2014), pp. 913–919. ISSN: 00032700. DOI: 10.1021/ac4035828.

[51] Robert P. Mazzarese et al. 'Chromatography Data Systems: Perspectives, Principles, and Trends'. In: *LCGC North America* 37.12 (Dec. 2019), pp. 852–865.

[52] Andre J. Simpson, Myrna J. Simpson and Ronald Soong. 'Nuclear magnetic resonance spectroscopy and its key role in environmental research'. In: *Environmental Science and Technology* 46.21 (Nov. 2012), pp. 11488–11496. ISSN: 0013936X. DOI: 10.1021/es302154w.

[53] Komal Zia et al. 'Nuclear Magnetic Resonance Spectroscopy for Medical and Dental Applications: A Comprehensive Review'. In: *European Journal of Dentistry* 13.01 (Feb. 2019), pp. 124–128. ISSN: 1305-7456. DOI: 10.1055/s-0039-1688654.

[54] Ron Darbeau. 'Nuclear magnetic resonance (NMR) spectroscopy: A review and a look at its use as a probative tool in deamination chemistry'. In: *Applied Spectroscopy Reviews* 41.4 (2006), pp. 401–425. ISSN: 05704928. DOI: 10.1080/05704920600726175.

[55] P Konzbul and K Sveda. 'Shim coils for NMR and MRI solenoid magnets'. In: *Measurement Science and Technology* 6.8 (Aug. 1995), pp. 1116–1123. ISSN: 0957-0233. DOI: 10.1088/0957-0233/6/8/005.

[56] P Eaton and P West. *Atomic Force Microscopy*. Oxford University Press, 2010. ISBN: 978-0-19-957045-4.

[57] H. J. Quenzer et al. 'Fabrication of conducting AFM cantilevers with AlN-based piezoelectric actuators'. In: *Procedia Engineering.* Vol. 25. 2011, pp. 665–668. DOI: 10.1016/j.proeng.2011.12.164.

[58] Yves F. Dufrêne et al. 'Imaging modes of atomic force microscopy for application in molecular and cell biology'. In: *Nature Nanotechnology* 12.4 (May 2017), pp. 295–307. ISSN: 17483395. DOI: 10.1038/nnano.2017.45.

[59] Miguel Angel Sánchez Quintanilla. 'Surface Analysis Using Contact Mode AFM'. In: *Encyclopedia of Tribology.* Boston, MA: Springer US, 2013, pp. 3401–3411. DOI: 10.1007/978-0-387-92897-5_323.

[60] Xiangying Deng et al. 'Application of atomic force microscopy in cancer research'. In: *Journal of Nanobiotechnology* 16.1 (Dec. 2018), p. V. ISSN: 14773155. DOI: 10.1186/s12951-018-0428-0.

[61] Universität Greifswald. *AFM (Atomic Force Microscopy).* URL: https://physik.uni-greifswald.de/en/research-groups/soft-matter-and-biophysics-prof-christiane-helm/methods/afm-atomic-force-microscope/.

[62] Bruker. *AFM Modes.* URL: https://www.bruker.com/en/products-and-solutions/microscopes/materials-afm/afm-modes.html.

[63] Zurich Instruments AG. *Non-Contact Atomic Force Microscopy (NC-AFM).* URL: https://www.zhinst.com/europe/en/applications/scanning-probe-microscopy/non-contact-atomic-force-microscopy-nc-afm.

[64] Miloslav Capek, Lukas Jelinek and Guy A.E. Vandenbosch. 'Stored electromagnetic energy and quality factor of radiating structures'. In: *Proceedings of the Royal Society A: Mathematical, Physical and Engineering Sciences* 472.2188 (Apr. 2016). ISSN: 14712946. DOI: 10.1098/rspa.2015.0870.

[65] S. B. Kaemmer. *Introduction to Bruker's ScanAsyst and PeakForce Tapping AFM Technology.* URL: https://blog.brukerafmprobes.com/wp-content/uploads/2015/08/AN133-Introduction_to_Brukers_ScanAsyst_and_PeakForce_Tapping_Atomic_Force_Microscopy_Technology_AFM_AN133.pdf.

[66] Hollis Williams. 'SEM for conductive and non-conductive specimens'. In: *Phys. Educ.* 56 (Aug. 2021). DOI: 10.1088/1361-6552/ac1503.

[67] Kirti Prakash et al. 'Super-resolution microscopy: A brief history and new avenues'. In: *Philosophical Transactions of the Royal Society A: Mathematical, Physical and Engineering Sciences* 380.2220 (2022). ISSN: 1364503X. DOI: 10.1098/rsta.2021.0110.

[68] E. Abbe. 'Beiträge zur Theorie des Mikroskops und der mikroskopischen Wahrnehmung'. In: *Archiv für Mikroskopische Anatomie* 9.1 (Dec. 1873), pp. 413–468. ISSN: 0176-7364. DOI: 10.1007/BF02956173.

[69] Thermo Fisher Scientific. *Apreo 2 SEM.* 2023. URL: https://www.thermofisher.com/no/en/home/electron-microscopy/products/scanning-electron-microscopes/apreo-sem.html.

[70] Daisuke Koga et al. 'Applications of Scanning Electron Microscopy Using Secondary and Backscattered Electron Signals in Neural Structure'. In: *Frontiers in Neuroanatomy* 15 (Dec. 2021). ISSN: 1662-5129. DOI: 10.3389/fnana.2021.759804.

[71] Thomas Kowoll et al. 'Contrast of Backscattered Electron SEM Images of Nanoparticles on Substrates with Complex Structure'. In: *Scanning* 2017 (2017), pp. 1–12. ISSN: 0161-0457. DOI: 10.1155/2017/4907457.

[72] Erich Müller, Milena Hugenschmidt and Dagmar Gerthsen. 'Electron-beam broadening in electron microscopy by solving the electron transport equation'. In: *Physical Review Research* 2.4 (Dec. 2020), p. 043313. ISSN: 2643-1564. DOI: 10.1103/PhysRevResearch.2.043313.

[73] Antonis Nanakoudis. *SEM: Types of Electrons and the Information They Provide.* 2019. URL: https://www.thermofisher.com/blog/materials/sem-signal-types-electrons-and-the-information-they-provide/.

[74] Victory Armida Janine Jaques et al. 'Conductive cross-section preparation of non-conductive painting micro-samples for SEM analysis'. In: *Scientific Reports* 12.1 (Nov. 2022), p. 19650. ISSN: 2045-2322. DOI: 10.1038/s41598-022-21882-1.

[75] Alexander V. Malm and Jason C.W. Corbett. 'Improved Dynamic Light Scattering using an adaptive and statistically driven time resolved treatment of correlation data'. In: *Scientific Reports* 9.1 (Dec. 2019). ISSN: 20452322. DOI: 10.1038/s41598-019-50077-4.

[76] M. Naiim et al. 'Multiangle dynamic light scattering for the improvement of multimodal particle size distribution measurements'. In: *Soft Matter* 11.1 (Jan. 2015), pp. 28–32. ISSN: 17446848. DOI: 10.1039/c4sm01995d.

[77] Jörg Stetefeld, Sean A. McKenna and Trushar R. Patel. 'Dynamic light scattering: a practical guide and applications in biomedical sciences'. In: *Biophysical Reviews* 8.4 (Dec. 2016), pp. 409–427. ISSN: 18672469. DOI: 10.1007/s12551-016-0218-6.

[78] Puthusserickal A. Hassan, Suman Rana and Gunjan Verma. 'Making sense of Brownian motion: Colloid characterization by dynamic light scattering'. In: *Langmuir* 31.1 (Jan. 2015), pp. 3–12. ISSN: 15205827. DOI: 10.1021/la501789z.

[79] Sven Falke and Christian Betzel. 'Dynamic Light Scattering (DLS)'. In: *Radiation in Bioanalysis* 8 (Sept. 2019), pp. 173–193. DOI: 10.1007/978-3-030-28247-9_6.

[80] Yuanheng Xiong, Xiaodong Zhang and Lianbo Hu. 'A method for tracking the Brownian motion to estimate the size distribution of submicron particles in seawater'. In: *Limnology and Oceanography: Methods* 20.7 (July 2022), pp. 373–386. ISSN: 15415856. DOI: 10.1002/lom3.10494.

[81] Ragy Ragheb and Ulf Nobbmann. 'Multiple scattering effects on intercept, size, polydispersity index, and intensity for parallel (VV) and perpendicular (VH) polarization detection in photon correlation spectroscopy'. In: *Scientific Reports* 10.1 (Dec. 2020). ISSN: 20452322. DOI: 10.1038/s41598-020-78872-4.

[82] Oksana Leszczyszyn. *In pursuit of perfect data: DLS correlation function.* Nov. 2012. URL: https://www.materials-talks.com/in-pursuit-of-perfect-data-dls-correlation-function/.

[83] Mengjie Wang et al. 'Particle size measurement using dynamic light scattering at ultra-low concentration accounting for particle number fluctuations'. In: *Materials* 14.19 (Oct. 2021). ISSN: 19961944. DOI: 10.3390/ma14195683.

[84] Horiba Scientific. *Choosing the Concentration Range for DLS Size Measurement.* URL: https://www.horiba.com/int/scientific/technologies/dynamic-light-scattering-dls-particle-size-distribution-analysis/concentration-range-for-dls-size-measurement/.

[85] Ulf Nobbmann. *Derived count rate – what is it?* 2015. URL: https://www.materials-talks.com/derived-count-rate-what-is-it/.

[86] Ulf Nobbmann. *Multi Angle Light Scattering (MALS).* 2014. URL: https://www.materials-talks.com/multi-angle-light-scattering-mals/.

[87] Bhumit A. Patel et al. 'Multi-angle light scattering as a process analytical technology measuring real-time molecular weight for downstream process control'. In: *mAbs* 10.7 (Oct. 2018), pp. 945–950. ISSN: 19420870. DOI: 10.1080/19420862.2018.1505178.

[88] Bruno H. Zimm. 'The Scattering of Light and the Radial Distribution Function of High Polymer Solutions'. In: *The Journal of Chemical Physics* 16.12 (Dec. 1948), pp. 1093–1099. ISSN: 0021-9606. DOI: 10.1063/1.1746738.

[89] Philip J. Wyatt. 'Light scattering and the absolute characterization of macromolecules'. In: *Analytica Chimica Acta* 272.1 (Feb. 1993), pp. 1–40. ISSN: 00032670. DOI: 10.1016/0003-2670(93)80373-S.

[90] Wyatt Technology. *Understanding Multi-Angle Static Light Scattering.* URL: https://www.wyatt.com/library/theory/multi-angle-light-scattering-theory.html.

[91] Allan H. Harvey and Eric W. Lemmon. 'Correlation for the Second Virial Coefficient of Water'. In: *Journal of Physical and Chemical Reference Data* 33.1 (2004), pp. 369–376. ISSN: 00472689. DOI: 10.1063/1.1587731.

[92] Sanbo Qin and Huan Xiang Zhou. 'Calculation of Second Virial Coefficients of Atomistic Proteins Using Fast Fourier Transform'. In: *Journal of Physical Chemistry B* 123.39 (Oct. 2019), pp. 8203–8215. ISSN: 15205207. DOI: 10.1021/acs.jpcb.9b06808.

[93] Taira Oohashi, Kouta Inoue and Yo Nakamura. 'Second and third virial coefficients of low-molecular-weight polyisoprene in 1,4-dioxane'. In: *Polymer Journal* 46.10 (Jan. 2014), pp. 699–703. ISSN: 13490540. DOI: 10.1038/pj.2014.43.

[94] Wyatt Technology. *Understanding Dynamic Light Scattering.* 2023. URL: https://www.wyatt.com/library/theory/dynamic-light-scattering-theory.html.

[95] Chandy Kim, André Deratani and Frédéric Bonfils. 'DETERMINATION OF THE REFRACTIVE INDEX INCREMENT OF NATURAL AND SYNTHETIC POLY(CIS-1,4-ISOPRENE) SOLUTIONS AND ITS EFFECT ON STRUCTURAL PARAMETERS'. In: *Journal of Liquid Chromatography & Related Technologies* 33.1 (Dec. 2009), pp. 37–45. ISSN: 1082-6076. DOI: 10.1080/10826070903427072.

[96] Ted Pella. *Properties & Chemical Composition of Mica Grade V1 Grade Classification of Muscovite Mica.* URL: https://www.tedpella.com/Vacuum_html/Mica_Grade_V1_Properties.aspx.

[97] Ted Pella. *Conductive Adhesives Tabs, Tapes and Sheets Carbon, Aluminum, Copper, Silver.* URL: https://www.tedpella.com/SEMmisc_html/SEMadhes.aspx#_16084-1.

[98] Bruker. *SCANASYST-AIR.* URL: https://www.brukerafmprobes.com/p-3726-scanasyst-air.aspx.

[99] Pharmacosmos. *Dextran Standard 2000.* 2023. URL: https://www.dextran.com/products/dextran-standards-gpc-standards/dextran-2000/c-24/c-73/p-1511.

[100] Shoshy Mizrahy and Dan Peer. 'Polysaccharides as building blocks for nanotherapeutics'. In: *Chem. Soc. Rev.* 41.7 (2012), pp. 2623–2640. ISSN: 0306-0012. DOI: 10.1039/C1CS15239D.

[101] Robby A. Petros and Joseph M. DeSimone. 'Strategies in the design of nanoparticles for therapeutic applications'. In: *Nature Reviews Drug Discovery* 9.8 (Aug. 2010), pp. 615–627. ISSN: 1474-1776. DOI: 10.1038/nrd2591.

[102] Leon Alexander. 'Extravasation Injuries: A Trivial Injury Often Overlooked with Disastrous Consequences'. In: *WORLD JOURNAL OF PLASTIC SURGERY* 9.3 (Sept. 2020), pp. 326–330. ISSN: 2228-7914. DOI: 10.29252/wjps.9.3.326.

[103] D. Craig Brater. 'Measurement of renal function during drug development'. In: *British Journal of Clinical Pharmacology* 54.1 (July 2002), pp. 87–95. ISSN: 03065251. DOI: 10.1046/j.1365-2125.2002.01625.x.

[104] Parisa Foroozandeh and Azlan Abdul Aziz. 'Insight into Cellular Uptake and Intracellular Trafficking of Nanoparticles'. In: *Nanoscale Research Letters* 13.1 (Dec. 2018), p. 339. ISSN: 1931-7573. DOI: 10.1186/s11671-018-2728-6.

[105] Ilse Gosens et al. 'Impact of agglomeration state of nano- and submicron sized gold particles on pulmonary inflammation'. In: *Particle and Fibre Toxicology* 7.1 (2010), p. 37. ISSN: 1743-8977. DOI: 10.1186/1743-8977-7-37.

[106] Mohamed Yassine Amarouch, Jaouad El Hilaly and Driss Mazouzi. 'AFM and FluidFM Technologies: Recent Applications in Molecular and Cellular Biology'. In: *Scanning* 2018 (July 2018), pp. 1–10. ISSN: 0161-0457. DOI: 10.1155/2018/7801274.

[107] André Meister et al. 'FluidFM: Combining Atomic Force Microscopy and Nanofluidics in a Universal Liquid Delivery System for Single Cell Applications and Beyond'. In: *Nano Letters* 9.6 (June 2009), pp. 2501–2507. ISSN: 1530-6984. DOI: 10.1021/nl901384x.

[108] Rizwan Ali, Kheireddine El-Boubbou and Mohamed Boudjelal. 'An easy, fast and inexpensive method of preparing a biological specimen for scanning electron microscopy (SEM)'. In: *MethodsX* 8 (Sept. 2021). ISSN: 22150161. DOI: 10.1016/j.mex.2021.101521.

[109] Carolyn J. Anderson and Riccardo Ferdani. 'Copper-64 Radiopharmaceuticals for PET Imaging of Cancer: Advances in Preclinical and Clinical Research'. In: *Cancer Biotherapy and Radiopharmaceuticals* 24.4 (Aug. 2009), pp. 379–393. ISSN: 1084-9785. DOI: 10.1089/cbr.2009.0674.

[110] Ali Al Ahmed and Khaled Al-Surimi. 'Improving efficiency management of radiopharmaceutical materials at a nuclear medicine department'. In: *BMJ Quality Improvement Reports* 4.1 (Sept. 2015), u208970.w3709. ISSN: 2050-1315. DOI: 10.1136/bmjquality.u208970.w3709.

Appendix

A Direct titration calculation

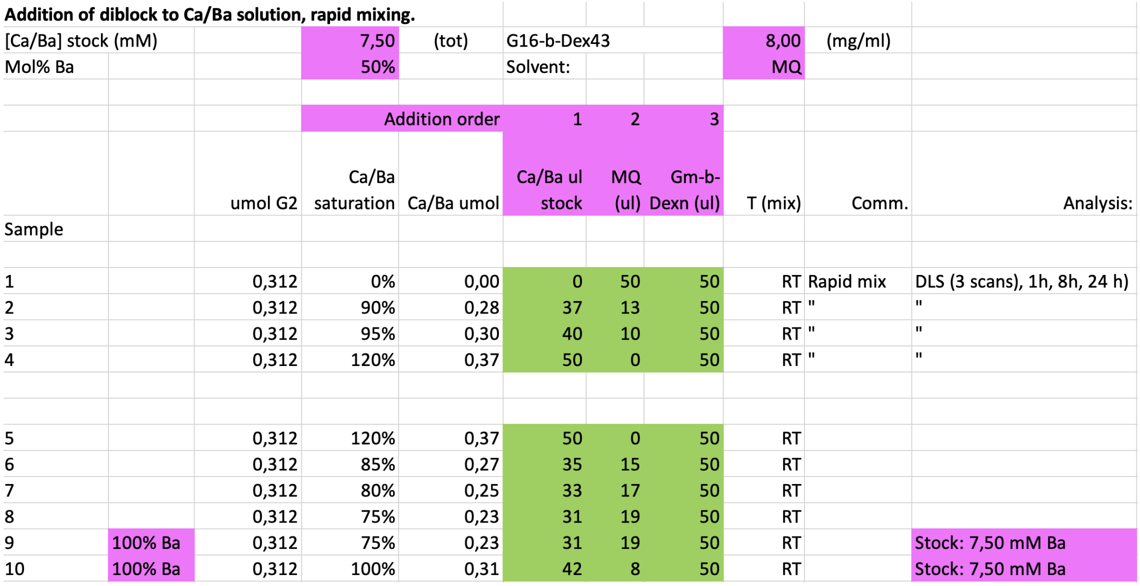

Addition of diblock to Ca/Ba solution, rapid mixing.										
[Ca/Ba] stock (mM)			7,50	(tot)	G16-b-Dex43			8,00	(mg/ml)	
Mol% Ba			50%		Solvent:			MQ		
				Addition order	1	2	3			
		umol G2	Ca/Ba saturation	Ca/Ba umol	Ca/Ba ul stock	MQ (ul)	Gm-b-Dexn (ul)	T (mix)	Comm.	Analysis:
Sample										
1		0,312	0%	0,00	0	50	50	RT	Rapid mix	DLS (3 scans), 1h, 8h, 24 h)
2		0,312	90%	0,28	37	13	50	RT	"	"
3		0,312	95%	0,30	40	10	50	RT	"	"
4		0,312	120%	0,37	50	0	50	RT	"	"
5		0,312	120%	0,37	50	0	50	RT		
6		0,312	85%	0,27	35	15	50	RT		
7		0,312	80%	0,25	33	17	50	RT		
8		0,312	75%	0,23	31	19	50	RT		
9	100% Ba	0,312	75%	0,23	31	19	50	RT		Stock: 7,50 mM Ba
10	100% Ba	0,312	100%	0,31	42	8	50	RT		Stock: 7,50 mM Ba

Figure 51: The Excel-spreadsheet used to calculate the different amounts to be added for various saturation percentages of NPs by direct titration. The spreadsheet was developed by Elise Holmås.

B DLS data processing

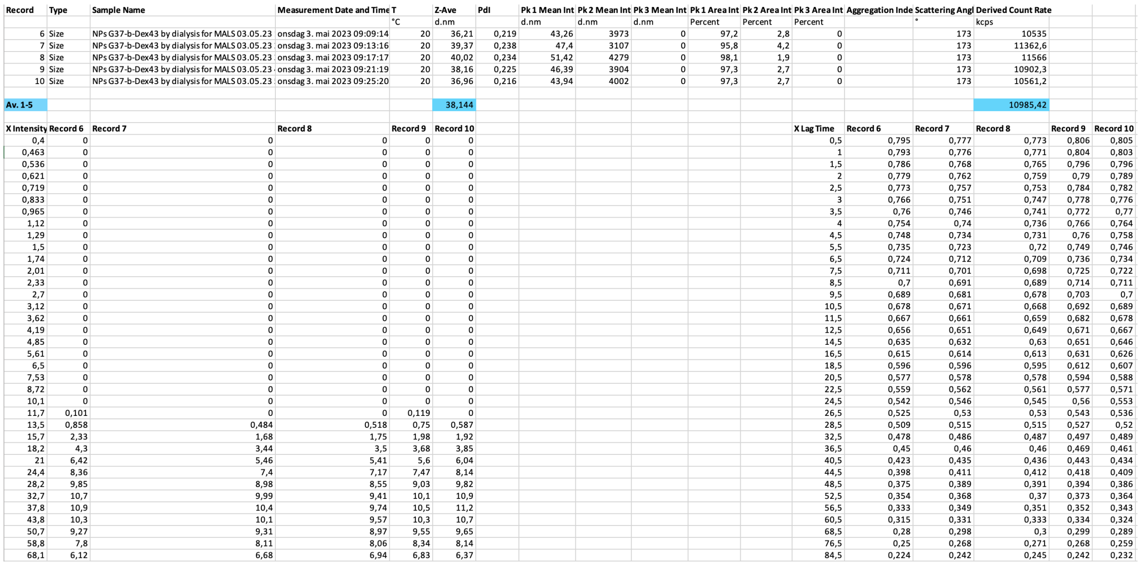

Record	Type	Sample Name	Measurement Date and Time	T	Z-Ave	PdI	Pk 1 Mean Int	Pk 2 Mean Int	Pk 3 Mean Int	Pk 1 Area Int	Pk 2 Area Int	Pk 3 Area Int	Aggregation Inde	Scattering Angl	Derived Count Rate
				°C	d.nm		d.nm	d.nm	d.nm	Percent	Percent	Percent		°	kcps
6	Size	NPs G37-b-Dex43 by dialysis for MALS 03.05.23	onsdag 3. mai 2023 09:09:14	20	36,21	0,219	43,26	3973	0	97,2	2,8	0		173	10535
7	Size	NPs G37-b-Dex43 by dialysis for MALS 03.05.23	onsdag 3. mai 2023 09:13:16	20	39,37	0,238	47,4	3107	0	95,8	4,2	0		173	11362,6
8	Size	NPs G37-b-Dex43 by dialysis for MALS 03.05.23	onsdag 3. mai 2023 09:17:17	20	40,02	0,234	51,42	4279	0	98,1	1,9	0		173	11566
9	Size	NPs G37-b-Dex43 by dialysis for MALS 03.05.23	onsdag 3. mai 2023 09:21:19	20	38,16	0,225	46,39	3904	0	97,3	2,7	0		173	10902,3
10	Size	NPs G37-b-Dex43 by dialysis for MALS 03.05.23	onsdag 3. mai 2023 09:25:20	20	36,96	0,216	43,94	4002	0	97,3	2,7	0		173	10561,2
Av. 1-5					38,144										10985,42

X Intensity	Record 6	Record 7	Record 8	Record 9	Record 10
0,4	0	0	0	0	0
0,463	0	0	0	0	0
0,536	0	0	0	0	0
0,621	0	0	0	0	0
0,719	0	0	0	0	0
0,833	0	0	0	0	0
0,965	0	0	0	0	0
1,12	0	0	0	0	0
1,29	0	0	0	0	0
1,5	0	0	0	0	0
1,74	0	0	0	0	0
2,01	0	0	0	0	0
2,33	0	0	0	0	0
2,7	0	0	0	0	0
3,12	0	0	0	0	0
3,62	0	0	0	0	0
4,19	0	0	0	0	0
4,85	0	0	0	0	0
5,61	0	0	0	0	0
6,5	0	0	0	0	0
7,53	0	0	0	0	0
8,72	0	0	0	0	0
10,1	0	0	0	0	0
11,7	0,101	0	0	0,119	0
13,5	0,858	0,484	0,518	0,75	0,587
15,7	2,33	1,68	1,75	1,98	1,92
18,2	4,3	3,44	3,5	3,68	3,85
21	6,42	5,46	5,41	5,6	6,04
24,4	8,36	7,4	7,17	7,47	8,14
28,2	9,85	8,98	8,55	9,03	9,82
32,7	10,7	9,99	9,41	10,1	10,9
37,8	10,9	10,4	9,74	10,5	11,2
43,8	10,3	10,1	9,57	10,3	10,7
50,7	9,27	9,31	8,97	9,55	9,65
58,8	7,8	8,11	8,06	8,34	8,14
68,1	6,12	6,68	6,94	6,83	6,37

X Lag Time	Record 6	Record 7	Record 8	Record 9	Record 10
0,5	0,795	0,777	0,773	0,806	0,805
1	0,793	0,776	0,771	0,804	0,803
1,5	0,786	0,768	0,765	0,796	0,796
2	0,779	0,762	0,759	0,79	0,789
2,5	0,773	0,757	0,753	0,784	0,782
3	0,766	0,751	0,747	0,778	0,776
3,5	0,76	0,746	0,741	0,772	0,77
4	0,754	0,74	0,736	0,766	0,764
4,5	0,748	0,734	0,731	0,76	0,758
5,5	0,735	0,723	0,72	0,749	0,746
6,5	0,724	0,712	0,709	0,736	0,734
7,5	0,711	0,701	0,698	0,725	0,722
8,5	0,7	0,691	0,689	0,714	0,711
9,5	0,689	0,681	0,678	0,703	0,7
10,5	0,678	0,671	0,668	0,692	0,689
11,5	0,667	0,661	0,659	0,682	0,678
12,5	0,656	0,651	0,649	0,671	0,667
14,5	0,635	0,632	0,63	0,651	0,646
16,5	0,615	0,614	0,613	0,631	0,626
18,5	0,596	0,596	0,595	0,612	0,607
20,5	0,577	0,578	0,578	0,594	0,588
22,5	0,559	0,562	0,561	0,577	0,571
24,5	0,542	0,546	0,545	0,56	0,553
26,5	0,525	0,53	0,53	0,543	0,536
28,5	0,509	0,515	0,515	0,527	0,52
32,5	0,478	0,486	0,487	0,497	0,489
36,5	0,45	0,46	0,46	0,469	0,461
40,5	0,423	0,435	0,436	0,443	0,434
44,5	0,398	0,411	0,412	0,418	0,409
48,5	0,375	0,389	0,391	0,394	0,386
52,5	0,354	0,368	0,37	0,373	0,364
56,5	0,333	0,349	0,351	0,352	0,343
60,5	0,315	0,331	0,333	0,334	0,324
68,5	0,28	0,298	0,3	0,299	0,289
76,5	0,25	0,268	0,271	0,268	0,259
84,5	0,224	0,242	0,245	0,242	0,232

Figure 52: The Excel setup used to process the data obtained from the Malvern software to find the size intensity distribution (X intensity) and correlation (X lag time). The rows with data continue past this screenshot. The blue cells show the average size and average derived count rate for the measurements. This is the data from Section 4.1.5, Figures 33 and 34.

C MALS data processing

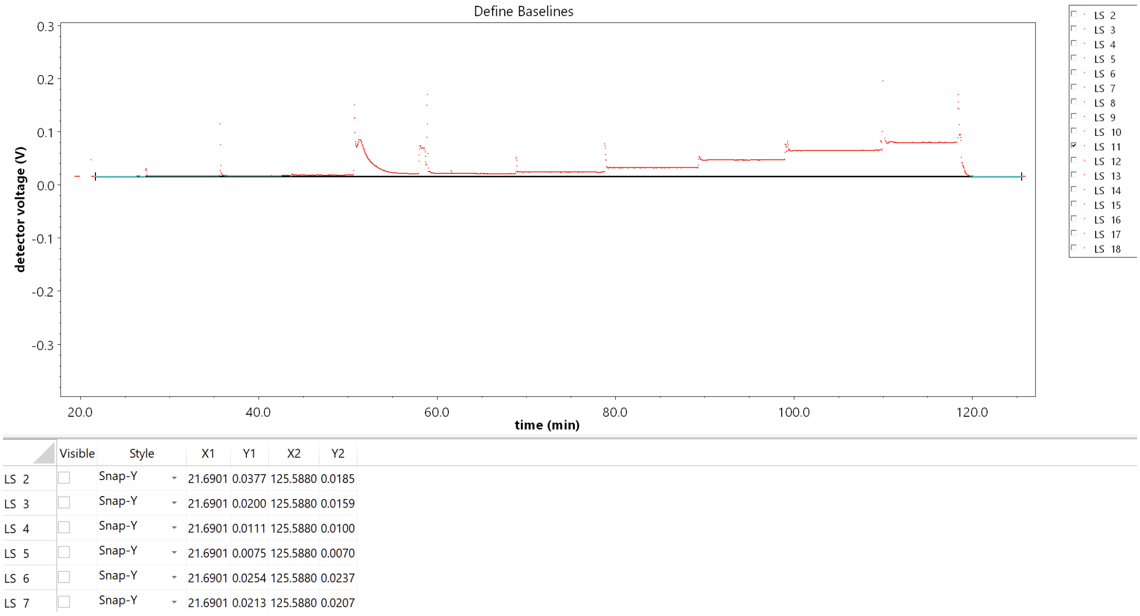

	Visible	Style	X1	Y1	X2	Y2
LS 2	☐	Snap-Y	21.6901	0.0377	125.5880	0.0185
LS 3	☐	Snap-Y	21.6901	0.0200	125.5880	0.0159
LS 4	☐	Snap-Y	21.6901	0.0111	125.5880	0.0100
LS 5	☐	Snap-Y	21.6901	0.0075	125.5880	0.0070
LS 6	☐	Snap-Y	21.6901	0.0254	125.5880	0.0237
LS 7	☐	Snap-Y	21.6901	0.0213	125.5880	0.0207

Figure 53: Baselines are defined in Astra. Here from the experiment with pullulan in Section 4.2.1

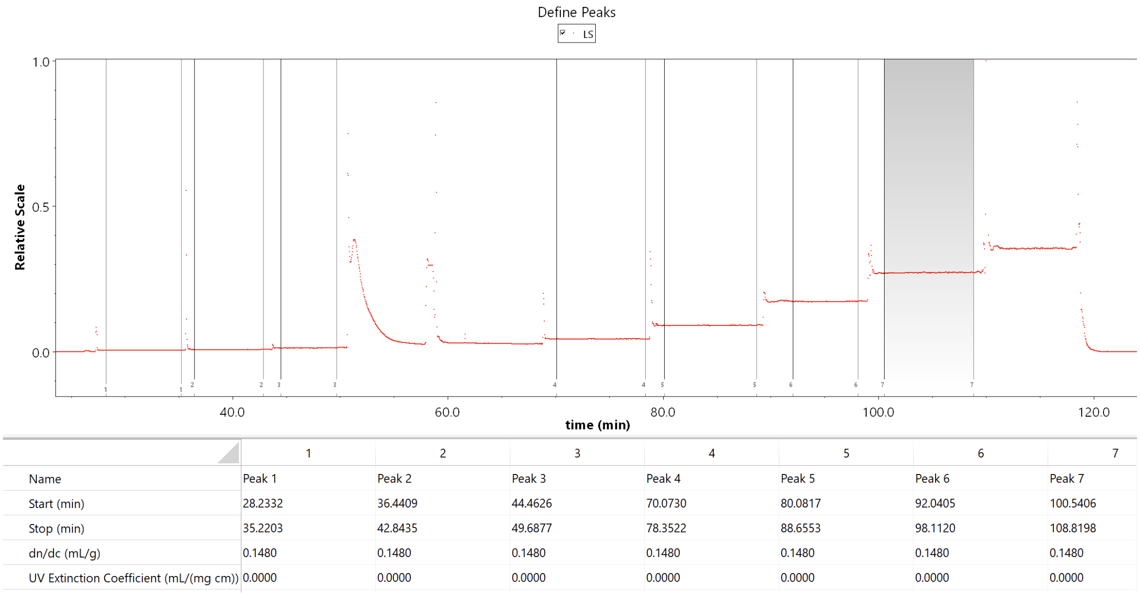

	1	2	3	4	5	6	7
Name	Peak 1	Peak 2	Peak 3	Peak 4	Peak 5	Peak 6	Peak 7
Start (min)	28.2332	36.4409	44.4626	70.0730	80.0817	92.0405	100.5406
Stop (min)	35.2203	42.8435	49.6877	78.3522	88.6553	98.1120	108.8198
dn/dc (mL/g)	0.1480	0.1480	0.1480	0.1480	0.1480	0.1480	0.1480
UV Extinction Coefficient (mL/(mg cm))	0.0000	0.0000	0.0000	0.0000	0.0000	0.0000	0.0000

Figure 54: Peaks are defined in Astra. Here from the experiment with pullulan in Section 4.2.1

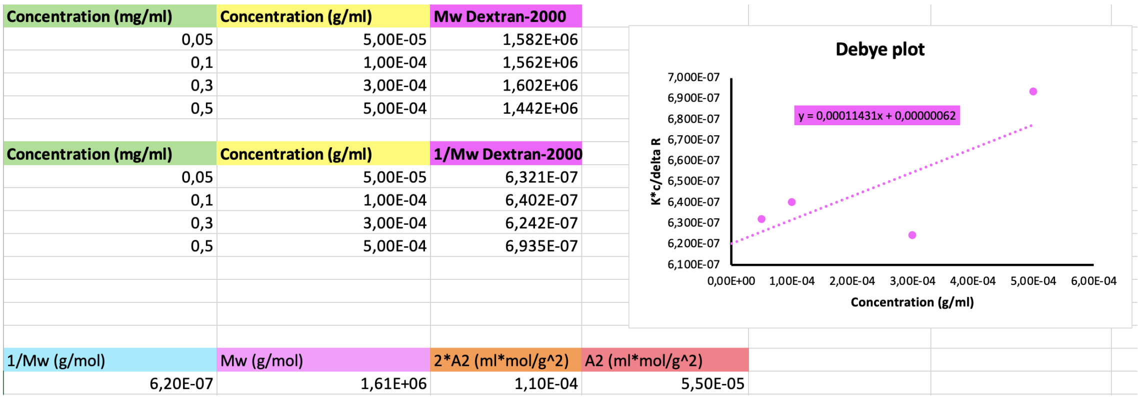

Concentration (mg/ml)	Concentration (g/ml)	Mw Dextran-2000
0,05	5,00E-05	1,582E+06
0,1	1,00E-04	1,562E+06
0,3	3,00E-04	1,602E+06
0,5	5,00E-04	1,442E+06

Concentration (mg/ml)	Concentration (g/ml)	1/Mw Dextran-2000
0,05	5,00E-05	6,321E-07
0,1	1,00E-04	6,402E-07
0,3	3,00E-04	6,242E-07
0,5	5,00E-04	6,935E-07

1/Mw (g/mol)	Mw (g/mol)	2*A2 (ml*mol/g^2)	A2 (ml*mol/g^2)
6,20E-07	1,61E+06	1,10E-04	5,50E-05

Figure 55: The Excel setup used to process the data obtained from Astra to find the calculated molecular weight and the second virial coefficient of Dextran-2000. These are the results from dextran in Section 4.2.1.

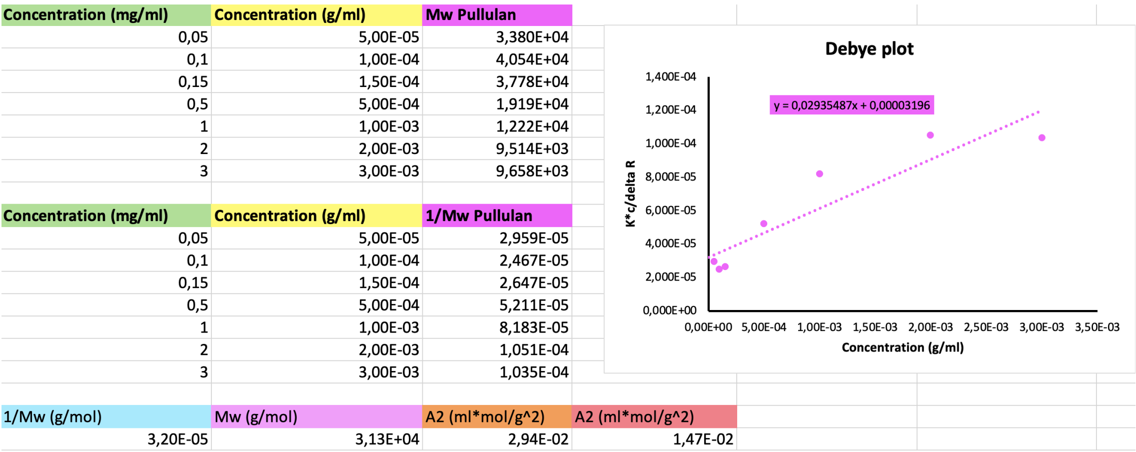

Concentration (mg/ml)	Concentration (g/ml)	Mw Pullulan
0,05	5,00E-05	3,380E+04
0,1	1,00E-04	4,054E+04
0,15	1,50E-04	3,778E+04
0,5	5,00E-04	1,919E+04
1	1,00E-03	1,222E+04
2	2,00E-03	9,514E+03
3	3,00E-03	9,658E+03

Concentration (mg/ml)	Concentration (g/ml)	1/Mw Pullulan
0,05	5,00E-05	2,959E-05
0,1	1,00E-04	2,467E-05
0,15	1,50E-04	2,647E-05
0,5	5,00E-04	5,211E-05
1	1,00E-03	8,183E-05
2	2,00E-03	1,051E-04
3	3,00E-03	1,035E-04

1/Mw (g/mol)	Mw (g/mol)	A2 (ml*mol/g^2)	A2 (ml*mol/g^2)
3,20E-05	3,13E+04	2,94E-02	1,47E-02

Figure 56: The Excel setup used to process the data obtained from Astra to find the calculated molecular weight and the second virial coefficient of pullulan in Section 4.2.1.

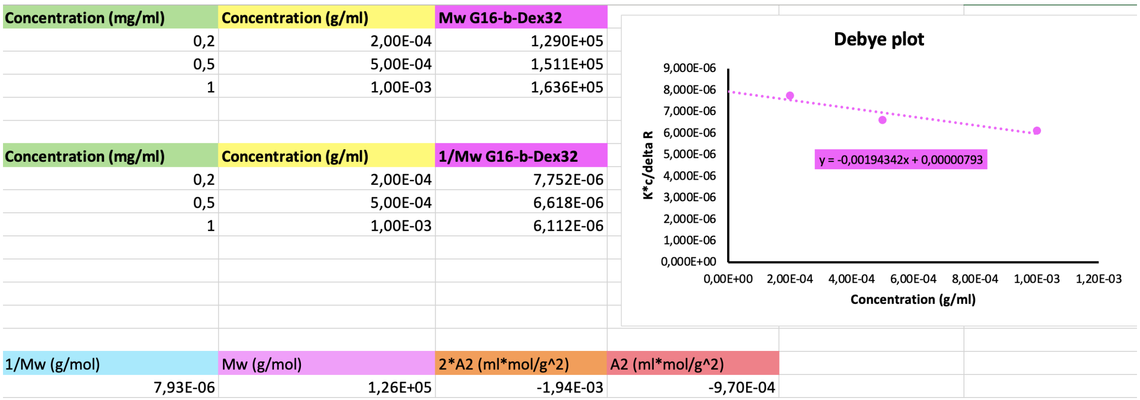

Concentration (mg/ml)	Concentration (g/ml)	Mw G16-b-Dex32
0,2	2,00E-04	1,290E+05
0,5	5,00E-04	1,511E+05
1	1,00E-03	1,636E+05

Concentration (mg/ml)	Concentration (g/ml)	1/Mw G16-b-Dex32
0,2	2,00E-04	7,752E-06
0,5	5,00E-04	6,618E-06
1	1,00E-03	6,112E-06

1/Mw (g/mol)	Mw (g/mol)	2*A2 (ml*mol/g^2)	A2 (ml*mol/g^2)
7,93E-06	1,26E+05	-1,94E-03	-9,70E-04

Figure 57: The Excel setup used to process the data obtained from Astra to find the calculated molecular weight and the second virial coefficient of G_{16}-b-Dex_{32} NPs. These are the results from Section 4.2.2.

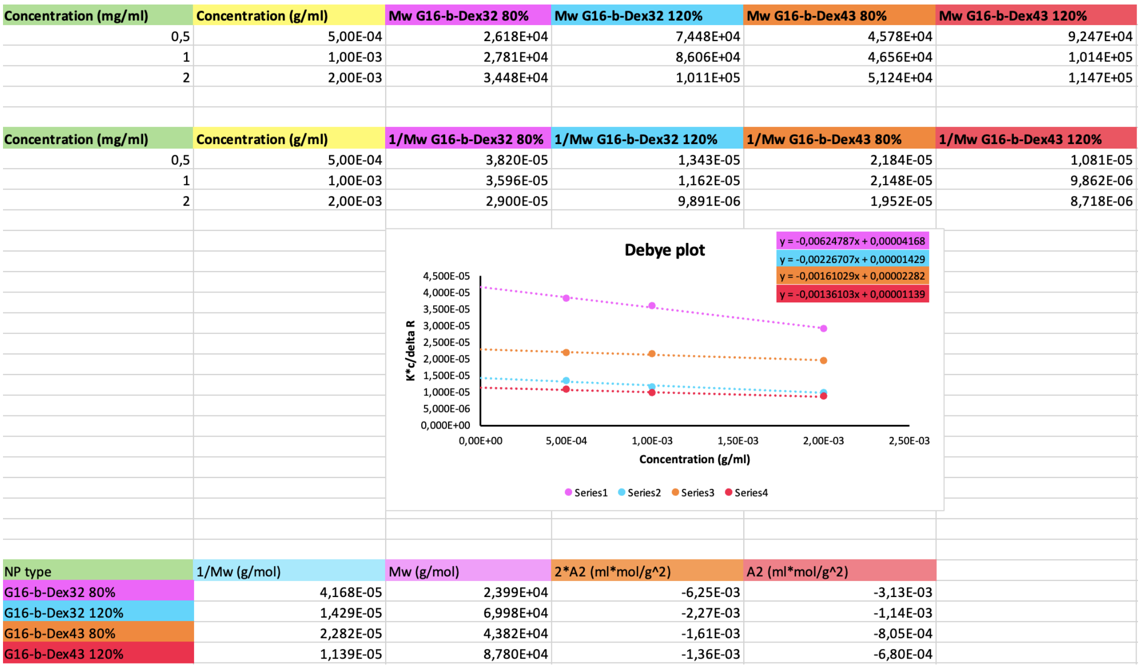

Concentration (mg/ml)	Concentration (g/ml)	Mw G16-b-Dex32 80%	Mw G16-b-Dex32 120%	Mw G16-b-Dex43 80%	Mw G16-b-Dex43 120%
0,5	5,00E-04	2,618E+04	7,448E+04	4,578E+04	9,247E+04
1	1,00E-03	2,781E+04	8,606E+04	4,656E+04	1,014E+05
2	2,00E-03	3,448E+04	1,011E+05	5,124E+04	1,147E+05

Concentration (mg/ml)	Concentration (g/ml)	1/Mw G16-b-Dex32 80%	1/Mw G16-b-Dex32 120%	1/Mw G16-b-Dex43 80%	1/Mw G16-b-Dex43 120%
0,5	5,00E-04	3,820E-05	1,343E-05	2,184E-05	1,081E-05
1	1,00E-03	3,596E-05	1,162E-05	2,148E-05	9,862E-06
2	2,00E-03	2,900E-05	9,891E-06	1,952E-05	8,718E-06

NP type	1/Mw (g/mol)	Mw (g/mol)	2*A2 (ml*mol/g^2)	A2 (ml*mol/g^2)
G16-b-Dex32 80%	4,168E-05	2,399E+04	-6,25E-03	-3,13E-03
G16-b-Dex32 120%	1,429E-05	6,998E+04	-2,27E-03	-1,14E-03
G16-b-Dex43 80%	2,282E-05	4,382E+04	-1,61E-03	-8,05E-04
G16-b-Dex43 120%	1,139E-05	8,780E+04	-1,36E-03	-6,80E-04

Figure 58: The Excel setup used to process the data obtained from Astra to find the calculated molecular weight and the second virial coefficient of different NPs. These are the results from Section 4.2.3.

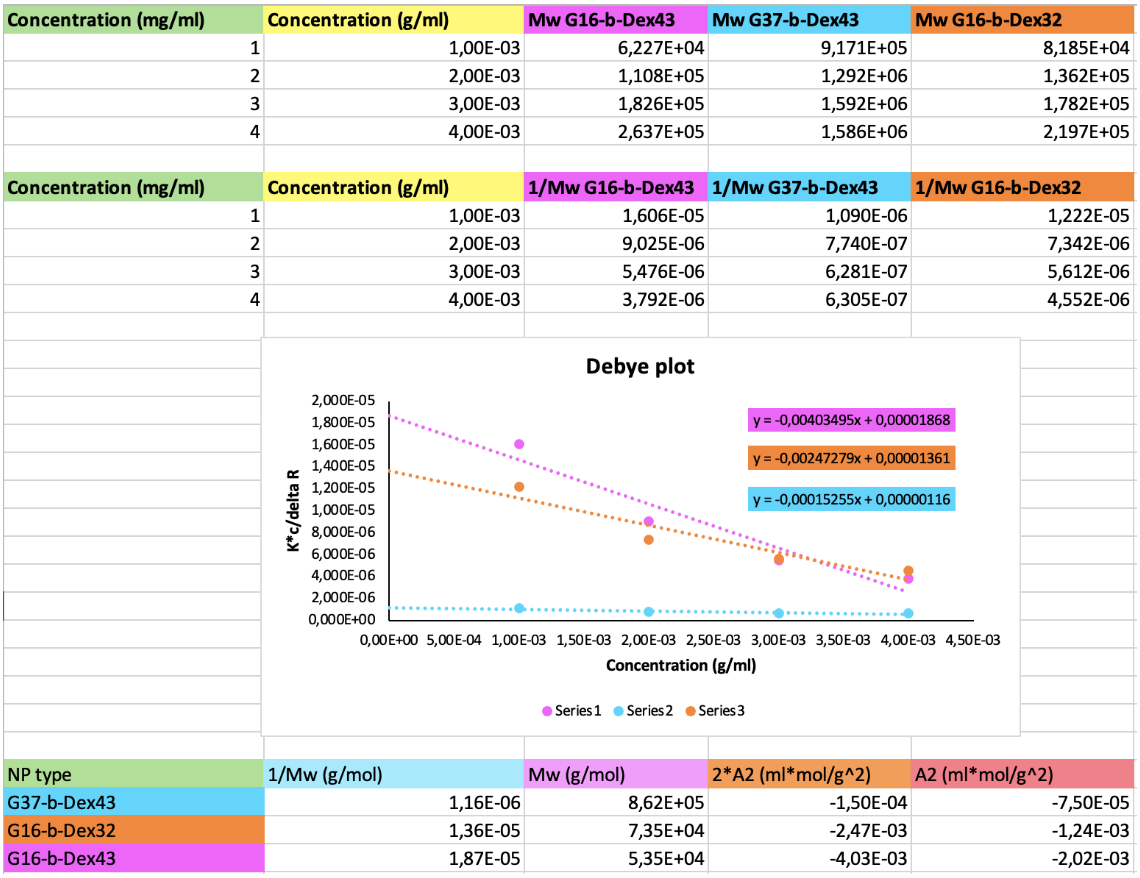

Concentration (mg/ml)	Concentration (g/ml)	Mw G16-b-Dex43	Mw G37-b-Dex43	Mw G16-b-Dex32
1	1,00E-03	6,227E+04	9,171E+05	8,185E+04
2	2,00E-03	1,108E+05	1,292E+06	1,362E+05
3	3,00E-03	1,826E+05	1,592E+06	1,782E+05
4	4,00E-03	2,637E+05	1,586E+06	2,197E+05

Concentration (mg/ml)	Concentration (g/ml)	1/Mw G16-b-Dex43	1/Mw G37-b-Dex43	1/Mw G16-b-Dex32
1	1,00E-03	1,606E-05	1,090E-06	1,222E-05
2	2,00E-03	9,025E-06	7,740E-07	7,342E-06
3	3,00E-03	5,476E-06	6,281E-07	5,612E-06
4	4,00E-03	3,792E-06	6,305E-07	4,552E-06

NP type	1/Mw (g/mol)	Mw (g/mol)	2*A2 (ml*mol/g^2)	A2 (ml*mol/g^2)
G37-b-Dex43	1,16E-06	8,62E+05	-1,50E-04	-7,50E-05
G16-b-Dex32	1,36E-05	7,35E+04	-2,47E-03	-1,24E-03
G16-b-Dex43	1,87E-05	5,35E+04	-4,03E-03	-2,02E-03

Figure 59: The Excel setup used to process the data obtained from Astra to find the calculated molecular weight and the second virial coefficient of different NPs. These are the results from Section 4.2.4.

D Tools used in Gwyddion

Align rows using various methods

Measure distances and directions between points

Stretch color range to part of data

Figure 60: The tools used in the software Gwyddion.

E Full-size SEM images

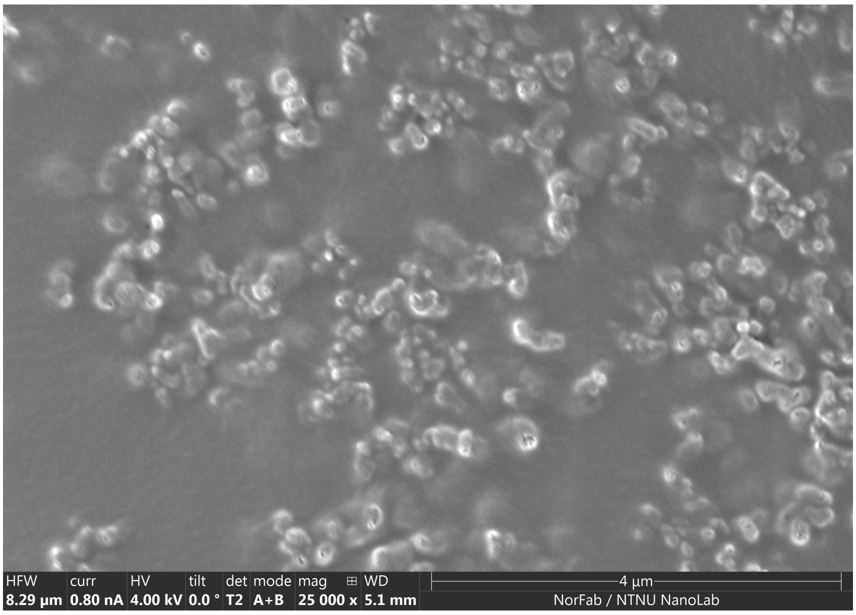

Figure 61: G_{16}-b-Dex_{32} NPs prepared by dialysis. This sample was vacuum dried.

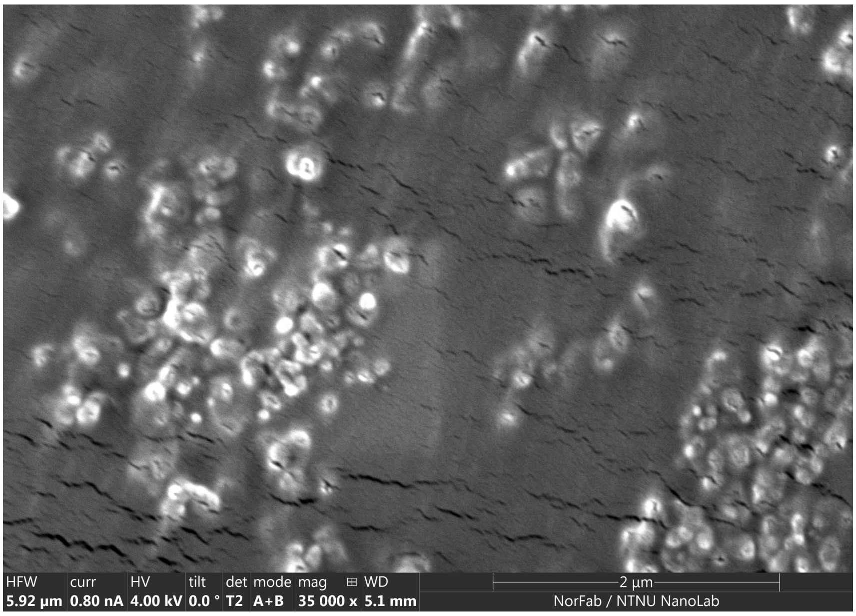

Figure 62: G_{16}-b-Dex_{32} NPs prepared by dialysis. This sample was vacuum dried.

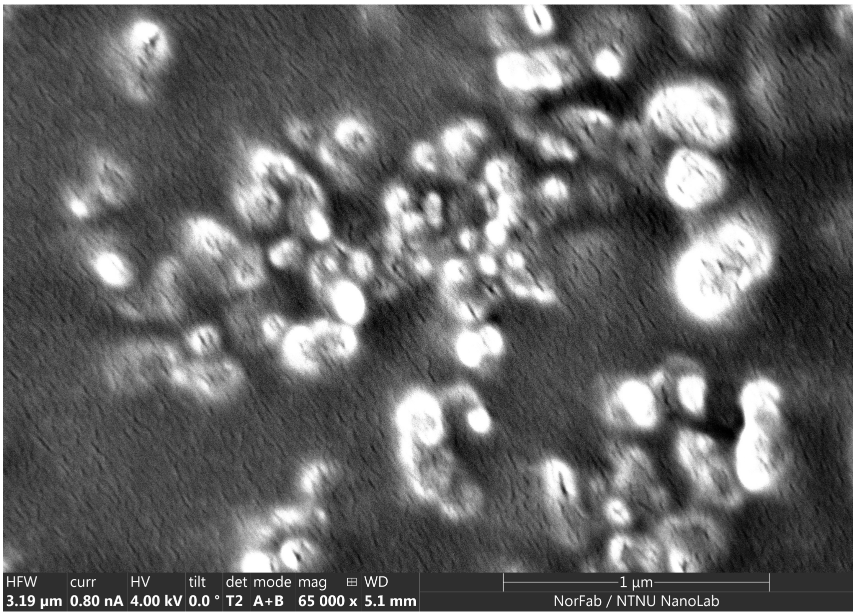

Figure 63: G_{16}-b-Dex_{32} NPs prepared by dialysis. This sample was vacuum dried.

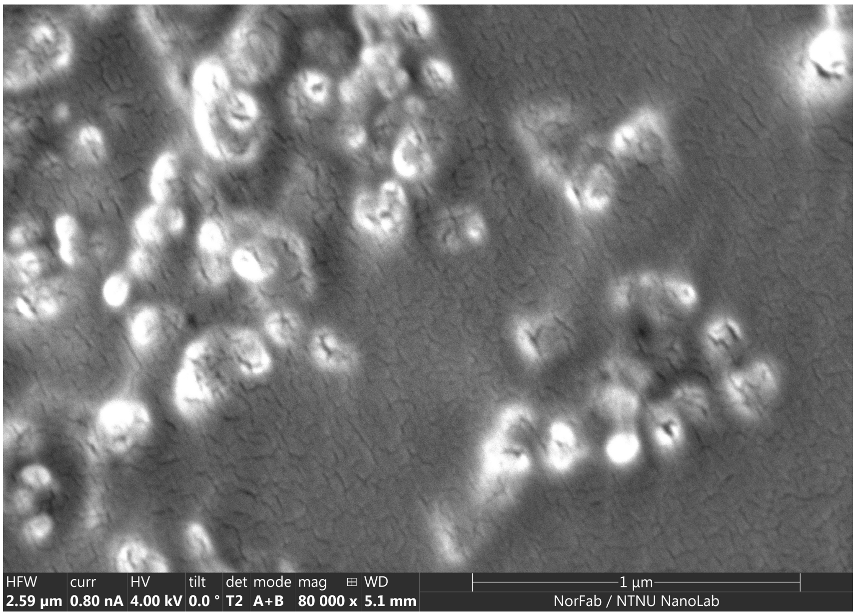

Figure 64: G_{16}-b-Dex_{32} NPs prepared by dialysis. This sample was vacuum dried.

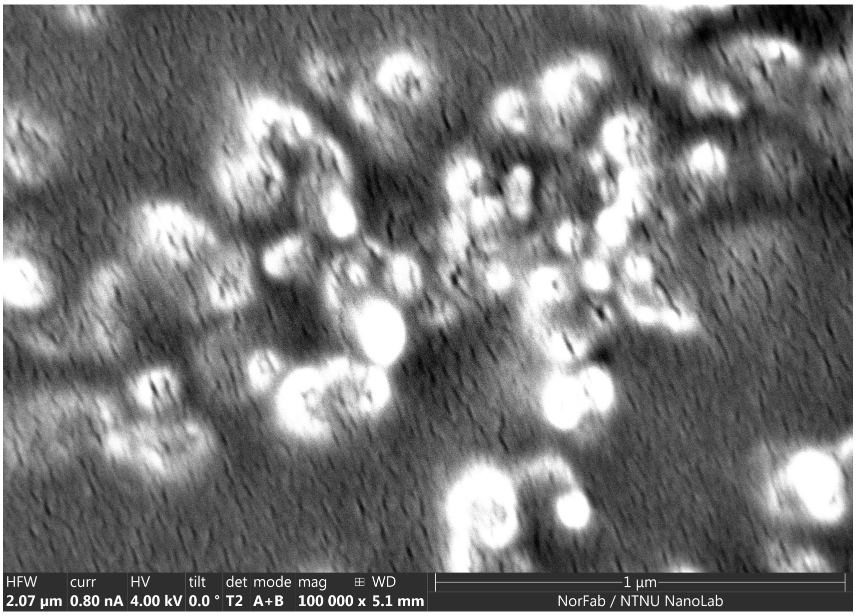

Figure 65: G_{16}-b-Dex_{32} NPs prepared by dialysis. This sample was vacuum dried.

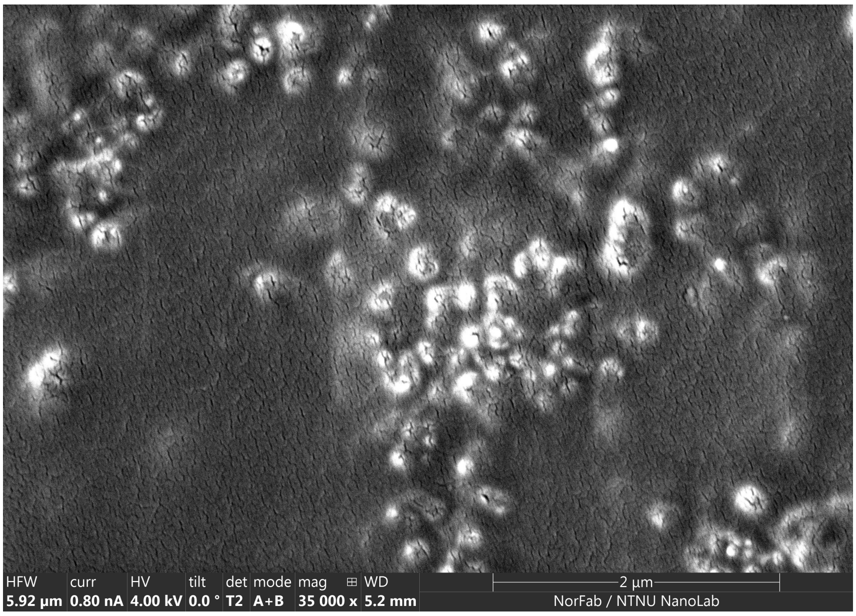

Figure 66: G_{16}-b-Dex_{32} NPs prepared by dialysis. This sample was not vacuum dried.

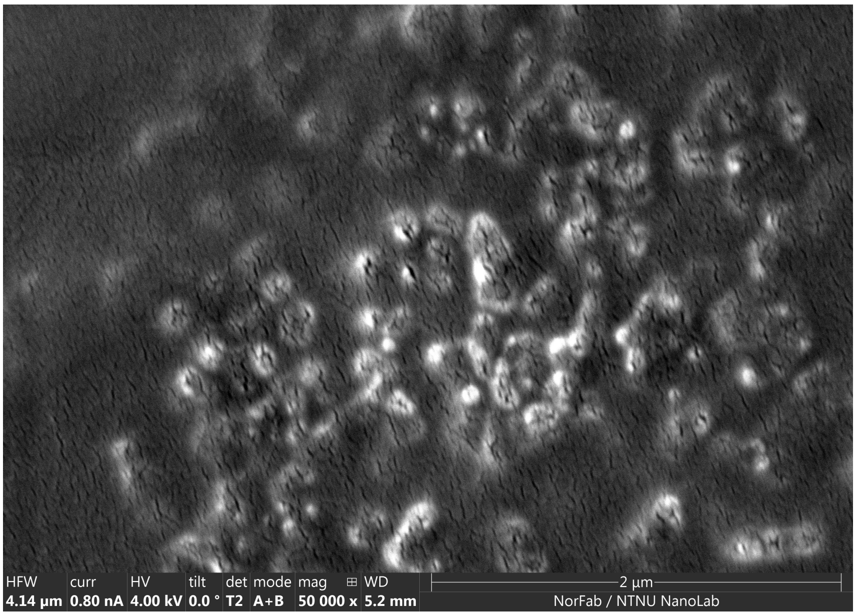

Figure 67: G_{16}-b-Dex_{32} NPs prepared by dialysis. This sample was not vacuum dried.

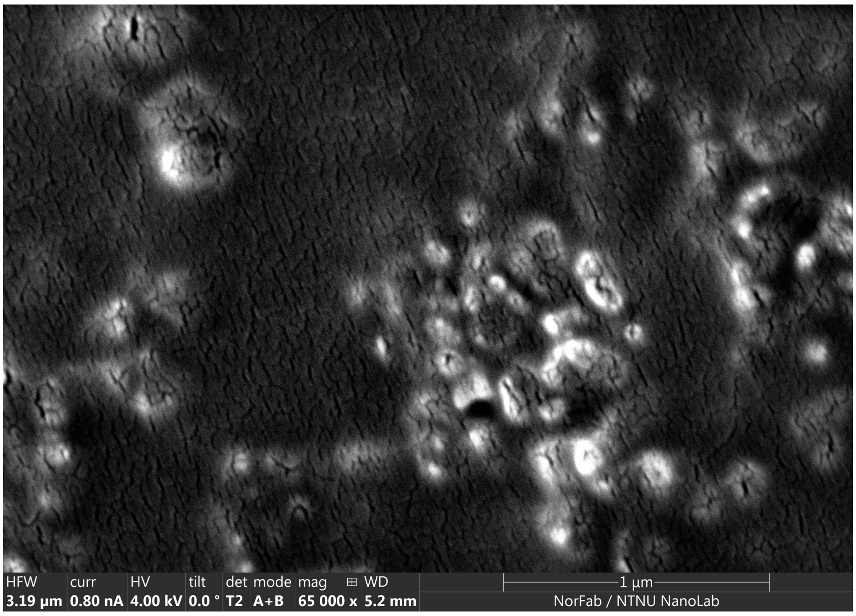

Figure 68: G_{16}-b-Dex_{32} NPs prepared by dialysis. This sample was not vacuum dried.

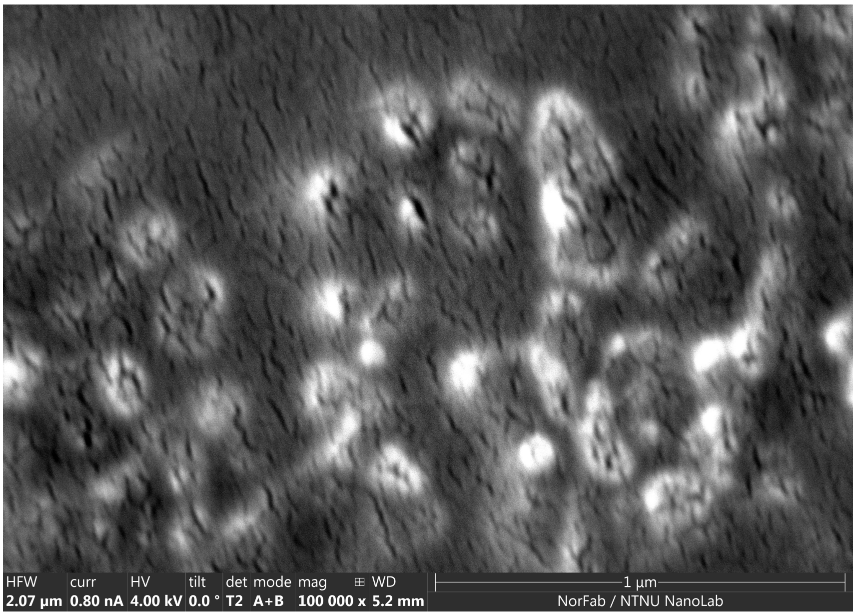

Figure 69: G_{16}-b-Dex_{32} NPs prepared by dialysis. This sample was not vacuum dried.

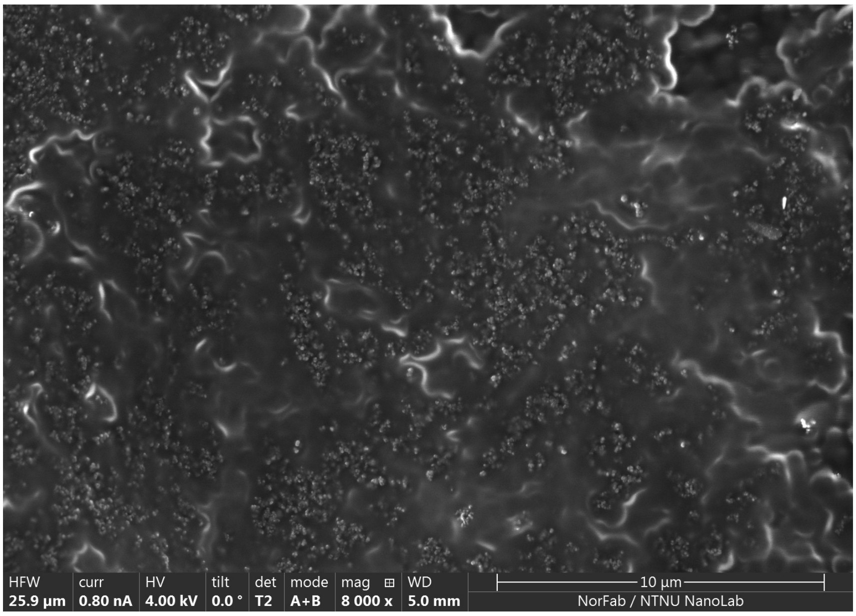

Figure 70: Pure carbon tape for the negative control.

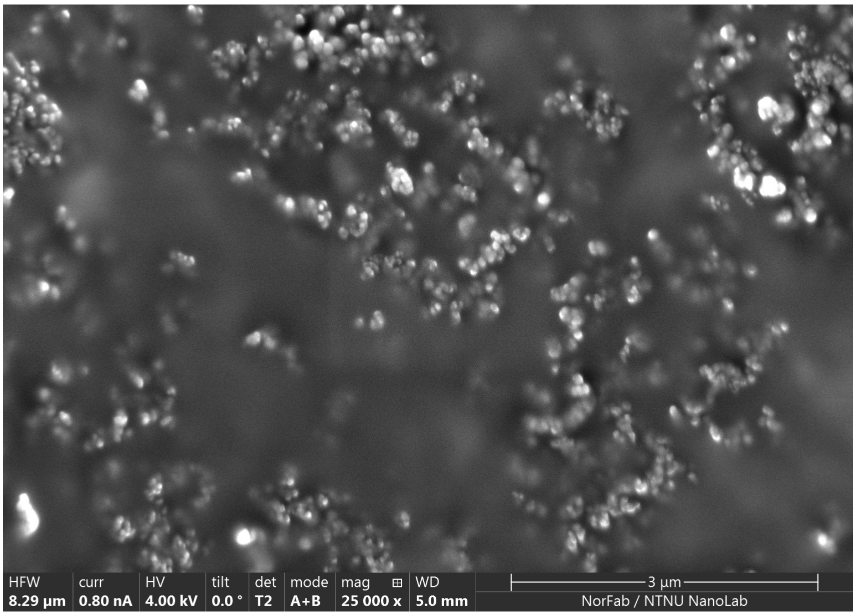

Figure 71: Pure carbon tape for the negative control.

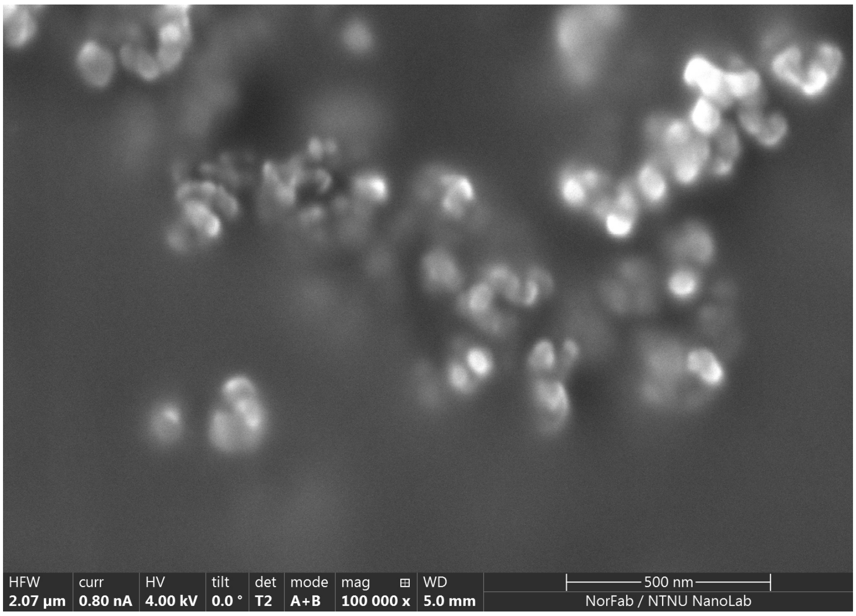

Figure 72: Pure carbon tape for the negative control.

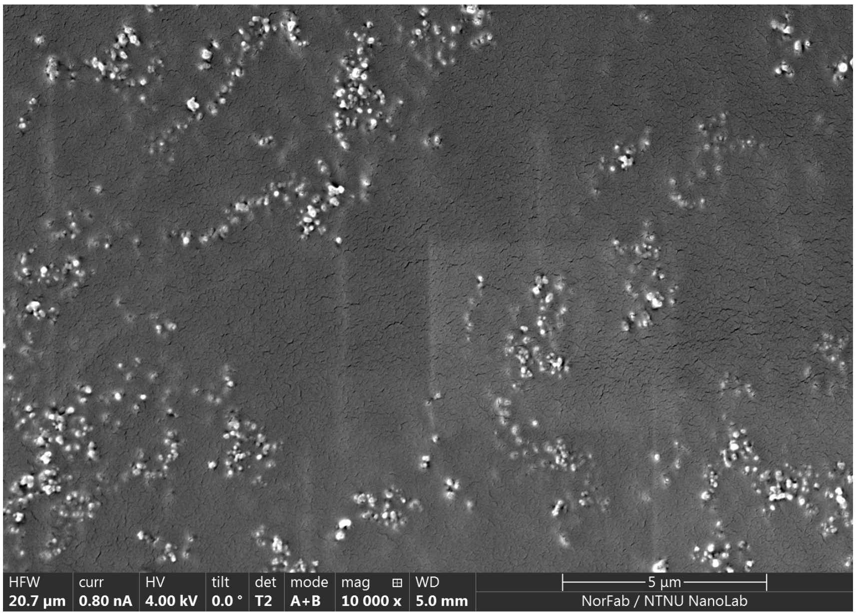

Figure 73: 20 mM $CaCl_2$ and 10 mM NaCl for the negative control.

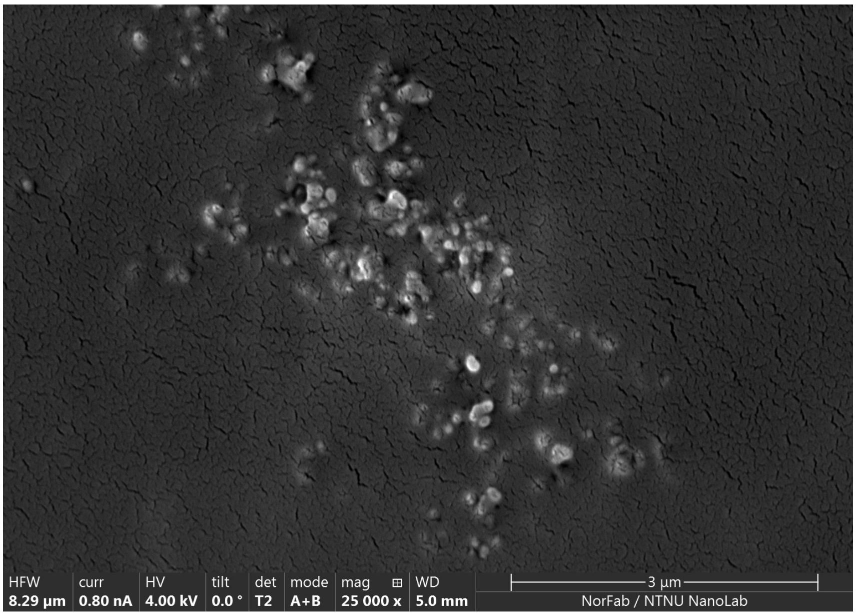

Figure 74: 20 mM $CaCl_2$ and 10 mM NaCl for the negative control.

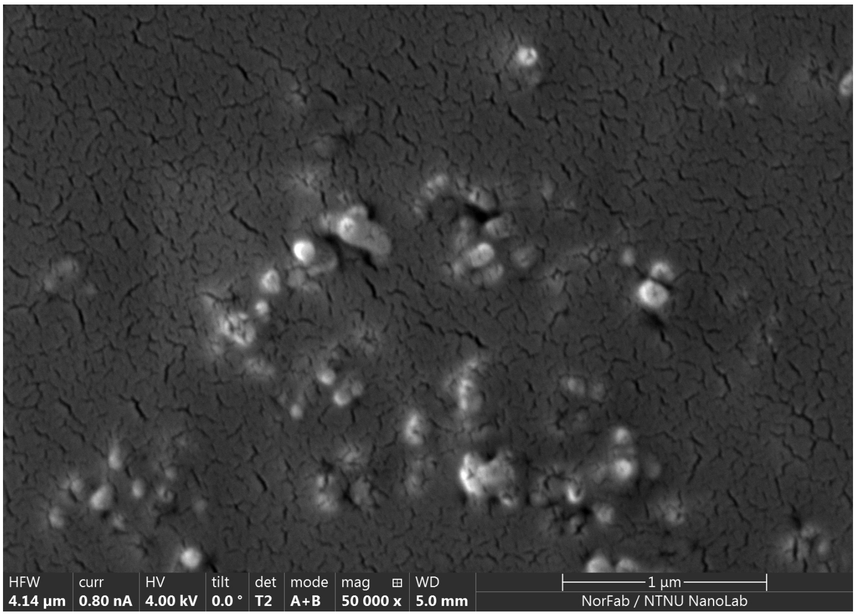

Figure 75: 20 mM $CaCl_2$ and 10 mM NaCl for the negative control.

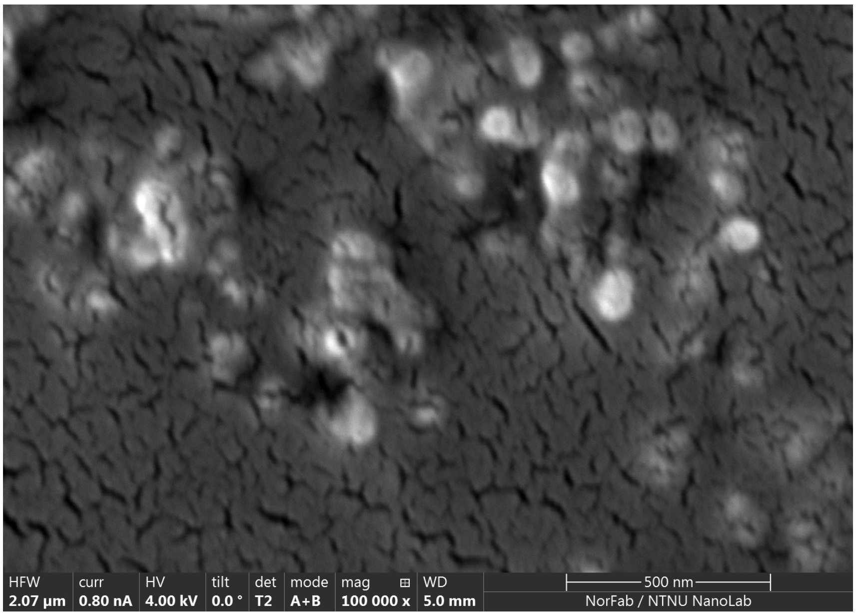

Figure 76: 20 mM $CaCl_2$ and 10 mM NaCl for the negative control.

NTNU

Norwegian University of
Science and Technology